Crystal Structure, Electric Properties and Phase Transition of Phase Change Materials $\mathbf{Ge_2Sb_2Se_{5x}Te_{5-5x}}$

Zhenyang Xu

A Dissertation Presented to the Graduate Faculty
of the University of Virginia in Candidacy for the Degree of
Doctor of Philosophy

University of Virginia, Physics Department

University of Virginia
Aug., 2021

Abstract

Computers with solid state memories own their success in part due to phase change materials (PCMs). These are binary, ternary or even quaternary compounds, consisting of Ge, Sb and one or more chalcogen ions such as Te and Se. PCMs have been of interest for decades because their reversible transformation from crystalline to amorphous states of matter is coupled with vastly different electric and optical properties that are so uniquely suited to devices such as random access memories. PCM can be made into random access memories due to their vast differences in electrical and optical characteristics between amorphous and crystalline phases. In today's PCM research, the central problem lies in finding a PCM with high performance in reading and writing data. This requires PCMs to have fast switching, low activation energy, and stable amorphous phases. The first PCM $Ge_2Sb_2Te_5$ (GST-225) was discovered in 1987. After that many material systems have been proposed such as AgInSbTe, GeSbMnSn and AuTe2. Of these, GST-225 remains a promising candidate due to its unique physical properties. A key structural component to the transformation is the appearance of a rocksalt like structure that is intermediary to the hexagonal ground state and the amorphous state. The rocksalt structure is riddled with vacancies and acts as a conduit to the transition from the crystalline to the amorphous phase. However, the rocksalt like structure is prevalent in thin films only.

In this thesis, bulk $Ge_2Sb_2Te_5$ (GST-225) was investigated to explore the structural and electronic properties with Se doping. $Ge_2Sb_2Se_{5x}Te_{5-5x}$ (GSST-225) with varying degrees of Se doping were synthesized under two different conditions involving slow cooling (SC) and liquid nitrogen quenching (Q). It is shown that upon doping, liquid nitrogen quenched $Ge_2Sb_2Se_{5x}Te_{5-5x}$ (GSST-225) exhibits a direct hexagonal-to-amorphous phase change above $x > 0.8$ The rock-salt like structure appears as a second phase with a volume fraction that does not change as a function of the doping. The electric resistivity and optical reflectivity of GST-225 undergo changes with several orders of magnitude when it's transformed between different phases. In this work, the phase change of GSST-225 is accompanied by a metal-to-insulator transition (MIT), with several orders of magnitude increase in the resistivity on approaching the amorphous state. A similar MIT is observed even without the phase change, in hexagonal crystals with doping levels above $x > 0.8$. Through crystallization kinetics study, we reported the re-crystallization onset temperature and activation energy of amorphous GSST. In our neutron diffraction experiments, PDF analyses were performed to research the local structure evolution across phase transition in Q-GSSTs. We reported the existence of local structures in amorphous GSST-225. These local structures have shapes like tetragon and feature Ge/Sb atoms siting at centers and Te/Se atoms siting at vertices.

From these results, GSST-225 is a suitable candidate for making random access memories. GSST-225 has fast phase transition and its amorphous phase is stable for data storage. It requires less activation energy to complete phase transition cycle. A more energy efficient type of random access memory can be made using this material.

Acknowledgments

During my Ph.D. studies I have received valuable support from my advisor, classmates, family and friends. I would like to thank my academic advisor, Prof. Despina Louca, whose guidance and vision helped me complete a long and exciting journey in physics. I would also like to thank the other members of my research committee, Prof. Kent Yagi, Prof. Giawei Chern, Prof. Utpal Chatterjee, Prof. Keivan Esfarjani.

The neutron scattering experiments in this work would not have been possible without the help and guidance of the instrument scientists and support staff at the neutron facilities. This includes Dr. Craig Brown at the NIST Center for Neutron Research, Dr. Jeorg Neuefeind, Dr. Michelle at the Spallation Neutron Source at Oak Ridge National Laboratory (ORNL).

I would like to express my thanks to my group members Dr. Junjie Yang, Dr. John Schneeloch, Dr. Chunruo Duan, Dr. Anushika Athauda, Yu Tao, Sharon Phillip for their help in experiments.

Finally, I would like to thank my parents for their support throughout my life. Their love and support has enabled me to pursue my academic degree.

Contents

List of Figures

List of Tables

Chapter 1

Introduction

Phase-change materials (PCMs) are promising materials for next generation data-storage device applications which have been explored for decades. PCMs have the potential for constituting random access memories due to their unique phase transition ability. Nowadays, the computer industry is in desperate need for a new generation of random access memories which have high performance. A major main question lies in phase change material research is that how to find proper material for constituting high-quality, non-volatile random access memories[1].

Several characteristics are required for PCMs. First, the desired PCMs should have a fast phase transition which is the key for fast data processing when they are made into random access memories. Nowadays, the normal data processing speed for a solid-state drive is around 500MB/s; for a hard disk drive, the speed is around 60∼80MB/s[2]. How to break through these speed limits is a vital problem, and it lies in the development of phase change materials. Second, the phase transition between crystalline and amorphous phases should be reversible and large cycling numbers should be expected. Most random access memories have the ability of erasing and reading data for multiple times. A typical standard for PCM is to have a large contrast in resistivity or reflectivity (for rewritable electronic or optical data storage, respectively) between crystalline and amorphous phases[1]. Fourth, phase change materials should have thermal stability. A minimum requirement is that the random access memories should maintain their data for at least several decades at room temperature. Since PCMs switch between crystalline and amorphous phases, a stable amorphous phase is required even though they are energetically unfavorable. Fifth, high chemical stability such as being waterproof and resistant to oxidation should also be an important criteria for judging the quality of a phase change material. A PCM with low phase transition activation energy is also a new requirement for looking for qualified candidate material. Additionally, with the increased demand for energy-efficient electronics, PCM with low activation energy which can trigger a phase transition is also desirable.

Many systems of materials have been researched in order to search for the ideal candidate PCMs for making random access memories. Among them, the GeTe-Sb_2Te_3 system was first discovered in 1987[1]. $Ge_2Sb_2Te_5$ is the most researched material and has many commercialized applications. This material can be viewed as a pseudobinary mixture of GeTe and Sb_2Te_3 atomic layers and can switch between its amorphous and crystalline phases with fast speed. Shown in Fig. 1-1 is a resistivity plot of $Ge_2Sb_2Te_5$ at different annealing temperatures[3]. The resistivity has three regions where the resistivity changes by orders of magnitude, representing the three different phases of Ge2Sb2Te5: the amorphous, cubic, and hexagonal phases. The amorphous phase has the highest resistivity while the crystalline hexagonal phase has the lowest. The amorphous and hexagonal phases are stable while the cubic phase is metastable under room temperature. Of the possible phase transitions, the transition typically used in GST-225 devices is between the crystalline and amorphous phases. High contrast in electric resistivity or optical reflectivity is satisfied between these two states.

Fig. 1-2(a) shows resistivity data measured on $Ge_2Sb_2Te_5$ material in thin film form[4]. Thin films with thicknesses of 50nm, 10nm, 5nm, 2.5nm were measured with constant heating and cooling rates. Like the results discussed above, three different resistivity regimes representing three different phases of $Ge_2Sb_2Te_5$ were shown in the data. With the increase of thin film thickness, resistivity also increased due to the segregation or loss of tellurium atoms[5]. Fig. 1-2(b) shows the effect of heating rate on the resistivity of thin film $Ge_2Sb_2Te_5$ with 2nm thickness. Thin film $Ge_2Sb_2Te_5$ samples with the same thickness (2nm) were synthesized by sputtering and

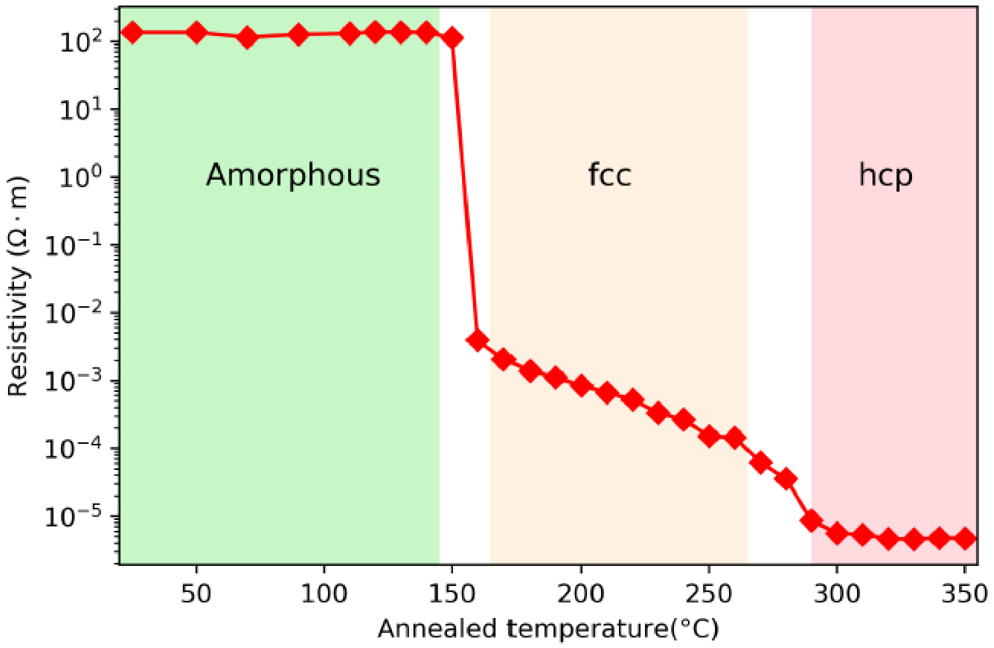

Figure 1-1: Resistivity of $Ge_2Sb_2Te_5$ as a function of annealed temperature[3].

their resistivity were measured with different heating rates (ranging from 3°C/min to 500°C/min). As we can see from the figure, the resistivity of thin film $Ge_2Sb_2Te_5$ increase as the heating rate increases. The rich physics behind thin film $Ge_2Sb_2Te_5$ is worth exploring.

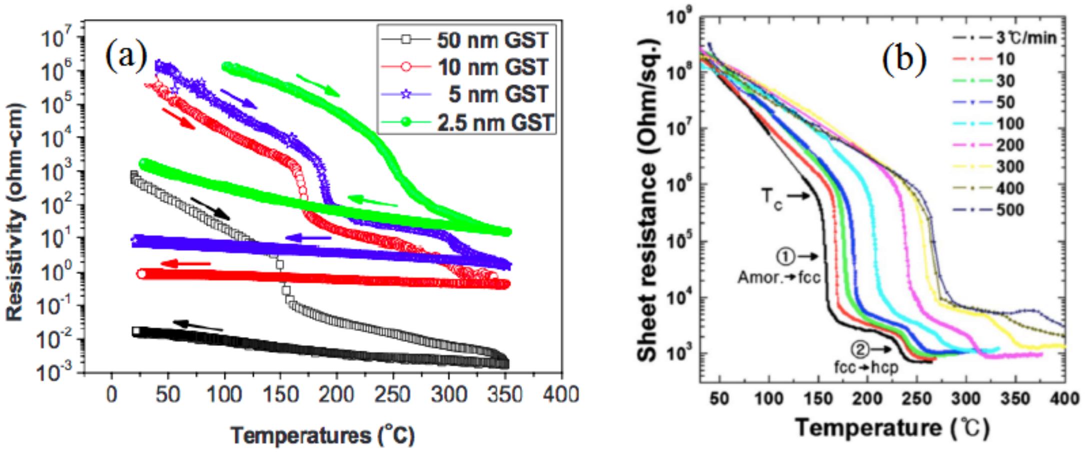

Figure 1-2: Fig. (a) shows the resistivity data measured on thin film $Ge_2Sb_2Te_5$ with different thickness. Fig. (b) shows the resistivity data measured on 2nm thick thin film $Ge_2Sb_2Te_5$ with different heating rate.[5, 6].

Doping $Ge_2Sb_2Te_5$ material is another way of improving the performance of $Ge_2Sb_2Te_5$ in random access memories. For example, Hubert et al. investigated the electrical performances of carbon-doped $Ge_2Sb_2Te_5$ (C-GST) in 2012[4]. In their work, thin film carbon-doped $Ge_2Sb_2Te_5$ (C-GST) materials with different levels of carbon doping were synthesized with a deposition method. Resistivity curves as functions of temperature were measured as shown in Fig. 1-3(a). The PCM devices which are based on these C-GST materials are shown in Fig. 1-3(b). The test results show that PCM devices with 5% of carbon doping content yield over 50% of electric current reduction compared to GST devices[4]. This result indicates that carbon-doped $Ge_2Sb_2Te_5$ may serve as a good candidate for PCM devices with low phase transition activation energy.

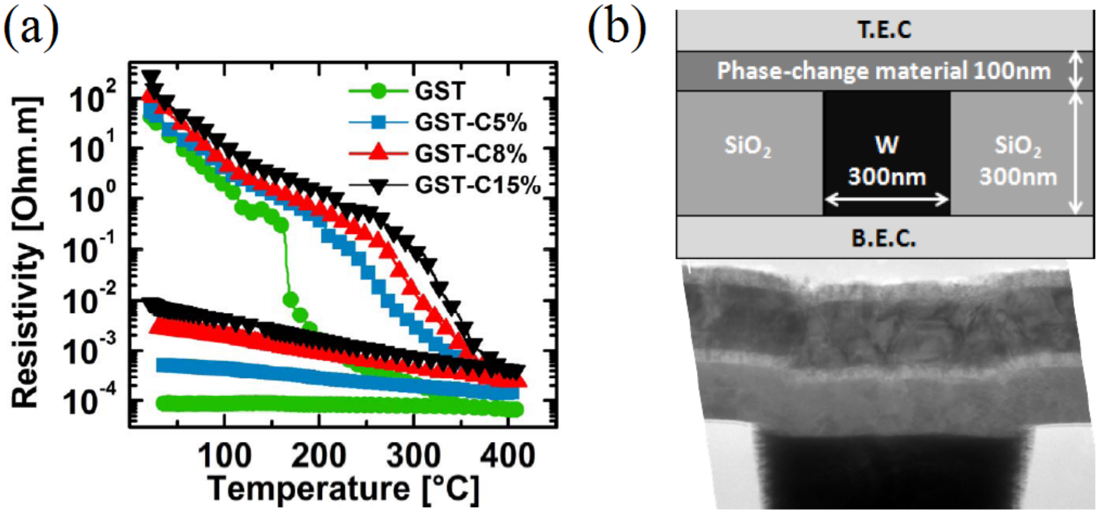

Figure 1-3: Fig. (a) shows the electrical resistivity of GST, 5% doped C-GST, 8% doped C-GST and 15% doped C-GST 100nm thick full-sheet layers as function of temperature. Fig. (b) shows a schematic picture of the studied PCM device and its corresponding cross section TEM image. [4].

In order to further explore the possibility of fabricating PCM with higher electric performance, we researched Se-doped GST-225 ($Ge_2Sb_2Se_{5x}Te_{5-5x}$) in bulk form with different doping contents ($0.0 \leq x \leq 1.0$, step $x = 0.1$). Both slow cooling (SC) and liquid nitrogen quenching (Q) methods were used. A crystalline-to-amorphous phase transition was observed in Q-GSST samples around $x = 0.9$. This is different from GST-225 since a high cooling rate ($\sim 10^9$K/s) is needed to make the sample amorphous. Through resistivity measurements, a metal-to-insulator transition (MIT) is observed both for SC-GSST and Q-GSST around $x = 0.9$. The phase transition in Q-GSST $x = 0.9$ samples was studied through temperature dependent XRD (X-ray Diffraction) measurements and DSC (Differential Scanning Calorimetry) measurements. The local structure of Se-doped $Ge_2Sb_2Te_5$ is investigated through PDF (Pair Distribution Function) analysis.

1.1 Layout of the Dissertation

This thesis contains several chapters which focus on different aspects of our research, they are organized as follows:

Chapter 1: Introduction.

Chapter 2: Background. This chapter is devoted to a discussion on PCM materials.

Chapter 3: Experimental Methods. This chapter includes three parts. Part one discusses the experimental techniques we have used for data collection which includes resistivity and DSC measurements. Part two discusses about the data analysis methods which includes Rietveld refinement of the XRD data and PDF analysis for the neutron diffraction data. Part three discusses several sample synthesis methods we have tried for GSST crystal growth.

Chapter 4: Crystal Structures and Electrical Properties of $Ge_2Sb_2Se_{5x}Te_{5-5x}$. This is the first chapter of presenting our research data on GSST-225 materials. First, the discussion on different phases and layer stacking orders will reveal the complexity behind GSST-225's crystal structures. A crystalline-to-amorphous phase transition was reported for Q-GSST around $x = 0.9$. Second, through resistivity measurements we demonstrated that metal-to-insulator transitions happen on both SC-GSST and Q-GSST around $x = 0.9$. Third, through temperature-dependent XRD measurements and DSC measurements on amorphous $x = 0.9$ GSST, crystallization kinetics during phase transition was studied and relative results were presented.

Chapter 5: Local Structure of $Ge_2Sb_2Se_{5x}Te_{5-5x}$. This is the second chapter of presenting our research data on GSST-225 materials. In this chapter, the neutron diffraction data of GSST-225 is analyzed and discussed. Through analysis of PDF patterns of amorphous Q-GGST samples, we discovered short-range peaks which indicate the existence of local structures. Small tetragonal local structures featuring Ge/Sb atoms as their centers and Te/Se as their corners are proposed to explain our experimental data.

Chapter 6: Conclusions. This chapter serves as a summary of our research data of GSST-225 materials from chapter 5 and 6.

Chapter 2

Phase Change Materials

Chalcogenide phase change materials receive more and more attention in recent years because of its application in random access memories. Phase change materials can switch between its crystalline and amorphous phases rapidly and reversibly. A high physical property contrast is observed between these two phases, such as electrical resistivity and optical resistivity. A phase transition is triggered by thermal heating or an electric/optic pulse. Two types of random access memories can be created from phase change materials: non-volatile electronic memories and optical memories[3]. Many of them have been commercialized (see Fig. 2-1). A promising future of this material can be expected.

2.1 Structure of PCMs

2.1.1 Phase Diagram of Ge-Sb-Te

In the ternary phase diagram of Ge-Sb-Te, a series of compounds can be found which are promising phase change material candidates. They all lie on the line connecting GeTe and Sb_2Te_3 endpoints. See Fig. 2-2. These candidates are $Ge_2Sb_2Te_5$ [1, 8, 2], $Ge_1Sb_2Te_4$ [1, 9, 10], $Ge_1Sb_4Te_7$ [1, 11, 12], and $Ge_3Sb_2Te_6$ [1, 13]. These compounds have a general chemical formula which can be written as $(GeTe)_n(Sb_2Te_3)_m$. From the point of view of structural unit cell, these compounds' unit cells can be

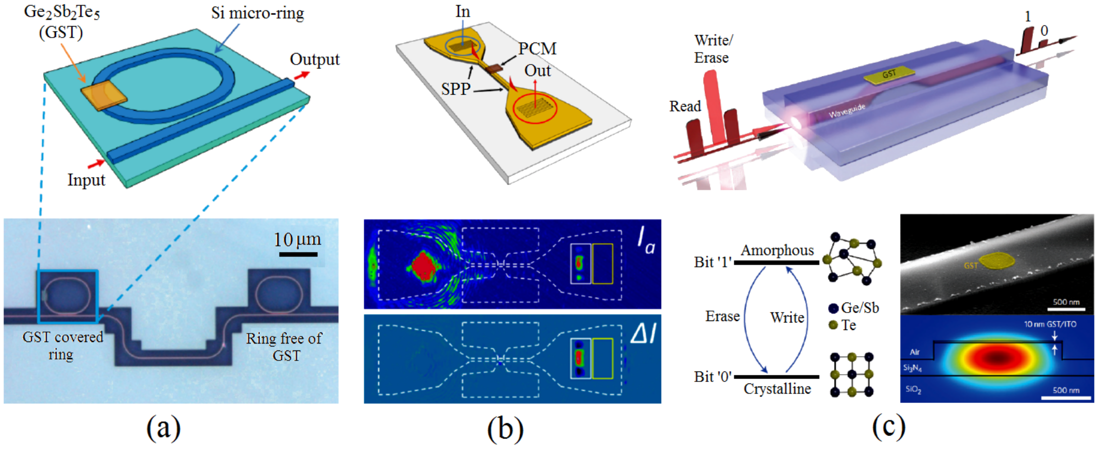

Figure 2-1: A figure showing the optical devices which uses GST as their medium. (a) An optical switch consisting of two micro-rings coupled to a waveguide. One of the rings is covered by GST. (b) A plasmonic waveguide with a GST strip in the middle neck. The optical intensity will drastically change if the GST material in the middle switches between its crystalline and amorphous phases. (c) A memory device with GST section on the top of the nanophotonic waveguide. Modified from [7].

constructed by stacking GeTe and Sb_2Te_3 layers along the z-axis direction. Due to different layer stacking sequences and Ge-Sb atomic position switching, these materials all have many possible layer stacking models. Some of these compounds have been used in commercial applications or products[1]. Of these materials, $Ge_2Sb_2Te_5$ is no doubt the most popular one, which has been extensively researched for many years. Besides the properties of $Ge_2Sb_2Te_5$'s crystal structure, electric properties, dynamic properties have been studied, its doped variants such as Bi-$Ge_2Sb_2Te_5$, C-$Ge_2Sb_2Te_5$, Co-$Ge_2Sb_2Te_5$ and Cr-$Ge_2Sb_2Te_5$ have also been synthesized and researched[14, 4].

2.1.2 Crystal structure of $Ge_2Sb_2Te_5$

The crystal structure of $Ge_2Sb_2Te_5$ can be viewed as a superlattice composed of sub-binary compounds GeTe and Sb_2Te_3. GeTe has been studied for many years due to its interesting phase transition characteristics[15, 16, 17]. The typical crystal structure of GeTe is a hexagonal unit cell with R3m symmetry. In a real GeTe material, various band gaps ranging from 0.3–0.8 eV have been reported which indicate the coexistence of various GeTe structures[18, 19, 20, 21]. In work done by K.

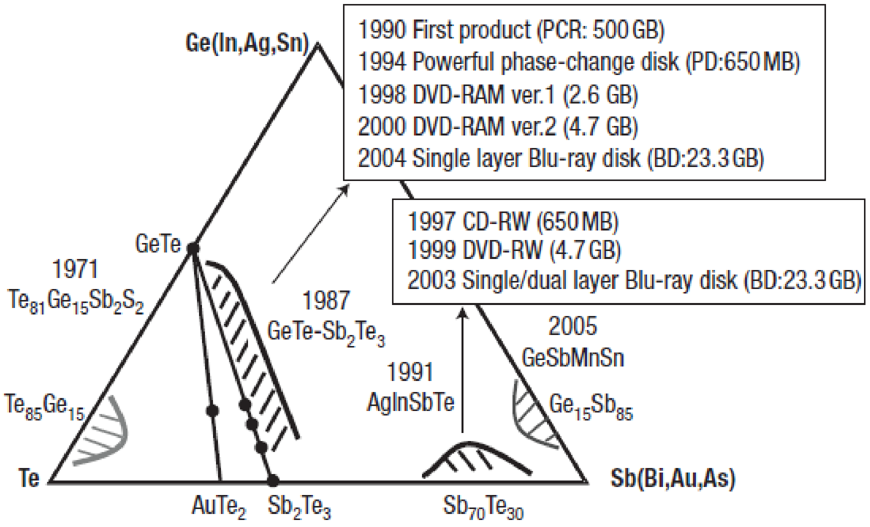

Figure 2-2: Ternary phase diagram of Ge-Sb-Te system. In the figure, different phase change materials are labeled with their years of discoveries and their usages in optical storage products.[1]

Jeong et al.[15], three possible crystal structure of GeTe were reported through DFT first-principles calculations (as shown in Fig. 2-3). Apart from these three crystalline phases, an amorphous phase is also shown when the material is quenched with a high cooling rate[15]. With the help of band gap calculations, it is found that structural transformation induces significant changes in the resistance between different phases in GeTe, which can be advantageous for fabricating data storage devices such as random access memories[15].

On the other hand, Sb_2Te_3 has a rhombohedral unit cell which belongs to the $R\overline{3}m$ space group symmetry[22]. This unit cell contains five atomic layers which forms a Te-Sb-Te-Sb-Te stacking sequence along the z-axis called a quintuple layer (QL)[23]. Within QLs, strong covalent bonds exist between Sb and Te ions. Between QLs, weak van der Waals interactions helps hold QLs together[24]. Theoretical calculations have shown that Sb_2Te_3 is a narrow-gap semiconductor and spin–orbit coupling plays an important role in its band structure[25, 26]. Also Sb_2Te_3 is reported to be a topological insulator[25].

$Ge_2Sb_2Te_5$ can exist in three different forms: i) a stable crystalline hexagonal phase (of space group symmetry $P\overline{3}m1$); ii) a metastable, crystalline cubic phase with the

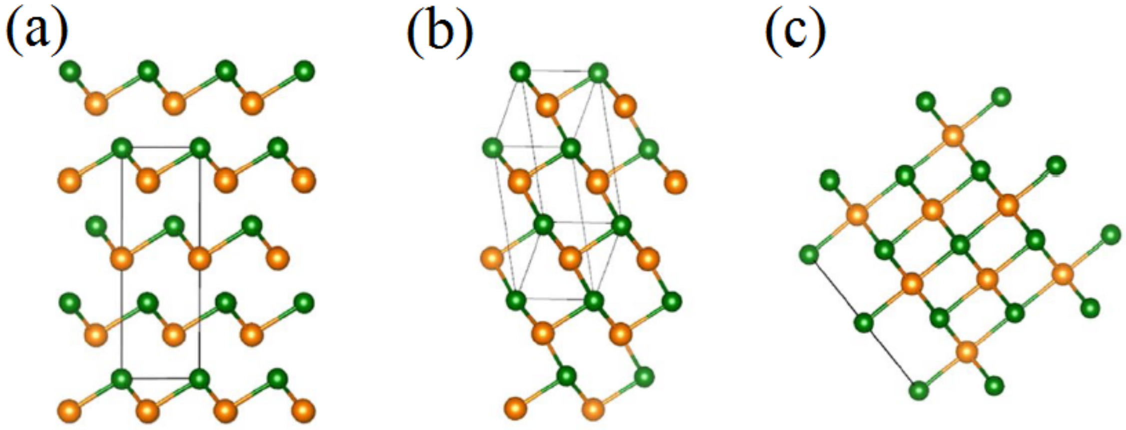

Figure 2-3: Crystal structures of GeTe material with (a) $R3m$ symmetry, hexgonal, (b) Cm symmetry, monoclinic, (c) $Fm\overline{3}m$ symmetry, cubic. The R3m structures feature three short and three long bonds. The Cm structure features two short, two intermediate, and two long bonds. The Fm3m structure features six identical bonds.. Modified from [15].

rock-salt like structure (of space group symmetry $Fm\overline{3}m$); and iii) an amorphous phase [2]. The crystalline hexagonal phase shows low electric resistivity but high optic reflectivity and the amorphous phase shows high electric resistivity but low optic reflectivity[8]. The transition from the ordered to the disordered phase has been of particular interest as it is accompanied by a metal-to-insulator transition (MIT), relevant to the SET-RESET functions[7, 1]. At present, most work on this system has focused on thin films or nano-particles [27, 28, 29, 30, 31]; GST-225 in bulk form hasn't been deeply researched. Another remaining problem in GST-225 research is that how the MIT occurs is not well understood. As we know, a critical feature associated with rewritable, high-density recording is the amorphous phase stability[1]. If the amorphous high-resistivity state is not stable, the data stored on these amorphous data bits will not last long enough, and thus the memory device becomes volatile. A typical non-volatile random access memory requires data to be stored for more than 100∼200 years as to exceed the average human life span. This requires the candidate phase change material to have a stable amorphous phase, but the phase transition must also be triggered easily, rapidly, and at a low energy cost. Doping with Se as in $Ge_2Sb_2Se_{5x}Te_{5-5x}$ (GSST-225) allows access to the amorphous phase via much slower quenching rates in bulk crystalline samples, allowing the electrical properties coupled to this transition to be investigated in bulk materials.

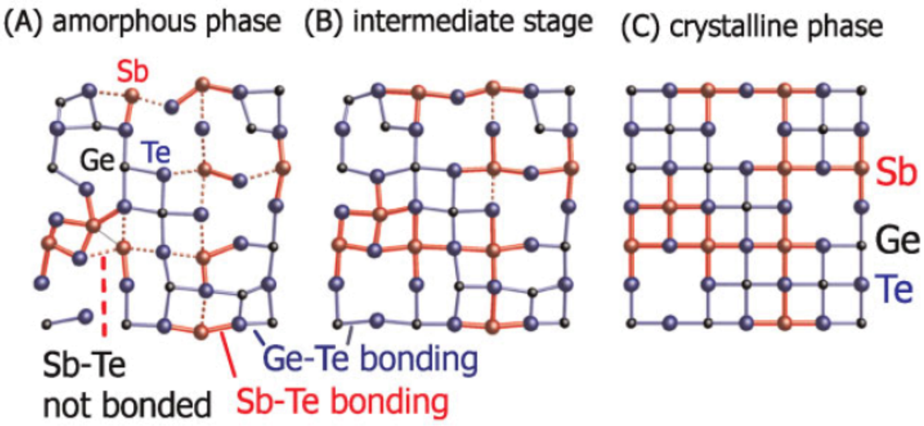

Figure 2-4: Schematic crystal models for Ge-Sb-Te material during its crystallization process: (a) amorphous phase; (b) intermediate metastable phase; (c) crystalline stable phase.[2]

2.1.3 Different Layer Stacking of $Ge_2Sb_2Te_5$

Up to now, many works have been published discussing the crystal structures[32, 33, 10, 34] and different layering stacking models[9, 35, 36, 37, 38, 39, 40] of GST-225. The hexagonal phase of $Ge_2Sb_2Te_5$ has a nine-layered (nonuple) unit cell. Four different polymorphic structures have been discussed in the context of thin films: Ferro, Kooi, Petrov, and inverted-Petrov[36, 37, 39, 40]. Although the differences between these four layer stackings may appear complex, their structures can be reduced to two fundamental stacking layers as to assemble the whole structure. For example, in the Ferro stacking, the layer sequence is {Te-Sb-Te-Sb-Te}-{Ge-Te}-{Ge-Te}-{Te-Sb-Te-Sb-Te}. This structure has a middle double layer made of {Ge-Te}-{Ge-Te} and a quintuple layer of {Te-Sb-Te-Sb-Te} at both ends. The van der Waals interlayer boundaries within these polymorphs are between Sb_2Te_3 QLs and GeTe middle layers. The middle double layer and quintuple layer alternate along the z-direction of unit cell. In the Petrov and inverted-Petrov structures, the middle double layer sequence is different from the Ferro structure. Instead, it is {Ge-Te}-{Te-Ge} for the Petrov and {Te-Ge}-{Ge-Te} for the inverted-Petrov. Through an umbrella-flip transition which switches the {Ge-Te} layer to {Te-Ge} layer, the Ge and Te atoms move along $+z$ and $-z$ directions respectively, until they switch their z coordinates. This transition only needs a small amount of energy to be triggered[37], rendering the three polymorphs equally likely to be present in the material. In the Kooi polymorph, the Ge atoms in the middle double layer is switched with the Sb atoms in the quintuple layer which is energetically more costly than the umbrella flip transition of the other three structures.

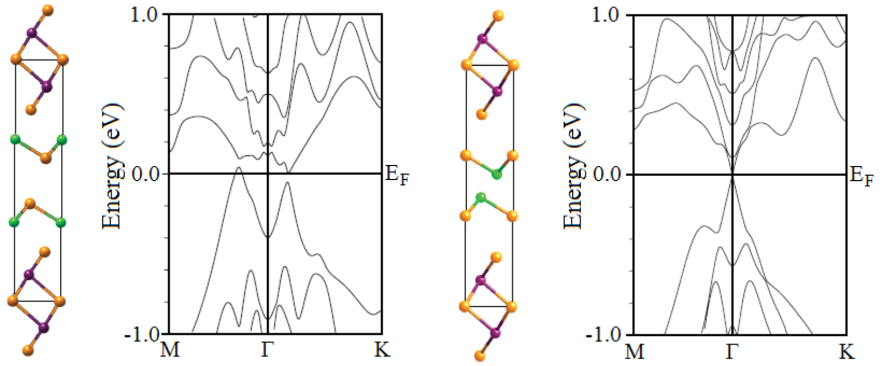

(a) Petrov

(b) Inverted Petrov

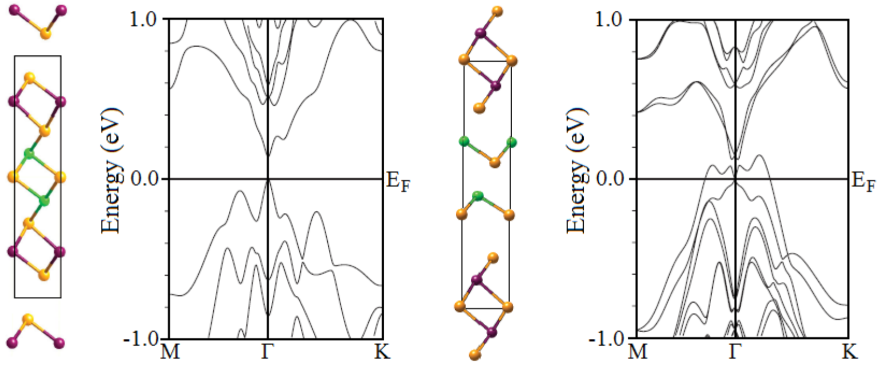

(c) Kooi

(d) Ferro

Figure 2-5: Four different layer stacking of $Ge_2Sb_2Te_5$. Shown in figures are (a) Petrov structure, (b) Inverted Petrov structure, (c) Kooi structure and (d) Ferro structure. Ge atoms are marked in green, Sb atoms are marked in purple, and Te atoms are marked in orange. Next to these structures are their corresponding band structures from first-principles computation. Modified from [36].

From first-principles calculation, the band structures of these four different layer stacking structures can be calculated. The calculation results are shown in Fig. 2-

5. These calculations suggest that these four polymorphs have different topological properties. For example, in Tominaga et al.s calculation[36]: the Petrov structure shows a bulk insulator band structure; the Inverted Petrov structure shows a band structure very similar to a Dirac semimetal; the Ferro structure shows a band structure very similar to a Weyl semimetal; and the Kooi structure shows a topological insulator band structure[36]. From this discussion above, the topological properties of $Ge_2Sb_2Te_5$ can be tuned by a certain choice of layer stacking sequence.

2.2 Topological Properties

Beyond the rich physics of the structural, electronic, and optical properties of $Ge_2Sb_2Te_5$, recent theoretical studies of Ge-Sb-Te based phase change materials also reveal a role for topology. When GeTe and Sb_2Te_3 sub-layers are separated and forms thin layers with thickness of several nanometers, a new superlattice structure which is called interfacial phase change memory (iPCM) forms with interesting physical properties in surface states[41]. An evolution of Fermi arcs and Weyl points can be seen with different termination layers of this material. Different from conventional phase change material which exploits the contrast of physical properties between crystalline and amorphous phases, iPCM remains in its crystalline phases both for SET and RESET states. So the electronic resistivity and optical reflectivity changes before and after the SET-RESET transition is not so large compared with conventional PCM.

Fig. 2-6 shows the crystal structures and band structures of RESET and SET phases in iPCM. The RESET structure has a middle layer consisting of Te-Ge-Ge-Te which corresponds to the inverted-Petrov structure in conventional PCM. The SET structure has a middle layer consisting of Ge-Te-Ge-Te which corresponds to the Ferro structure in conventional PCM. Their band structures also show a large difference due to layer switching. This is desirable because only a small amount of energy is needed to trigger this phase transition[42, 43].

Fig. 2-7 shows the surface states of Ge-Te-terminated and Sb-Te-terminated iPCM as a function of vacancy layer thickness. Different terminations bring different band structures shown in Fig. 2-7(a) and (b). The band structure of Ge-Te-terminated iPCM shows Weyl nodes. Within the first Brillouin zone, along the $\overline{M} - \overline{\Gamma}$ line, an energy gap is observed, while on route $\overline{\Gamma} - \overline{K}$, it's gapless due to a pair of Weyl nodes connected by Fermi arc across $\overline{\Gamma} - \overline{K}$ line shown in Fig. 2-7(d). Due to symmetry, there are, in total, six pairs of Weyl nodes connected by Fermi arcs. The band structure of Sb-Te-terminated iPCM is gapless along both $\overline{M} - \overline{\Gamma}$ and $\overline{\Gamma} - \overline{K}$ lines. This indicates a closed loop on the Fermi surface as shown in Fig. 2-7(g). In Ref. [41], due to the difference in the z-lattice constants of the SET and RESET phases, they assume that the van der Waals bonding is mostly affected by external strain. The vacancy layer thickness t is defined as the empty spacing distance between the Ge-Te layer and the Sb_2Te_3 layer (see Fig. 2-6(b)) which is related to the interlayer spacing. Its value relative to equilibrium, $\Delta t = t - t_{eq}$ can be used to measure the extent of the evolution of Weyl nodes and the Fermi arcs on Fermi surface of iPCM since the topology of Fermi surface is dependent on the t value. From Fig. 2-7 (c)-(f) and (g)-(j), with the value of Δt increasing, Weyl nodes belonging to the same pair move farther away from each other, making the Fermi arcs connecting them longer and longer. Distinctive behaviors on band structure evolution are observed in Ge-Te-terminated and Sb-Te-terminated iPCMs.

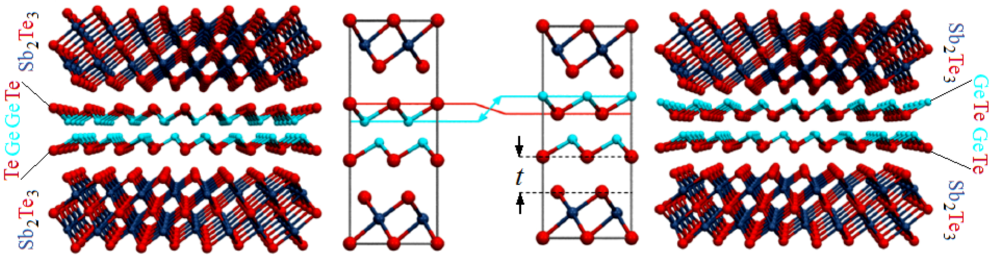

(a) RESET iPCM Phase (Inverted Petrov)

(b) SET iPCM Phase (Ferro GeTe)

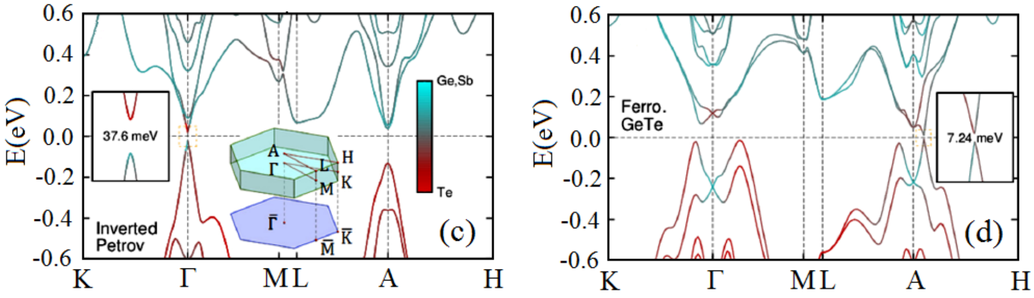

Figure 2-6: Figures (a) and (b) show crystal structures of RESET and SET phases of iPCM. The RESET phase of iPCM (of stacking: Sb_2Te_3-Te-Ge-Ge-Te-Sb_2Te_3) corresponds to the inverted-Petrov structure in conventional PCM. The SET phase of iPCM (of stacking: Sb_2Te_3-Ge-Te-Ge-Te-Sb_2Te_3) corresponds to the Ferro-GeTe structure in conventional PCM. An umbrella flipping of Ge-Te layers could trigger the structural transition between RESET and SET phases by low activation energy. Figures (c) and (d) shows the bulk band structures of RESET and SET phases on high symmetry K-point lines along $K-\Gamma-M-L-A-H$. A schematic plot of the first Brillouin zone is shown in the insert in Fig. (c). Fermi level is chosen to be 0 eV. The band structures in figure (c) and (d) are plotted with dotted lines colored in red or cyan which correspond to the anion or cation states. A close look at the band gaps are shown in inserts in figure (c) and (d) respectively. Modified from [41].

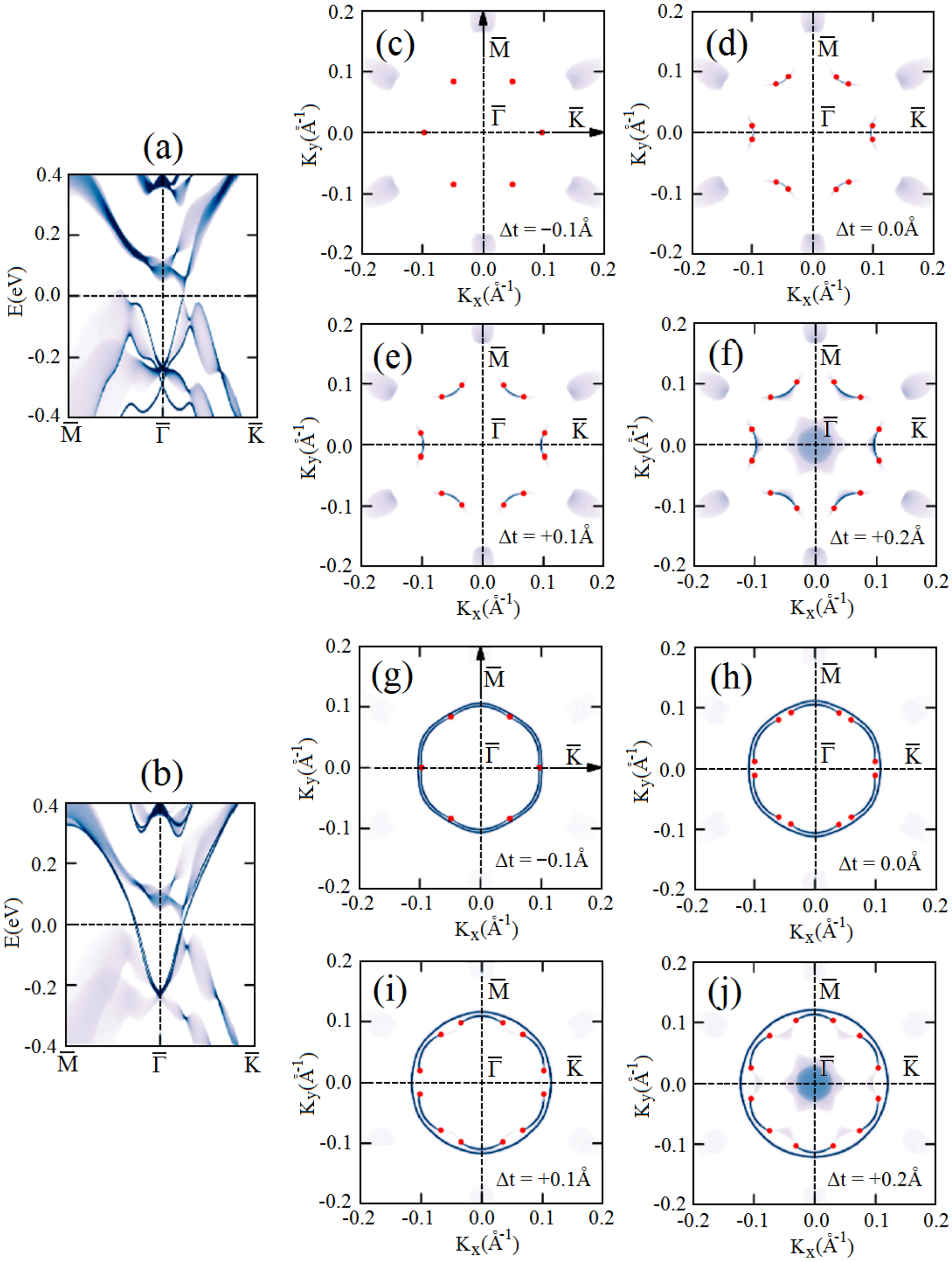

Figure 2-7: Calculated patterns of (001) surface states of interfacial phase change material $Ge_2Sb_2Te_5$. Plots (a) and (b) show band structures for Ge-Te-terminated and Sb-Te-terminated materials. Plots (c)-(f) and (g)-(j) show Fermi surface evolution of Ge-Te-terminated and Sb-Te-terminated materials as a function of the change of vacancy layer thickness from its equilibrium value respectively. Red dots on patterns show the Weyl nodes projected on the surface of Brillouin zone. Modified from [41].

2.3 Switching Properties

In industry, non-volatile phase change material data storage devices utilize the large contrast between the crystalline phase and amorphous phase in electric resistivity and optical reflectivity. A SET and RESET switching mechanism can be established according to this principle. The SET status is defined as the process of writing a logical bit '1' and is associated with the amorphous-to-crystalline phase transition, while the RESET status is defined as the process of writing a logical bit '0' and is associated with the crystalline-to-amorphous phase transition[3].

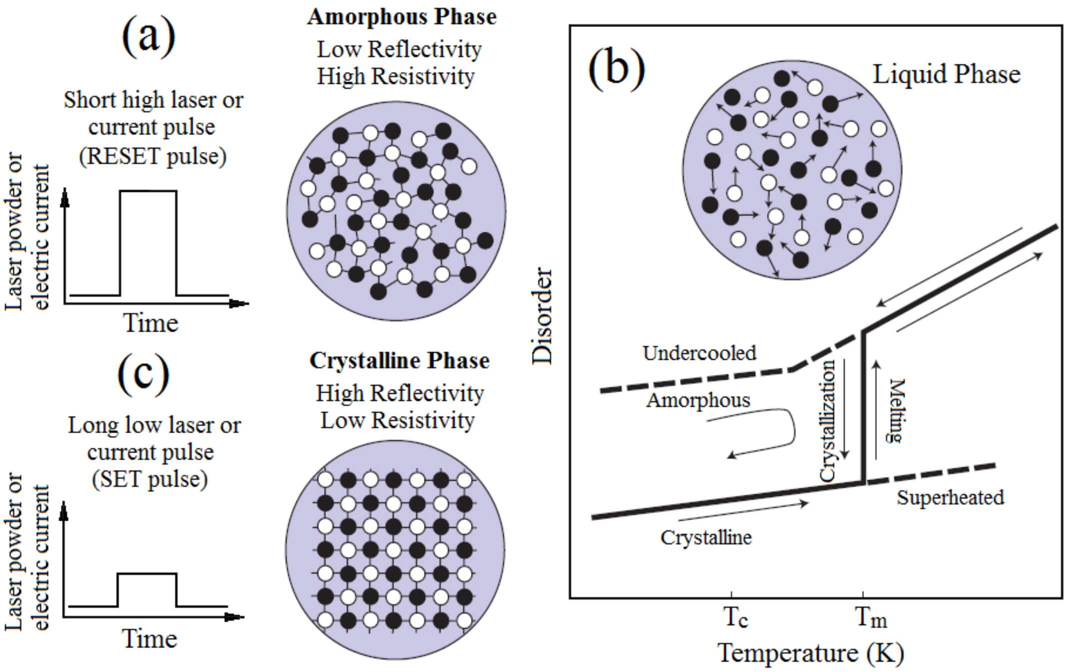

Figure 2-8: A figure showing the SET-RESET status transition within the data storage devices using phase change material. In figure (a), a short, high-intensity laser beam is used to heat the phase change material locally. The phase change material is heated over its melting temperature T_m so as to liquefy the material. In figure (b), a fast cooling process quenches the material from liquid phase back into a disordered amorphous phase. In figure (c), a long, low-intensity laser beam is used to heat the phase change material over its crystallization temperature T_c. The atoms within material become mobile and transfer back into its crystalline phase which is more energetically favourable. Modified from [1].

The SET/RESET switching is usually accomplished through Joule heating or laser annealing locally on the surface of phase change material within the data storage devices[44]. As shown in Fig. 2-8, a RESET pulse is used to heat the phase change material over its melting temperature T_m. This process will transform material into its liquid state where atoms within the material are in a disordered arrangement. Then a fast quenching process will stabilize the liquid state into an amorphous solid state. During quenching, the cooling rate is very high ($\sim 10^9 K/s$). In industry, it is not possible to heat a large portion of the material and transform it into a bulk amorphous material. However, nanoscale regions naturally cool very rapidly, due to a high surface-area-to-volume ratio. Because GST crystallizes so rapidly, we need a very rapid cooling rate for the amorphous phase. Such a high cooling rate can only be achieved on the nanoscale. Thus, bulk amorphous GST cannot be created, and electronic devices grow the material in thin film form. Electronic devices such like those using $Ge_2Sb_2Te_5$[8] grow the material in thin film form. Only a small portion of the sample surface is heated and is amorphized, forming a small amorphous dot on the material surface. The small size of these dots is beneficial for high data storage density. After amorphization, a SET pulse is used to heat the amorphous material over its crystallization temperature T_c. Since the crystallization temperature T_c is lower than the melting temperature T_m, this will transform the material into a state where the atoms are mobile but not so fluid as to become liquid. Atoms will reorganize themselves into a crystalline phase which is more energetically favorable, forming a complete cycle for switching between the crystalline and amorphous phases.

The process for crystallization is much slower than amorphization in phase change materials[3]. Since the process for crystallization is much slower than amorphization, shorter pulses are used for RESET switching and longer pulses are used for SET switching. A typical RESET pulse for phase change materials usually has a time scale of 30∼50 ns, and a SET pulse usually has time scale of 100∼200 ns (see Fig. 2-9). Also, since $T_m > T_c$, the RESET pulse is also of higher intensity than the SET pulse, since more energy is required for a laser to heat the material to a higher temperature. The short RESET pulse also functions as a method of fast quenching. For crystallization, the SET pulse keeps the sample at a temperature T ($T_c < T < T_m$) long enough for atoms within material to have adequate time to reorganize themselves into crystalline state. The RESET pulse, on the other hand, is high enough to transform material into a liquid state, and short enough that atoms in the liquid don't have enough time to reorganize themselves into a crystal structure, giving the rise of an amorphous state.

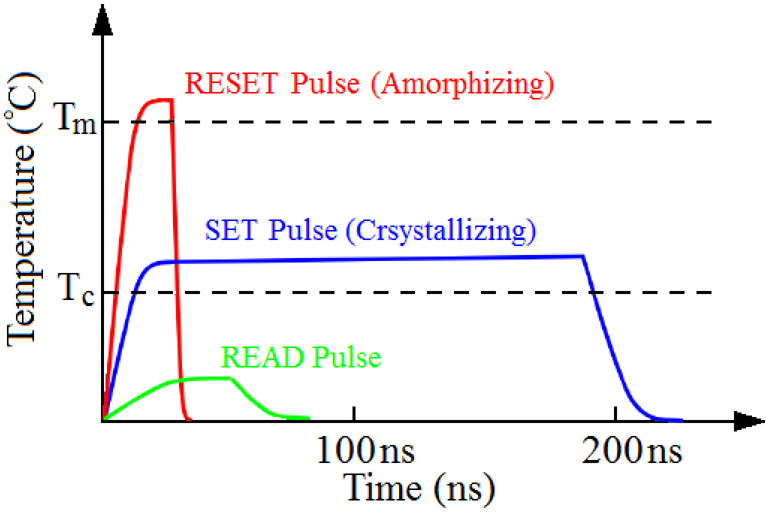

Figure 2-9: A figure showing the typical time duration for RESET, SET and READ laser pulse which used in data storage devices with phase change materials. Modified from [3].

2.4 Local Structure Properties

The local structure of amorphous $Ge_2Sb_2Te_5$ is also an interesting research topic. In work done by et al. in 2004[45], EXAFS (Extended X-ray Absorption Fine Structure) spectra data of $Ge_2Sb_2Te_5$ were published (shown in Fig. 2-10). EXAFS K-edge data shows a comparison of the Ge-, Sb- and Te- bond lengths within crystalline and amorphous phases which is useful for understanding the local structure within amorphous state. According to the K-edge data, atomic bonds get shortened and a local structure is discovered in amorphous $Ge_2Sb_2Te_5$. They proposed a schematic crystal structure model for laser-amorphized $Ge_2Sb_2Te_5$ based on their discoveries (shown in Fig. 2-11).

In the model shown in Fig. 2-11, thick lines join the atoms which from the building blocks of $Ge_2Sb_2Te_5$ structure. Small green arrows indicate the deviations of atomic positions away from the ideal cubic structure. Ge-Te and Sb-Te bonds get shortened

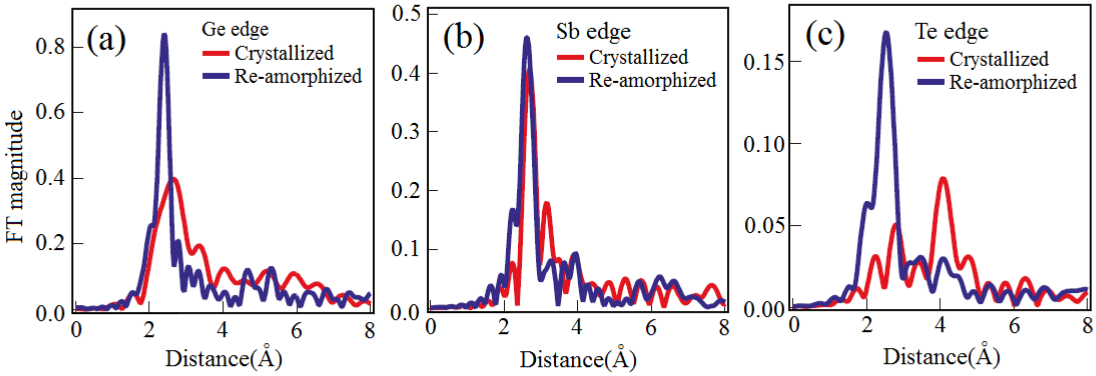

Figure 2-10: Fourier-transformed EXAFS spectra of $Ge_2Sb_2Te_5$ material in its crystallized and re-amorphized phases. Fig. (a), (b) and (c) show the K-edges of Ge, Sb and Te atoms respectively. It is worth mentioning that the r-space data isn't real-space radial distribution function data. Data represents the magnitude of the Fourier transformation in K-Space. Peak positions on patterns are shifted compared with the actual inter-atomic distances. Modified from [45].

due to this umbrella flipping transition which provides an explanation of EXAFS data[45]. On the other hand, this local structure within the amorphous phase is not unique for $Ge_2Sb_2Te_5$. In amorphous thin-film GeTe, a similar case is found within this material[46]. It is presumed that all Ge-Sb-Te based phase change material share this trait as long as they can be made amorphous.

Shown in Fig. 2-12 is the measured and simulated Ge-edge XANES (X-ray Absorption Near Edge Structure) spectra for $Ge_2Sb_2Te_5$ material[45]. Fig. 2-12(a) shows the measured XANES data and Fig. 2-12(b) shows the simulated data. Both crystallized and re-amorphous $Ge_2Sb_2Te_5$ materials are used for measurements and their data are shown in red and blue curves respectively. In simulation, Ge atoms were allowed to acquire their preferred atomic locations. If the Ge position changes from octahedral to tetrahedral coordination, part of the experimental data features are reproduced (see between Fig. 2-12(a) and Fig. 2-12(a)). The difference in amplitudes of the peak features is due to the thermal damping[45]. These data provide evidence that in amorphous $Ge_2Sb_2Te_5$, the atomic arrangement is more compact compared with the crystalline phase. When the local distortion of Ge atoms change its octahedral coordination to tetrahedral, Ge-Te bonds get shortened[45].

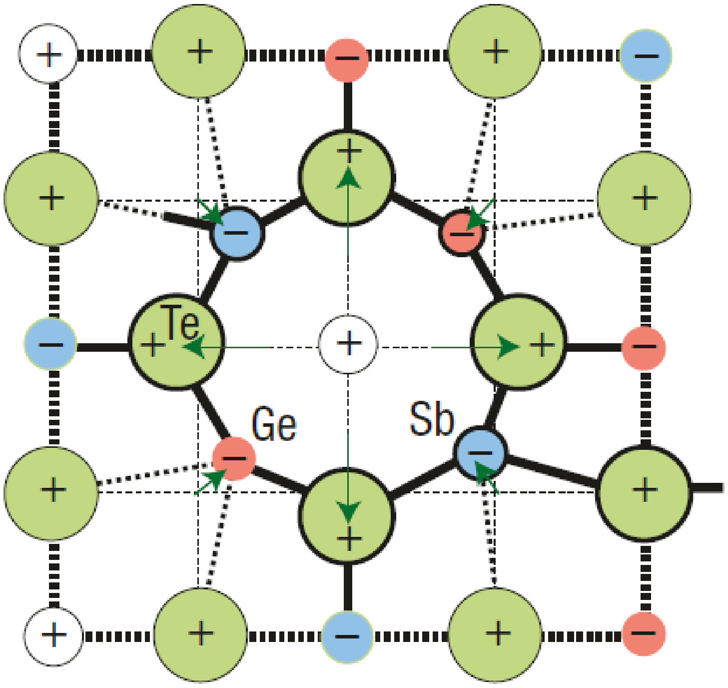

Figure 2-11: A schematic two dimensional image of the crystal lattice of distorted $Ge_2Sb_2Te_5$. [45].

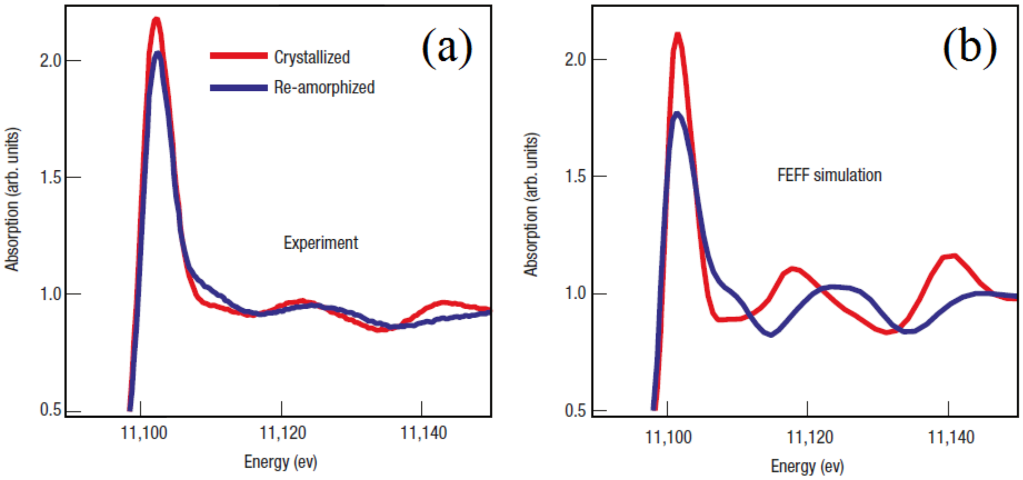

Figure 2-12: Measured and simulated Ge-edge XANES spectra for $Ge_2Sb_2Te_5$ for the crystalline and amorphous states. [45].

Chapter 3

Experimental Methods

3.1 Experimental Techniques

3.1.1 Resistivity Measurement

The temperature-dependent resistivity measurements on GSST samples shown in Chapter 6 were done on PPMS (Physical Property Measurement System). The conventional four-probe technique was used for mounting samples on resistivity puck. Shown in Fig. 3-1 is a schematic figure of experimental equipment for PPMS resistivity measurements. Before measurement, the sample should be mounted on the surface of a PPMS puck. Four platinum wires (0.025 mm in diameter) were used to make connections between the sample surface and the electric nodes on PPMS puck. Silver epoxy with fast drying ability were used to attach the platinum wires onto the surface of the sample. Another method of fast making connections is using the indium wires. When pressed, a small segment of indium wire can be attached onto the sample surface. A small tool with sharp tip could help connecting the platinum wire and make contacts. Between platinum wire and electric nodes, soldering tin is used to make contacts. Note that the base of resistivity puck is conducting, so an insulating layer like Kapton film should be used to separate sample's bottom surface and resistivity puck.

Samples' dimensions should also be recorded before the measurement starts. In most times, the shapes of GSST bulk polycrystal samples are irregular. This will bring difficulties in experiments in following two ways. First, the cross section area and length of the sample are hard to calculate. Second, it will be difficult to mount four contacts on irregular or rough sample surfaces. To solve these issues, a reasonable cut on the sample trying to get flat surfaces should be performed. Polishing the sample surface could also amend the rough surface. When measuring the dimensions, a microscope with length scale should be used, and multiple measurements should be taken to get the average value of a measured quantity.

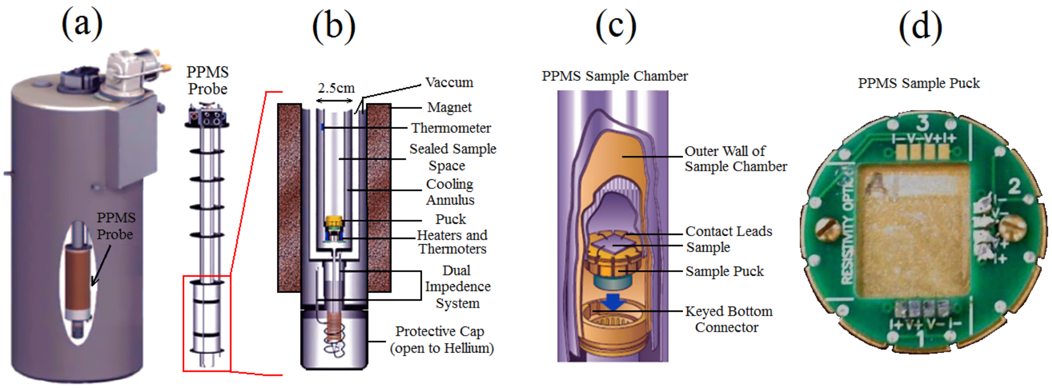

Figure 3-1: A figure showing the PPMS experiment equipment. Fig. (a) shows a picture of PPMS dewar. Fig. (b) shows a cross section of PPMS probe. Fig. (c) shows a schematic picture of sample chamber. Fig. (d) shows the top view of a PPMS resistivity puck. Modified from [47].

After sample mounting, it is reasonable to do a resistivty check before it's put into PPMS. A user resistivity bridge/sample test box along with a multimeter could give a rough resistivity measurement out of PPMS sample chamber. If the reading is reasonable, the resistivty puck can be put into the PPMS sample chamber with the help of a tool. Several purge cycles should be performed in order to get ideal vacuum. Then, a software called MultiVu[48] can assist us writing a programmed file for setting temperature run and measurement parameters. A typical resistivity measurement of GSST samples takes around 6-7 hours, Matlab[49] data analysis software was used to process resistivity data and generate corresponding plots.

3.1.2 Differential Scanning Calorimetry (DSC) Measurement

Differential Scanning Calorimetry (DSC) method is an experimental technique which can be used to analyse sample's thermal properties. DSC is popular in studying the thermal transition in polymer materials. This technique was developed by E. S. Watson and M. J. O'Neill in 1962[50]. Fig. 3-2 shows a schematic plot of the measurement chamber of a DSC experimental instrument. Before measurement, a sample piece should be cut and weighed before put into the chamber. The sample mass is recommended to be between 10mg$\sim$100mg. Next, the sample piece should be encapsulated in an aluminum pan with cap. The same procedure should be done with the reference material. Several inert inorganic substances are recommended for standard reference materials used in DSC and DTA (Differential Thermal Analysis) measurements, for example, aluminum oxide (alumina, Al_2O_3), silica (SiO_2) and KNO_3. The reason for choosing alumina is because alumina has no phase transformation between room temperature and its melting point of 2050°C. And also alumina doesn't readily adsorb water, no dehydration on the surface of the sample will happen during heating. For DSC measurement, its reference can be an empty pan. In case the baseline problem happens during experiment, the reference material discussed above can be added to balance the sample. Due to the melting point of aluminum of 660°C, the chamber temperature should never goes above 600°C in case the encapsulated pan melts.

A protective gas like argon should be flowing through the heating chamber during experiment in order to isolate the sample with air atmosphere so as to avoid oxidation. Usually the chamber will be kept at 50°C for further measurements. A software will assist the user in editing the temperature control program. For a temperature scan, the temperature will increase from starting point to end point linearly with a pre-programmed rate. It is useful for checking the onset temperature of a phase transition within a sample. For an isothermal scan, the temperature is held at a certain temperature for a time duration. It is useful for researching the samples' crystallization kinetics.

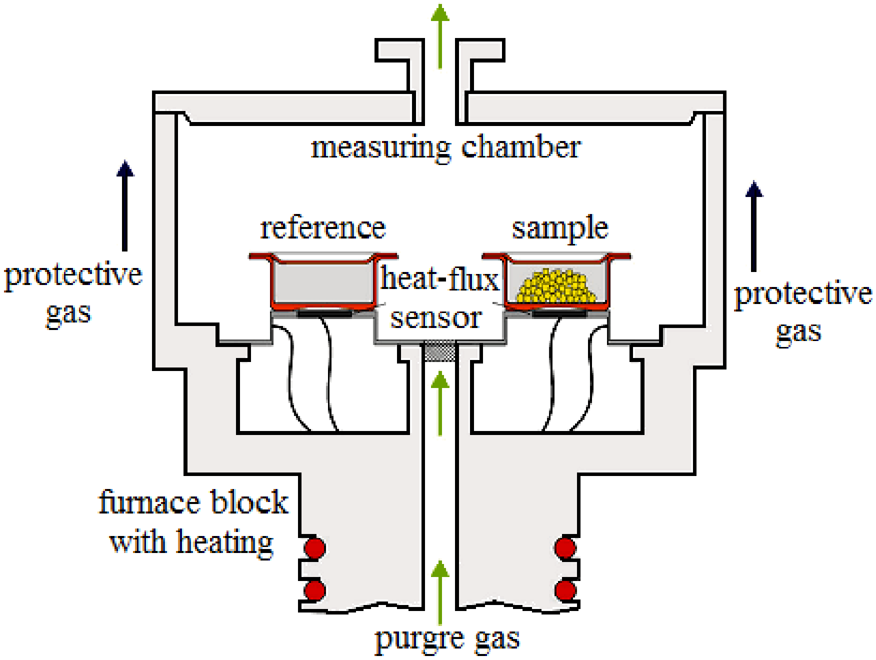

Figure 3-2: A schematic figure showing the measurement chamber of a DSC instrument. Modified from [51].

Fig. 3-2 shows a typical DSC temperature scan pattern. When the DSC measurement is running, the heat flow difference from sample and reference material is recorded as a function as time or temperature. Since the reference material has no transformation under 600°C, no change in heat flow should be observed. If a phase change process is happening within the sample, their difference on heat follow shall be recorded as a peak on the pattern. For example, The red curve in Fig. 3-2 shows a melting process happening on researched sample at around 278°C. A peak pointing up is observed which represents an endothermic process. The blue curve in Fgure. 3-2 shows a phase transition process happening on researched sample at around 218°C. A peak pointing down is observed which represents an exothermic process. The peak area underneath represents the total energy absorbed or released during phase change process and can be used to analyze the crystallization process and extract the value of enthalpy of a glassy material[52].

Before formal measurements, a calibration is needed for a DSC machine if it hasn't been used for a long time. A calibration needs to run two reference materials for a

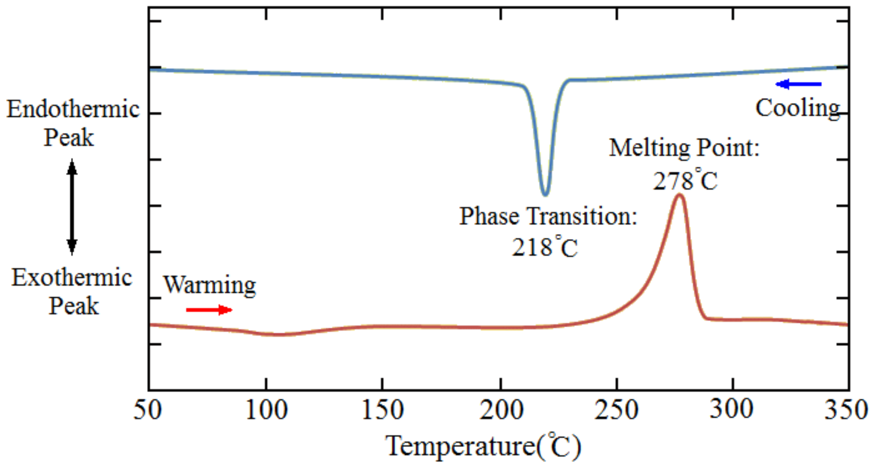

Figure 3-3: A typical figure showing the DSC temperature scans on warming (red) and cooling (blue). An exothermic peak (pointing up) labels the temperature point of melting process. An endothermic peak (pointing down) labels the temperature point of a phase transition.

wide temperature range. Two materials for calibration should be selected from table 3.1 in order to do temperature scans. For example, Zinc and Indium are usually used as calibration materials. For Zinc, a temperature scan from 50°C to 600°C with heating rate 20°C/min should be performed. For Indium, a similar temperature scan from 50°C to 200°C with heating rate 20°C/min should also be done. After both data are collected, the peak positions and peak areas of their exothermic peaks can be extracted, these data can be used to compare with the standard values listed in table 3.1. If an obvious discrepancy between the experimental data and standard values are observed, linear transformations are done both on x-axis and y-axis units of the DSC data pattern in order to compensate the offsets. The transition temperature values can be used to calibrate the temperature axis and the transition energy values can be used to calibrate the heat flow axis.

Calibration Materials	Transition Temperature(°C)	Transition Energy(J/g)
Zinc(Zn)	419.5	108.37
Tin(Sn)	231.9	60.46
Indium(In)	156.6	28.45
Lead(Pb)	327.5	23.01
Potassium Sulfur(K_2S)	585.0	33.26
Potassium Chromate(K_2CrO_4)	670.5	25.56

Table 3.1: A table summarizing the transition temperatures and transition energies of reference materials which can be used to perform DSC calibration. Modified from [53].

3.2 Diffraction Experiment

X-ray was first used to characterize crystal material in 1912 by Laue, Friedrich and Knipping[54]. They were awarded Nobel prize soon after their significant discovery. Nowadays X-ray diffraction is still a powerful method in determining materials' structures especially in crystalline and quasi-crystal materials.

The premise for structural determination with X-ray is that the researched material has spatial periodicity in its structure[55]. If X-ray is radiated on amorphous materials, such as liquid, gas, glass. Reflected X-ray beam will be scattered in all directions and no diffraction pattern with signatures will form. If we can't extract useful information from diffraction pattern, no further structural modeling can be done. If the researched material is in its crystalline state, then diffraction pattern with bright spots or sharp peaks will form. From these patterns, we can use Rietveld refinement method to model the pattern from structure.

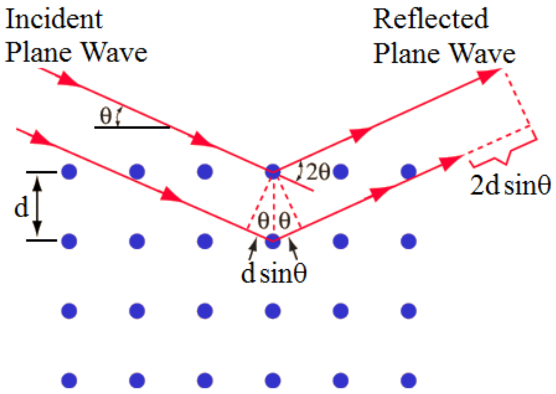

Figure 3-4: A figure showing the derivation process of Bragg's Law. Modified from [56].

The Bragg's law was first introduced in 1913[57], soon after Laue et al's discovery of X-ray's use on crystal diffraction. Although simple, this equation is in a vital position in X-ray diffraction analysis. Shown in Fig. 3-4 is a schematic figure of derivation of Bragg's law. The two reflected X-ray beams with wavelength λ by top first and second layer of atoms within a crystal lattice are traveling in a direction that has an angle of 2θ with the incident beam. If a constructive interference between the two beams is established, a bright spot or sharp peak will form at this direction. This requires that their optical path difference $2d \cdot sin(\theta)$ should be a integer multiple of their wavelength λ. This gives the Bragg's law:

$$n\lambda = 2dsin(\theta) \tag{3.1}$$

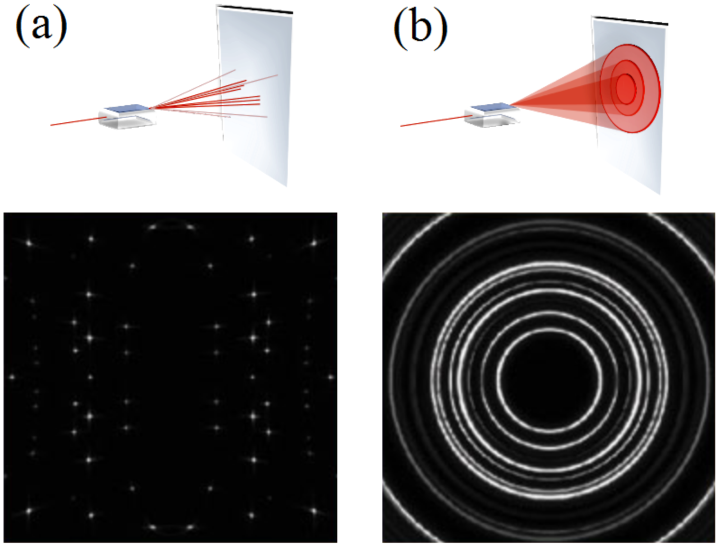

Figure 3-5: A comparison of single crystal X-ray diffraction (a) and powder X-ray diffraction (b). Modified from [55].

Fig. 3-5 shows a comparison of single crystal XRD and powder XRD and their resulting patterns. In single crystal XRD, only a large piece of crystalline lattice appears as the scattering center, several separate characteristic beam lines is diffracted into different orientations so as to form a pattern with bright spots, seen in Fig. 3-5(a). In powder diffraction, several diffraction cones form after X-ray is scattered by the powder material, and a ringed pattern is formed for this situation, seen in Fig. 3-5(b).

A powder sample can be seen as a collection of millions of small crystallites. When ground, large pieces of single crystal or polycrystal material break down into small crystallites, these small crystallites can have spatial orientations in all directions. When the incident X-ray is radiated on these small crystallites, only a small portion of crystallites which have orientations satisfy Bragg's law give constructive interference. Constructive interference brings diffracted beams received by detectors. For example,

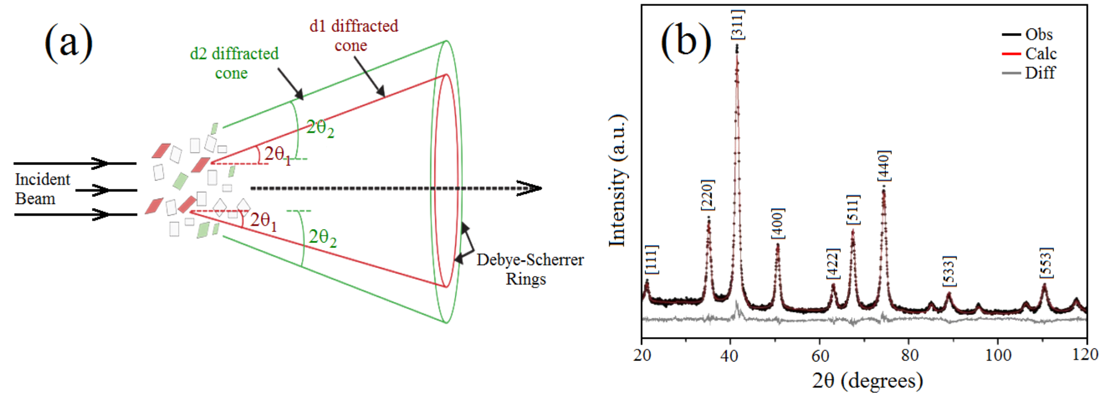

Figure 3-6: Figure (a) shows a schematic plot of the powder diffraction experiment set. Figure (b) shows a powder diffraction pattern generated from (a) for Fe_3O_4 material with peak indices labeled. Modified from [55].

in Fig. 3-6(a), two sets of crystallites (colored in red and green respectively) give direction angles θ_1 and θ_2 which satisfy:

$$n\lambda = 2dsin(\theta_1), m\lambda = 2dsin(\theta_2). \tag{3.2}$$

These two sets of crystallites generate two diffracted beams with angles of $2\theta_1$ and $2\theta_2$ to the incident beam direction (also the direction of black dashed arrow). However, these crystallites still have the freedom of rotating an arbitrary ϕ angle around black dashed arrow. All the crystallites whose direction satisfy $\theta = \theta_1/\theta_2$, $\phi =$ arbitrary angle can give diffraction beams. These diffraction beams merge into two diffraction cones (as shown in Fig. 3-6(a)) and form a pattern of concentric rings when they are projected onto the screen which is perpendicular to the incident beam. In XRD machine, the detectors usually takes signals in a trajectory in θ direction (see Fig. 3-7), it goes across different diffraction cones and record every cone as a diffraction peak on powder XRD pattern (as shown in Fig. 3-6(b)).

In ideal situation, the small crystallites within a powder sample are randomly oriented so that their orientations are evenly distributed across all directions. But chances are that these crystallites may have asymmetric shapes (for example, needle-like or disc-like shapes) due to their inner chemical ordering[58]. This will cause an uneven distribution of orientations in which crystallites face. In some certain directions, like z-direction, there will be less/more crystallites face which is called the preferred orientation. In preferred orientation, the intensities of a set of peaks which has the same orientation indices like [001], [002], [003], ... will be tuned be a factor. In a more complex situation where a more uneven distribution happens, a spherical harmonics function with four parameters h, k, l, ratio is applied in GSAS to simulate the effect caused by preferred orientation on XRD pattern[59].

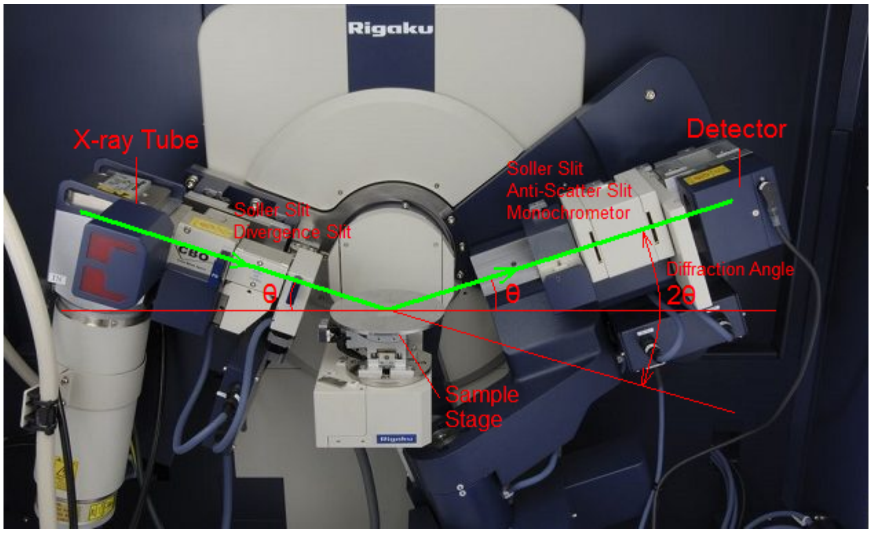

Figure 3-7: A figure showing the main working parts of RIGAKU X-ray diffraction machine. From left to right: (1) X-ray tube, generates incident X-ray beam; (2) Divergence Slit, limits the axial (perpendicular to paper plane) divergence of the incident X-ray beam; (3) Sample stage, holds the glass plate where powder sample is put on; (4) Receiving slit/anti-scatter slit, limits the axial (perpendicular to paper plane) divergence of the diffracted X-ray beams; (5) Monochrometor, provides a monochromatic source of x-rays; (6) Detector, receives the diffracted X-ray beam intensity signal. In this XRD machine's geometry, when it's running, sample stage is fixed, both X-ray tube and detector parts are moving in θ direction toward up-direction to create 2θ diffraction angle.

Every X-ray diffraction peak can be labeled with a set of (hkl) indices which is called the Miller index[60]. In crystallography, a set of parallel lattice planes can be determined by three integers h, k, l. This set of lattice planes are all perpendicular to the reciprocal lattice vector: $\boldsymbol{G} = h\boldsymbol{b_1} + k\boldsymbol{b_2} + l\boldsymbol{b_3}$. By convention, negative miller indices such like -1 and -2 are written as $\bar{1}$ and $\bar{2}$.

As discussed above, the peak positions of a X-ray diffraction pattern is determined by Bragg's law (see equation. 3.1). On the other side, the peak intensities of diffraction peaks can be described by following empirical formula[58]:

$$I_{hkl} = C \cdot S \cdot \frac{M_{hkl}|F_{hkl}e^{-2M}|^2}{sin(\theta_{hkl})sin(2\theta_{hkl})} + background \tag{3.3}$$

Here, C is a factor relative to instrument parameter. S is a factor relative to the amount of the sample, which is called the scaling factor. M_{hkl} is the multiplicity factor, it will count for all the Miller indices which are symmetrical equivalent[58]. For example, for a miller index has format (hhh), M_{hhh} equals 8, since both h and $\overline{h}$ are taken into consideration. So we have total 8 possible combinations:

(hhh), ($\overline{h}$hh), (h$\overline{h}$h), (hh$\overline{h}$), (h$\overline{h}\overline{h}$), ($\overline{h}$h$\overline{h}$), ($\overline{h}\overline{h}$h), ($\overline{h}\overline{h}\overline{h}$).

For a miller index like (hkl), M_{hkl} equals 48. This is because not only the multiplicity brought by symmetry equivalence of h and $\overline{h}$ should be accounted for, the multiplicity caused by permutation of (hkl) (h≠k≠l) should also be counted:

(hkl), (hlk), (klh), (khl), (lhk), (lkh).

A table summarizing the results of multiplicity factor is listed in table 3.2.

Miller Indices	M_{hkl}	Miller Indices	M_{hkl}
(h k l)	48	(h h 0)	12
(h h k)	24	(h 0 0)	6
(h h h)	8	(0 0 0)	1
(h k 0)	24		

Table 3.2: A table summarizing the values of multiplicity factor M_{hkl} with respect of different Miller index (hkl) format. Note: here h≠k≠l≠0.

F_{hkl} is the structure factor, which can be calculated from the atomic structure factors and the atomic positions within the unit cell, its formula is shown as follows:

$$F_{hkl} = \sum_j f_j e^{i\boldsymbol{L}\cdot\boldsymbol{G}} = \sum_j f_j e^{2\pi i(hx_j+ky_j+lz_j)} \tag{3.4}$$

In this equation, j is the index for different atoms within a unit cell. The sum is taken to go over all j in order to take consideration of contributions of all atoms to the final structure factor. The lattice vector and reciprocal lattice vector are expressed as: $\boldsymbol{L} = x_j\boldsymbol{a_1} + y_j\boldsymbol{a_2} + z_j\boldsymbol{a_3}$ and $\boldsymbol{G} = h\boldsymbol{b_1} + k\boldsymbol{b_2} + l\boldsymbol{b_3}$, which satisfy:

$$\boldsymbol{a_i} \cdot \boldsymbol{b_j} = 2\pi\delta_{ij} \tag{3.5}$$

Atomic factor f_j is dependent on the atomic species and direction of scattering and independent of the atomic positions within the unit cell. It is a measure of the X-ray scattering power of each atom[61]. If the atomic factor f_j is replaced by neutron scattering length b_j of each atomic species in equation 3.4, which gives:

$$F_{hkl} = \sum_j b_j e^{i\boldsymbol{L}\cdot\boldsymbol{G}} = \sum_j b_j e^{2\pi i(hx_j+ky_j+lz_j)} \tag{3.6}$$

This is the structure factor for neutron diffraction which can be used in neutron diffraction analysis. From the similarity between equation 3.4 and 3.6, it is no hard to infer that in most cases, the X-ray diffraction pattern and neutron diffraction pattern of the same material should bear some similarities. Their peak positions should be the same but with different peak intensities. However, due to the different scattering mechanism of X-ray electrons and neutrons, X-ray diffraction and neutron diffraction provide different parts of structural information of materials. X-ray diffraction is suitable for superficial diffraction analysis, since the X-ray are mainly scattered by electrons surrounding the nuclei. Neutrons have deep penetration depth and can reflect the the structural information of atomic nuclei and magnetic momentum[62].

The term e^{-2M} is the Debye Waller factor. This attenuates the peak intensity because of the thermal motion of the atoms. The term on the denominator $sin(\theta)sin(2\theta)$ comes from the angular contribution of the peak intensity. The last term is the contribution of the background which is dependent on the sample environment and instrument condition.

GSAS (General Structure Anlysis System)[59] is a integrated software package which can be used to do Rietveld refinements. Old versions of GSAS can only accepts typed commands, with the help of EXPgui[63], new versions of GSAS can be operated through a graphical interface which is more user-friendly. Fig. 3-8 shows a screen shot of the user interface of GSAS software package.

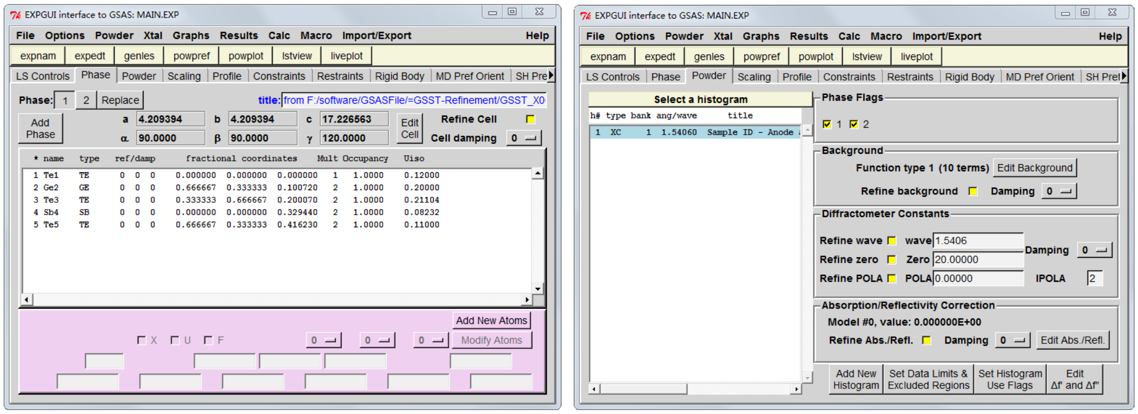

Phase: 1 2

title: from F:/software/GSASFile/=GSST-Refinement/GSST_X0

a 4.209394 b 4.209394 c 17.226563

α 90.0000 β 90.0000 γ 120.0000

Refine Cell ☐

Cell damping 0

```
 * name   type  ref/damp    fractional coordinates    Mult Occupancy  Uiso
 1 Te1    TE     0  0  0   0.000000  0.000000  0.000000   1   1.0000   0.12000
 2 Ge2    GE     0  0  0   0.666667  0.333333  0.100720   2   1.0000   0.20000
 3 Te3    TE     0  0  0   0.333333  0.666667  0.200070   2   1.0000   0.21104
 4 Sb4    SB     0  0  0   0.000000  0.000000  0.329440   2   1.0000   0.08232
 5 Te5    TE     0  0  0   0.666667  0.333333  0.416230   2   1.0000   0.11000
```

```
h# type bank ang/wave      title
 1  XC     1  1.54060  Sample ID - Anode
```

Phase Flags

☑ 1 ☑ 2

Background

Function type 1 (10 terms)

Refine background ☐ Damping 0

Diffractometer Constants

Refine wave ☐ wave 1.5406

Refine zero ☐ Zero 20.00000

Refine POLA ☐ POLA 0.00000

Damping 0

IPOLA 2

Absorption/Reflectivity Correction

Model #0, value: 0.000000E+00

Refine Abs./Refl. ☐ Damping 0

Figure 3-8: A figure showing the user interface tabs of GSAS software package[63].

Many input parameters can be tuned in order to get a successful fit of the crystal structure model with the diffraction pattern data. Lattice parameters a, b, c, and angles α, β, γ decide what shape of unit cell the researched material have. In most cases, their selection boxes should always be checked during refinement in order to get precise lattice parameters. First refinement attempt could start with refining lattice parameters, as this gives a coarse fitting of peak positions. Remember every peak appearing on the data pattern should have a peak position tick marker underneath generated by crystal model in order for further intensity fits. Unlabeled peaks on data pattern usually means the appearance of a secondary phase or unidentified peaks rising from local distortion. Atomic parameters including x, y, z fractional coordinates, site occupancy and U_{iso} thermal factors of atoms within the unit cell. Fractional coordinates affect both peak positions and peak intensities. Usually they should be refined with the lattice parameters. Site occupancy usually comes from material's stoichiometries, they represent the average number density of atoms occupying atomic sites[59]. Thermal factors attenuate the peak height and broaden the peak width, making the delta function-like peaks transform into Gaussian-like peaks. They cause more damping effect to the high angle peaks compared with to low angle peaks. This can be seen in this equation[58]:

$$e^{-2M} = e^{-2(\frac{2\pi sin(\theta)}{\lambda})^2 U_{iso}^2} \tag{3.7}$$

For a larger value of θ, $sin(\theta)$ is larger, making the whole Debye Waller factor e^{-2M} smaller, so as to cause a larger damping ratio to the peak intensity at high θ angle. At low temperature, atoms usually vibrate evenly in all spatial directions, their displacement area can usually be approached by a sphere. Under this condition, isotropic thermal factors U_{iso}s are adequate for Rietveld refinement modeling. At high temperature, atom's thermal displacement is no longer even in space, a more complex shape like ellipsoid is needed to be used to model the displacement area of an atom vibrates at high temperature. In this situation, a 3×3 array of parameters from U_{11} to U_{33} which are called anisotropic thermal factors are used to model thermal vibration. According to symmetry constraints, U_{ij} equals U_{ji}, only six anisotropic thermal factors are independent. For now, two common sets of units are used to measure the Debye Waller thermal factors, they are U_{ij}s and B_{ij}s. Their relationship is shown in equation 3.8. A conversion is necessary when thermal factors is exported from one software and imported into another, since different software may use different units.

$$B = \frac{8\pi^2}{3}\left\langle U^2 \right\rangle = 8\pi^2 U_{iso}^2 \tag{3.8}$$

The scale factor of total diffraction and phase volume fractions of each phase is listed in the scaling tab. These parameters should always be kept refined and they are deciding the material's phase compositions. The ratio of two phase volume fractions means the ratio of numbers of two types of unit cells belonging to different phases. Diffractometer constants DIFC, DIFA and Zero determines a nonlinear relationship between time of flight t and d-spacing d, which can be written as:

$$t = DIFA * d^2 + DIFC * d + Zero \tag{3.9}$$

In GSAS, several profile functions are provided in order to fit the peak shape due to thermal broadening. Among them, the Gaussian function, Lorentz function, Voigt function and Pseudo-Voigt function are four types of common profile functions used in Rietveld refinement[59]. In each function, around 10∼20 parameters can be refined in order to achieve better fits. For example, in Guassian function, GU, GV, GW, asym, F1, F2, peak cutoff are parameters which can be tuned during a refinement. The contribution from background in intensity is also modeled with several types of functions in GSAS. The shift Chebyschev polynomial function is the most frequently used one. Other types like cosine Fourier series and power series of $Q^{2n}/n!$ and $n!/Q^{2n}$ background functions can be used to fit irregular or wavy instrument backgrounds[59]. Another useful function in GSAS is that users can also manually determine the background by adding points on diffraction pattern, the system will generate background function which approaches to these points.

During a GSAS refinement, refine all the parameters at the same time is unrealistic as this will cause the blow-up of χ^2. A basic refinement strategy is starting from the Lebail refinement as this gives the structural information. The lattice parameters and atomic positions are always the first thing to handle as they give the peak positions. After all peak positions are found and labeled, thermal factors and peak profile factors can follow up and get refined since they affect peak intensities and peak shapes. It is worth mentioning that, the atomic positions and thermal factors should be refined together as both of them affect peak intensities. Refining all the thermal factors at the same time, in most situations, is also unrealistic. A process of thermal factor refinement from heavy elements to light elements should be taken[59]. Peak profile factors should be refined at last until all the peak positions and their relative intensities are in reasonable good fit.

In nature, Rietveld refinement in GSAS is a least-square method based regression process in multi-dimensional parameter space. Given a trial crystal structure model, a simulated diffraction pattern can be generated in GSAS, its difference with the experimental data pattern is evaluated through some indices. Two common indices which are used to evaluated the goodness of fitting are the χ^2 factor and weighted profile R factor. Their definitions are as follows:

$$\chi^2 = \frac{1}{N} \sum w(I_{calc} - I_{obs})^2, \tag{3.10}$$

and:

$$R_{wp}^2 = \frac{\sum w(I_{calc} - I_{obs})^2}{\sum w(I_{obs})^2} \tag{3.11}$$

In reality, a Rietveld refinement can't be perfect. If the value of R_{wp} is around or smaller than 0.09 and the value of χ^2 is around or smaller than 2 within a Rietveld refinement, this refinement can be seen as a good fit[64]. However, indices of goodness of fitting alone don't necessarily guarantee the success of a Rietveld refinement. A refinement with all peak positions, peak intensities, and peak shapes reasonably refined is the final criteria of judging the goodness of fit.

A final problem of GSAS refinement arises from its refinement process. During each refinement round, small steps are taken for all refinement parameters as to see whether these small changes in parameters will resulting a smaller χ^2. A common glitch for all these regression methods is that the refinement path of parameters may stuck at a local minimum point not a global minimum point within the parameter space. In this situation, it requires the user to manually change some parameters in order to get out of this dilemma. So a reasonable trial crystal structure and good estimate of structural parameters are required for a user during a Rietveld refinement with GSAS.

3.3 Data Analysis

3.3.1 Pair Distribution Function (PDF) Analysis

Although X-ray diffraction along with Rietveld refinement could give information about the average structure information about a researched material. The local structure information is lost in diffuse scattering[65]. The diffuse scattering contains structural information about local distortion and vacancy disorder which is not periodically present in the lattice. Pair Distribution Function (PDF) analysis provides a technique that can be used to research the local structure model of a researched material. The pair distribution function gives a probability distribution of finding some certain atomic correlation pair as a function of real space distance. The peak position on x-axis on a PDF pattern represents the correlation length of a certain atomic pair, the intensity of y-axis on a PDF pattern is associated with the coordination number and scattering lengths of atomic species.

Fig. 3-9 shows several material examples whose crystal structures can not be determined by using conventional X-ray diffraction methods. In these materials, the local structure domains usually extend to several nanometers, and no long-range order could be found within their crystal structures. A common situation is a local distortion of several atomic species could happen within a original perfect periodic lattice. Atoms within a unit cell could deviate from their average atomic positions due to Charge Density Wave (CDW). Although conventional X-ray diffraction still gives sharp Bragg peaks which can be used to determine their average structure in this case, superlattice peaks rise due to the lost of periodicity caused by local distortion. A larger supercell contains 2×2×2 or 3×3×3 unit cells should be viewed as the elementary building blocks of the whole crystal lattice and thus a more complex crystalline group symmetry should be introduced. The intensity of superlattice peaks is usually very small, of several percentages of the average Bragg peaks. So resolving superlattice structures with only Rietveld refinements is not applicable. PDF measurements could give information of the correlation lengths and coordination numbers of a structure, this is very useful in analyzing a material with local distortion. Relative

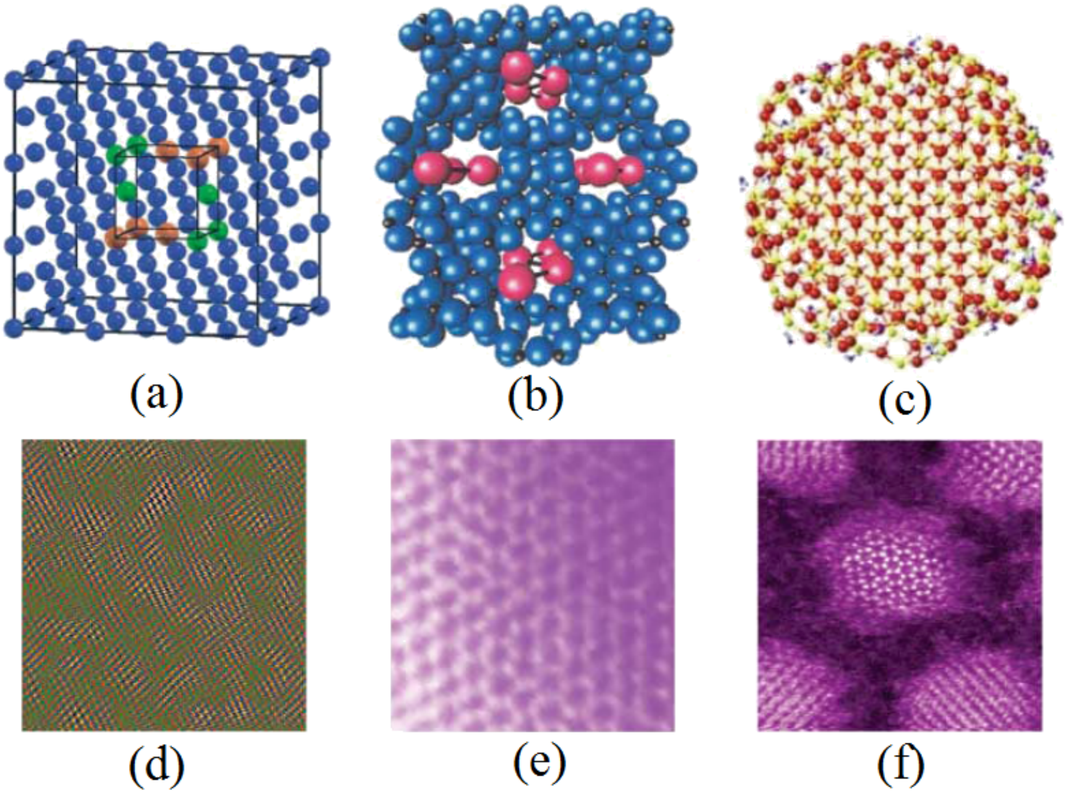

Figure 3-9: A figure showing the local structure of non-crystalline materials. (a) Nanostructured bulk material, (b) intercalated mesoporous material, (c) discrete nanoparticles. Their corresponding TEM images are shown below respectively. Modified from [66].

works can be seen in [67, 68, 69, 70].

Illustrated in Fig. 3-10 is a comparison of the conventional XRD patterns and corresponding PDF patterns of three samples. The top figures are from a crystalline bulk sample. As can be seen from the figure, both the XRD pattern and PDF pattern have sharp peaks which can be modeled with Gaussian peak profiles. The bottom two samples are from two amorphous samples, broad and diffusive peak features are shown on their XRD patterns which is called the Scherrer broadening[71]. Scherrer broadening can be perfectly dealt with by modeling if material's correlation length is long enough, but such modeling method failed when the correlation length is shortened to several nanometers[66]. So it is hard to extract useful structural information from XRD patterns of amorphous samples. PDF, on the other hand, is a good way to research the amorphous sample. As shown in fig. 3-10(d) and (f), both PDF pat-

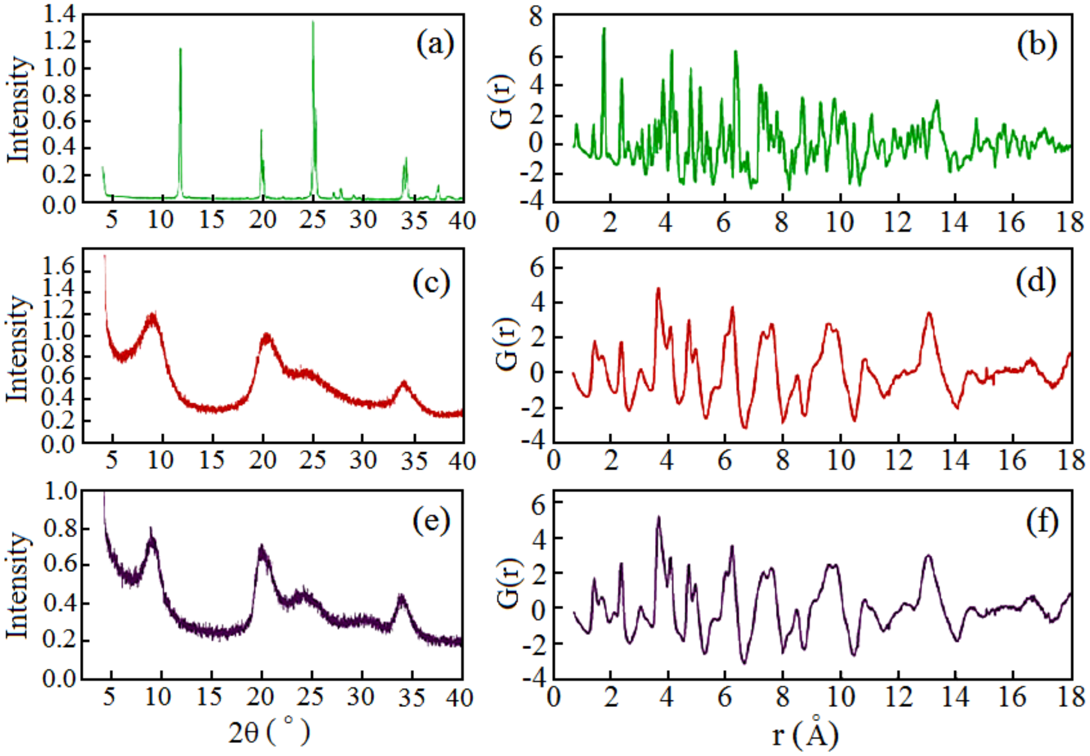

Figure 3-10: A comparison of conventional powder X-ray diffraction patterns and corresponding PDF patterns. Shown in figures on left columns are conventional XRD patterns for (a) a material in its crystalline phase, (b),(c) two materials in their amorphous phases. The diffraction patterns from the same samples are analyzed to get the total scattering patterns and extract PDF patterns which are shown in figures (b), (d), (f) respectively. There is considerably more information in the figures on the right column. Modified from [66].

terns show sharp peak features even though the samples are amorphous. The peak positions and intensities as discussed above are useful information to compute correlation lengths and coordination numbers of different atomic pairs. For amorphous materials, in most times, we are no longer taking care of the crystal structures at long distance since the amorphous sample lost its periodicity in x, y, z spatial directions and no long range order can be found. In another aspect, the local structure with short range order interests people a lot. By using PDF analysis method, we can get many useful results regarding local structures of an amorphous material.

Fig. 3-11 shows a schematic but straightforward procedure of generating PDF pattern from a known crystal structure. The atom sitting at origin is selected and a series of concentric blue circles are drawn around this atom so as to calculate

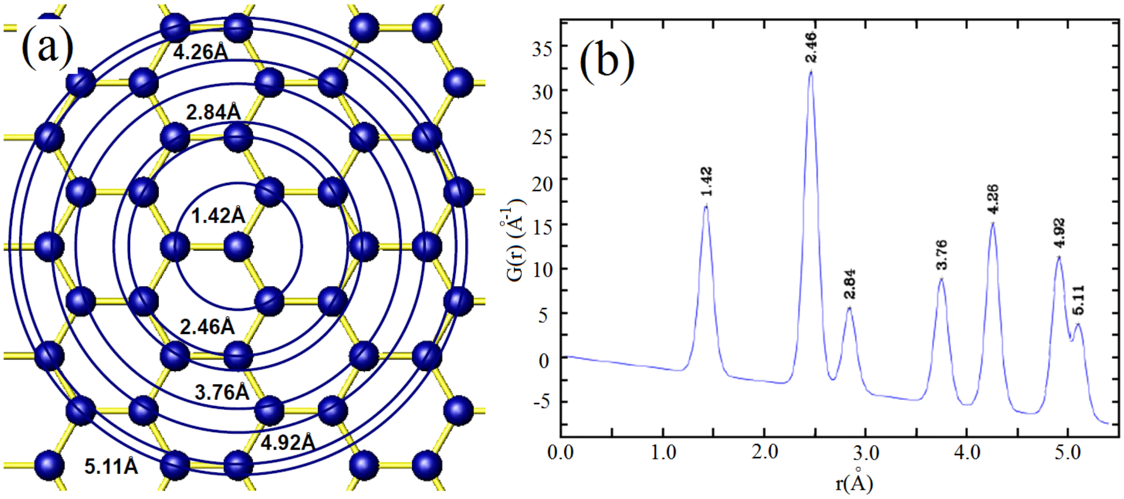

Figure 3-11: An illustration of the PDF modeling process. Figure (a) shows a typical 2-dimensional hexagonal lattice. One unique atom is placed at the origin (center of figure (a)) and blue concentric circles with larger and larger radii are drawn surrounding this atom. Whenever a new atom intersect with the blue circle, a unity of intensity in PDF is added in the histogram at position r (correlation length) which is the radius of the blue circle. The correlation lengths are labeled accordingly. Thermal motion of atoms will cause the histogram to broaden into Gaussian peaks. For this reason, a PDF is well represented by a collection of independent Gaussian peaks and can be analyzed and fitted with certain software package. The corresponding PDF pattern generated from crystal structure in figure (a) is shown in figure (b). Modified from [72].

the number of atoms which have the same distance from the central atom. Every atom siting on the blue circle with radius r will contribute a unit intensity with same correlation length r. This reflects on the PDF pattern is a sharp peak with its peak position located on x-axis with length r. Due to the thermal broadening, the delta function shaped intensity peaks will broaden into Gaussian functions which can be modeled with software package. The real material will be more complicated than this toy model. First, a real material is three-dimensional, so we need to draw concentric spheres in order to calculate the coordination numbers. Second, different atomic species have different scattering lengths, so their contribution to the peak intensity/area under peak shape is different. Both of these effects need to be taken into consideration in order to generating PDF patterns[73].

The inverse problem which is determining crystal structure according to a PDF pattern is however quite different and complex[74]. Nowadays, with the advent of computers and their wide applications in scientific research. Several software packages have been developed in order to solve this problem. For example, PDFgui uses the traditional least square refinement method and can be used to refine small crystal models, up to several hundred atoms can be input into software package and their lattice parameters can be tuned in order to achieve best fit. For large unit cell materials, Reverse Monte Carlo method is the choice, it can input over 20,000 atoms and fit both X-ray and neutron diffraction patterns. Other software like TOPAS PDF, DISCUS, ab initio PDF can also be applied under certain context[72].

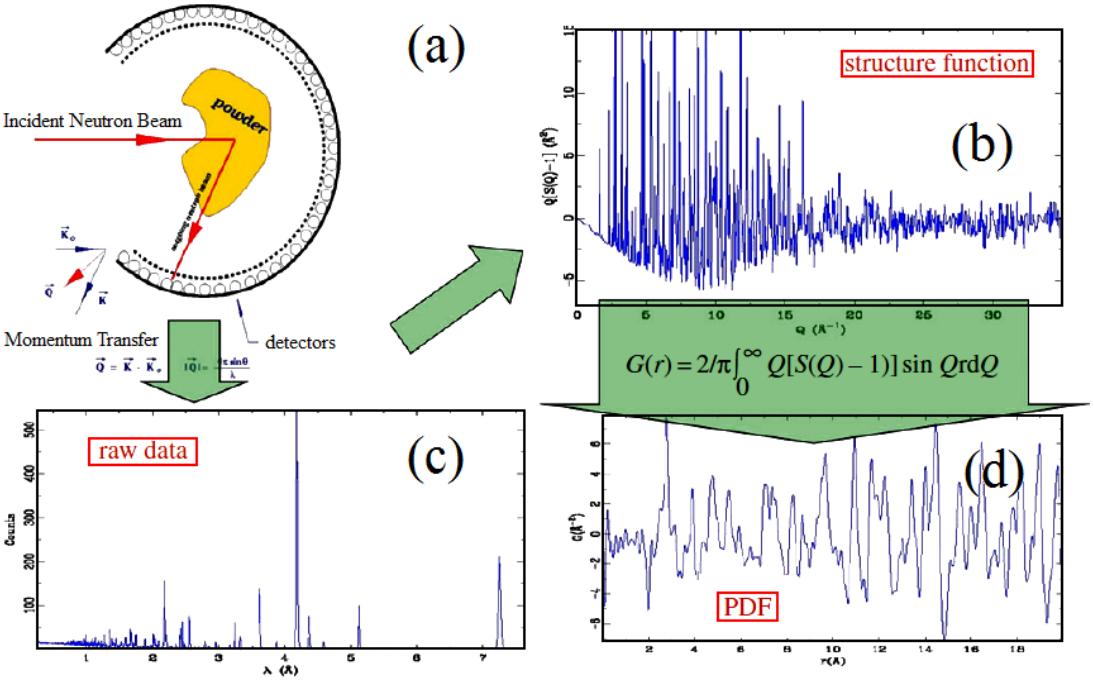

Figure 3-12: A schematic figure showing the procedures for collecting and processing PDF data. In figure (a), a powder nanopaticle sample is placed in the incident neutron beam, its scattered intensity is collected as a function of angle. Figure (b) shows the raw diffraction data after signal correction which get rid of the instrumental aberrations. After normalization, the reduced structure function is obtained, which is shown in figure (c). The PDF $G(r)$ function is obtained using a Fourier transform from the structure function $F(Q)$ which is shown in figure (d). Modified from [72].

Fig. 3-12 shows the process from sample measurement, data collection, to data analysis of a PDF pattern. In neutron diffraction experiment, the structure function $S(Q)$ is measured. PDF data can be obtained by Fourier transforming the structure function $S(Q)$. However, the raw $S(Q)$ needs to be corrected and normalized before it's transformed into final PDF data. These steps can be completed with the help of PDFgetN. PDFgetN is a software package which can be used to process raw $S(Q)$ data[75]. Corrections from instrument background scattering, sample can scattering, and normalization with respect to incident neutron beam need to be taken into consideration. Before sample measurement, empty instrument background scan, empty sample can scan, and vanadium rod scan were performed to provide data for further correction and normalization. The reason for using vanadium can here is vanadium atoms are nearly perfect incoherent scatterers, this makes it an easy step to subtract their contribution in $S(Q)$. The correction and normalization can be expressed in the following equation:

$$I = \frac{(S - B) - \alpha(C - B)}{V - B}, \tag{3.12}$$

Here in equation 3.12, S represents the scattering pattern from sample, B represents the scattering pattern from instrument background, C represents the scattering pattern from the empty sample can, V represents the scattering pattern from a vanadium rod, α represents the absorption coefficient of the sample container. In order to optimize data resolution, multiple detector banks with different angle coverage are used to collect diffraction data during sample measurement. Next, the parameters of the experiment set need to be input into PDFgetN such as height and radius of the sample, sample's chemical composition. This will allow the software to do multiple scattering correction and normalization. For samples with high inelastic scattering, Placezek correction should be applied[76]. But this option is not recommended for all sample corrections because it might over-correct the low energy portion as this method assumes a high energy of neutron and its ballistic scattering by an atom[77]. A typical situation for using Placezek correction is for materials which contain hydrogen atoms.

After correction, diffraction data from different banks will be combined to produce new $S(Q)$. The formula for Fourier transforming $S(Q)$ in order to get $G(r)$ is as follows[65]:

$$G(r)_{exp} = \frac{2}{\pi} \int_{Q_{min}}^{Q_{max}} Q[S(Q) - 1] sin(Qr) dQ \tag{3.13}$$

This formula shows how we can extract PDF pattern from experiment measured quantity: $S(Q)$. Here,

$$Q = \frac{4\pi sin(\theta)}{\lambda} \tag{3.14}$$

λ is the neutron wavelength and 2θ is the scattering angle. In reality, Q_{min} and Q_{max} can be determined by experimental conditions. Q_{max} is often evaluated under the experimental maximum to eliminate noise signal. In neutron diffraction experiment, the signal to noise ratio is usually unfavorable in high-Q region[66].

In theory, a PDF model can also be calculated directly from crystal structure model[72]:

$$G(r)_{mod} = \sum_i \sum_j \frac{b_i b_j}{\langle b \rangle^2} \delta(r - r_{ij}) - 4\pi\rho_0 r \tag{3.15}$$

In this formula, i and j represent the indices of atoms within a lattice, b_i is the scattering length for atom with index i. $\rho(0)$ is the average density of sample. The first part of this formula sums over all atomic pairs with delta functions to give a peak intensity profile generated from different atomic pairs. Only an atomic pair with distance r_{ij} equal to r could make a contribute in peak intensity at peak position r. In reality, due to the thermal vibration of atoms, the delta function shall broaden into Gaussian functions. And the peak intensity contributed from an atomic pair is also in proportional to the product of its composed two atoms' scattering lengths. The second part of this formula shows a baseline function of $G(r)$ which is $-4\pi\rho_0 r$.

$\rho(r)$ is another important quantity in PDF analysis which is called the atomic pair density. Its relationship with $G(r)$ can be expressed as follows:

$$G(r) = 4\pi r[\rho(r) - \rho(0)] \tag{3.16}$$

or:

$$\rho(r) = \frac{1}{4\pi r} G(r) + \rho(0) \tag{3.17}$$

Like $G(r)$ function, $\rho(r)$ also can be directly calculated from crystal structure. Its formula can be written as:

$$\rho(r)_{mod} = \frac{1}{4\pi r^2 N} \sum_i \sum_j \frac{b_i b_j}{\langle b \rangle^2} \delta(r - r_{ij}) \tag{3.18}$$

Here, N is the total number of atoms. As a function of atomic distance r, $\rho(r)$ should starts from zero and essentially goes to the atomic number density when r reaches infinity. Using equation 3.17 and plug in $G(r)$'s baseline function: $-4\pi\rho_0 r$, $\rho(r)$'s baseline or background is a constant zero. $\rho(r)$'s meaning is the weighted density of neighbouring atoms at a distance r from an atom at the origin and the sums in $\rho(r)$ run over all atoms in the sample[66]. Although there will be some negative values for a $\rho(r)$ function in reality at low r range due to large oscillation, $\rho(r)$ should keep its positive value according to its physical meaning.

3.4 Sample Synthesis

3.4.1 Sample Synthesis of $Ge_2Sb_2Se_{5x}Te_{5-5x}$

In this work, in order to fully study GSST-225 materials, two series of GSST-225 samples with different Se doping have been synthesized with doping content x ranging from 0.0 to 1.0, x step equals to 0.1. Two different cooling methods have been applied during our sample growth: (1) slow cooling/furnace cooling (SC/FC), which has relative slow cooling rate; (2) liquid nitrogen quench (Q), which has relative fast cooling rate. In our work, bulk polycrystal GSST-225 samples were prepared with solid reaction method. Part of the samples were ground for further XRD and EDS measurements to characterize the samples' phase compositions and chemical stoichiometries. Samples in bulk form were used for resistivity measurements. We also tried optical floating zone method, chemical vapor transport method to grow GST-225 material in single crystal form, but no idea samples were produced. Due to the complexity of different possible phase formations and stacking orders within this material, for now, the only ways to grow GST-225 in single crystal form is using magnetron sputtering method or atomic layer deposition method, both methods will produce GST-225 in thin-film form[29].

SC-GSST and Q-GSST materials were synthesized using following solid state reaction methods. First, powders of Ge (99.999%), Sb (99.5%), Se(99.999%) and Te (99.999%) were weighed in stoichiometric quantities. Then, the powders were mixed and ground with a mortar and pestle for 30 minutes. The well mixed powder was then pressed into a pellet. If the powder pellet was heated directly in air, oxygen would react with component elements and no target phase will be produced. So, we sealed pellets in evacuated quartz ampules and heated ampules up to 750 °C. SC-GSST samples were obtained by slow cooling to room temperature. Q-GSST samples were obtained by dipping quartz ampules into liquid nitrogen for fast cooling process. Energy dispersive X-ray (EDX) analysis was performed to confirm samples' chemical stoichiometries. Part of the EDS results are shown in Table 3.3. X-ray diffraction (XRD) experiments along with Rietveld refinements were performed to confirm sample's phase compositions.

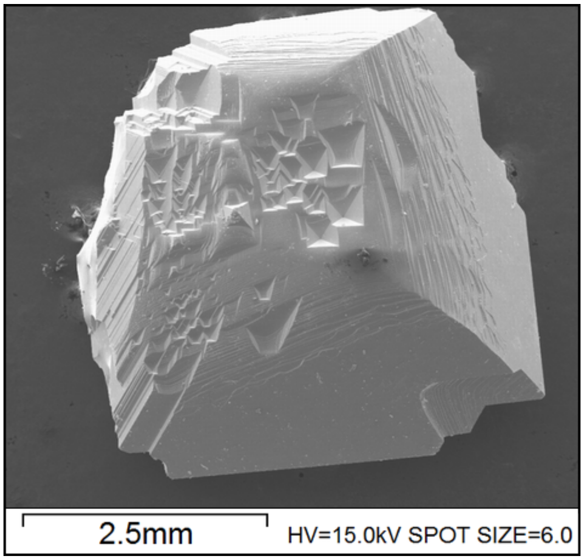

Figure 3-13: Scanning electron microscope (SEM) picture of a typical GST-225 sample piece.

	Doping x	Ge(%)	Sb(%)	Se(%)	Te(%)
1	$x = 0.4$	20.5(3)	22.1(2)	24.7(4)	32.7(1)
2	$x = 0.6$	21.2(1)	19.5(3)	35.8(3)	23.5(4)
3	$x = 0.8$	20.3(4)	23.1(6)	45.7(1)	10.9(2)
4	$x = 1.0$	19.9(3)	21.4(2)	59.7(3)	0.0

Table 3.3: EDS measurement results of GSST-225 samples. Atomic fractions of Ge, Sb, Se, and Te are shown in this table.

Apart from the majority phase of GSST-225 (of space group $P\overline{3}m1$), a secondary phase of GSST-124 (of space group $R\overline{3}m$) usually coexists within the sample. The rough ratio of GSST-225 phase to GSST-124 phase is around 6:1. In order to get Sb atoms fully entering into the lattice and make sample more homogeneous, we usually repeat the following sintering process in order to get high quality samples. For SC-GSSTs ($0.0 \leq x \leq 1.0$) and Q-GSSTs ($0.0 \leq x \leq 0.8$), samples show crystalline phases. light grey color were observed on samples' surfaces. When they were cleaved, shiny flat surfaces exposed. For Q-GSSTs($0.9 \leq x \leq 1.0$), samples show amorphous phases. They show dark grey color and are quite fragile. Sample surface is curved and show glass-like gloss.

3.4.2 Floating-Zone Method

Another method we have tried for growing GSST-225 is the floating zone method. The floating zone method can be used to grow single crystal material and many other materials like metals, oxides, semiconductors. This method is crucible free since it uses strong concentrating light to heat the sample[56].

Fig. 3-14 shows a schematic plot of the apparatus which used for floating zone method. Nowadays, people use halogen or Xenon lamps and ellipsoid mirrors to concentrate light beams. Two ceramic rods are mounted between upper and lower shafts. In order to achieve high homogeneity of grown crystal, the two rods usually rotate with the shafts so as to dissipate the heat uniformly around the cylinder-shaped floating zone. According to different material the rotation speed can vary from 0-50 rpm[56]. The upper rod is usually called the feed rod and the lower rod is usually called the seed rod. They are mounted on shafts so as to make their tips meet at the focal point of ellipsoidal mirrors. At the start of floating zone crystal growth, the light from halogen lamp is concentrated on the tips of these two rods. When the tips are melt, a liquid area which called floating zone is created between top rod (feed rod) and bottom rod (seed rod)[78]. This melt floating zone is usually kept between two rods due to its surface tension and electromagnetic force (levitation). After the floating zone is created, the shafts along with two rods begin to move downwards at a pre-programmed rate/speed, the melt liquid in the floating zone begins cooling down and condensates on the seed rod. The seed rod function as a platform for crystal nuclei from the feed rod to spontaneously form target crystal[79]. As the stage moves down, more and more materials from feed rod are transferred into target materials which deposit on seed rod so as to make crystal or alloys of high purity and homogeneity. See Fig. 3-15. A complete crystal growth procedure for floating zone method usually takes several hours or even longer time.

One advantage of choosing floating zone method as crystal growth method is that it is a containerless method. So all the contamination from containers can be excluded. Usually, grown crystal will have crystal defects due to its contact with the

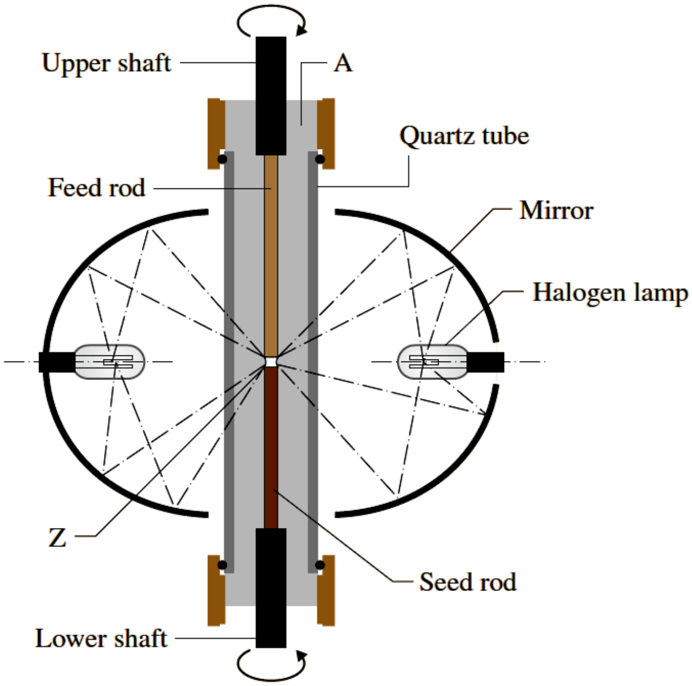

Figure 3-14: A schematic figure showing the working parts of optical floating zone apparatus. Modified from [56].

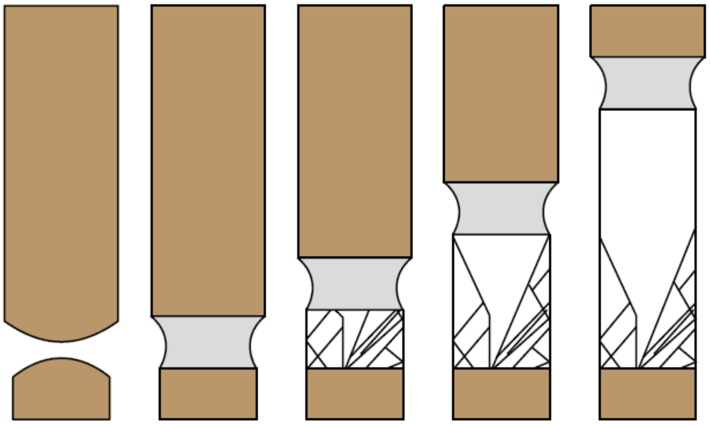

Figure 3-15: A schematic figure showing the different stages for nucleation on ceramic rods. Modified from [56].

wall of containers such as crucibles or glass tubes. So floating zone method can also prevent the crystal from developing surface defects such as cracks. Another advantage of floating zone method is that it allows the growth of large sized crystals. Both congruently and incongruently melting materials can be grown using this method[56].

The disadvantage of floating zone method is that it can's be used to grow materials with low surface-tension, high vapor pressure, high viscosity, or possess a phase transition during cooling due to the working principle of this method[56].

3.4.3 Chemical Vapor Transport Method

Another crystal growth method we have used to grow single crystal sample is chemical vapor transport method. Although for GST-225, we still can't grow single crystal out of this method, for Cu_xTiSe_2, it works well. Chemical vapor transport was first invented and utilized in single crystal material growth back to 1920s[80]. A lot of materials including oxides, halides, sulfides, selenides, tellurides, pnictides, and intermetallics can be grown using this method to produce their single crystals[80].

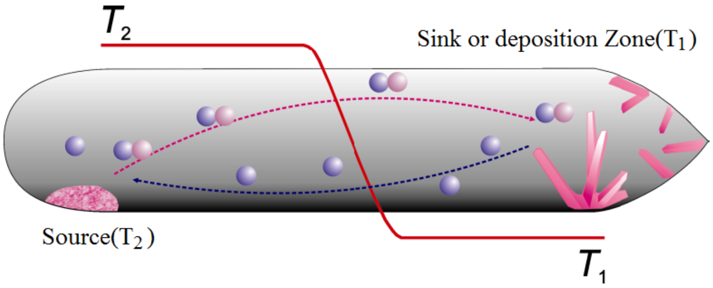

Figure 3-16: A schematic figure showing the experimental set for chemical vapor transport. Modified from [56].

Shown in Fig. 3-16 is a typical experimental set for conducting chemical vapor transport. The whole thing is sealed in a glass ampule to get rid of the contamination of oxygen. The source material is placed on the left side of the ampule, usually consisting the powder mixture with chemical stoichiometry of target material[81]. Some transport agent such like halogens and halogen compounds are mixed with source material to make it volatile. A two zone furnace is usually required for chemical vapor transport process to happen. At source end, a high temperature T_2 is applied. For a condensed phase, it will become volatilised if a gaseous reactant (transport agent) is present[82]. With more and more source material transferring into gas due to the heat of T_2, the hot gas mixing source material and transport agent will reach the low temperature end T_1 because of diffusion (shown in red dashed curved line in Fig. 3-16), here the source material deposits on ampule walls and crystal nucleation happens. At T_1, the transport agent is still in gas form, as this makes sure it won't deposit at the same site with the source material so as to contaminate the deposited crystal. A convection (shown in blue dashed curved line in Fig. 3-16) happens for the transport agent as to go back to the high temperature end to transport more source material to the low temperature end. A successful chemical vapor transport experiment depends on the establishment of the diffusion and convection cycle within the ampule[83]. Many parameters of experiment set can be tuned such like the length and diameter of the ampule, the amount of source material put on high temperature end, the chemical ratio of source material to transport agent, and the high temperature T_2 and low temperature T_1 in order to get optimized experiment results. For example, although enlarge the temperature difference between T_1 and T_2 helps establish higher temperature gradient across the ampule, this will accelerate the convection and diffusion process and increase the transport rate, the result crystal is usually inhomogeneous and defective[84]. Therefore, how to determine these experimental parameters and get optimized results is important for chemical vapor transport. In theory, it depends on free energy of the reaction between the chemical species, but in reality, the determination of optimized experimental parameters for chemical vapor transport is usually depend on experiences from similar systems, "trial-and-error", or thermodynamic calculations[85].

Shown in Fig. 3-17 is a picture of the Cu_xTiSe_2 single crystal sample we have grown by using chemical vapor transport method. The method is as follows. First, the chemical powders of high-purity Cu(99.999%), Ti(99.999%) and Se(99.99%) in stoichiometric amounts are well mixed and pressed into pellets. The powder mixture pellet was sealed in a quartz tube with length of 30cm and diameter of 1.5cm. In order to exclude oxidation, the quartz tube was sealed in vaccum. Iodine was used as the transport agent. Then the sealed quartz tube was placed in a two-zone furnace, the high temperature was set at 650°C and the low tempearture was set at 600°C. The quartz tube was heated up to target temperature configuration in 3 hours and stayed

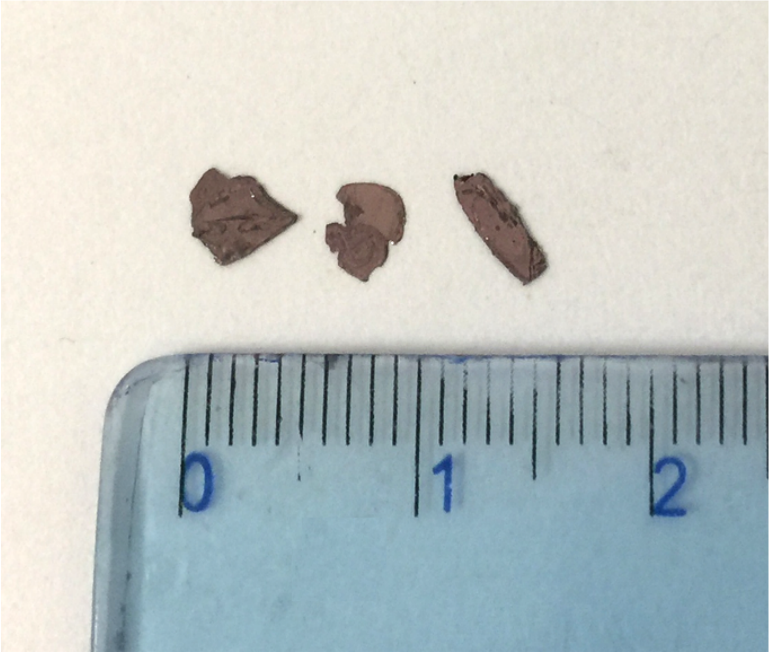

Figure 3-17: A picture showing Cu_xTiSe_2 single crystal sample grown using chemical vapor transport method.

at there for 1 day. A two stage cooling down process was applied in this experiment. First, the temperature was decreased to 450°C with cooling rate of 3°C/h. Then the furnace was shut down and the sample was slowly cooled to room temperature. XRD and EDS experiments were used to characterize the quality and phase compositions of samples.

Chapter 4

Crystal Structures and Electrical Properties of $Ge_2Sb_2Se_{5x}Te_{5-5x}$

In this chapter, the X-ray diffraction and resistivity measurement results of Se-doped GSST-225 ($Ge_2Sb_2Se_{5x}Te_{5-5x}$) will be discussed. We investigated the crystal structure and electric properties of this series compounds. Although as an promising phase change material, $Ge_2Sb_2Te_5$ has been synthesized and studied since 1987[2]. Most previous works have been focusing on synthesizing $Ge_2Sb_2Te_5$ in its thin film form using sputtering method and atomic layer deposition methods[8]. We have grown bulk $Ge_2Sb_2Se_{5x}Te_{5-5x}$ materials with slow cooling (SC) and liquid nitrogen quenching (Q) methods in our lab. Through systematic research of GSST-225, we have discovered a crystalline-to-amorphous phase transition at $x = 0.9$ in quenched GSST-225 samples. A metal-to-insulator transition is also discovered at this region. A temperature-dependent XRD experiment is conducted on Q-GSST $x = 0.9$ in order to research the phase transition process in depth and details. In order to research the thermal property of this material during its phase transition, DSC temperature scans and isothermal scans are performed and results are discussed in this chapter. And finally a schematic phase diagram of GSST-225 material is given.

4.1 Crystal Structure of $Ge_2Sb_2Se_{5x}Te_{5-5x}$

In an effort to understand the thermal stability and phase transition between the crystalline and amorphous phases of Se-doped GSST-225 samples, we have prepared Se-doped GSST-225 samples, from $0 \le x \le 1$ by both slow cooling (SC) and liquid nitrogen quenching (Q) from the melt. In order to research the crystal structure of these materials, systematic X-ray diffraction measurements were done on both SC-GSST and Q-GSST samples. The results are shown in Fig. 4-1. As we can see, in this figure, two types of XRD patterns showing different peak features are presented: (i) XRD patterns showing sharp peaks which indicate crystalline phases, these patterns are located on SC-GSST $0 \le x \le 1.0$ and Q-GSST $0 \le x \le 0.8$, (ii) XRD patterns show diffusive broad bumps, these patterns are located Q-GSST $0.8 \le x \le 1.0$. No crystalline-to-amorphous phase transition is observed in SC-GSST samples as a function of Se-doping, but this phase transition does happen in Q-GSST samples when the doping content x reaches around 0.9. Another effect which can be observed on XRD patterns is a constant peak shift to the left as doping x increases. Although the amount of shift movement is small, this is a good indicator showing the shrinking of the unit cell as more and more Se atoms coming into the lattice. According to the atomic radii in [86, 87], the ionic radius of Te^{-2} is 2.21Å, the ionic radius of Se^{-2} is 1.98Å. Te's ionic radius is larger than the Se's. With more Se atoms replacing the atomic sites of Te, it is expected that the unit cell will have smaller dimensions compared with the ones with low Se doping.

It is worth mentioning that the crystal structure of SC-GSST $x = 1.0$ sample has a different XRD pattern compared with the XRD patterns of other crystalline phases. A different crystalline structure is expected here. For now, we still don't have a clear and neat Rietveld refinement result showing the detailed and specific crystal structural phases of this sample. However, some previous works[88, 89] do shed some light on this mysterious phase. In work of Bartak et al.[88], a similar XRD pattern of $Ge_2Sb_2Se_5$ has been shown with some peak points from several possible formed phases, some calculated peak positions give a relatively good fit of the data pattern.

A rough conclusion can be reached here that the actual $Ge_2Sb_2Se_5$ phase is composed of several sub-binary phases like GeSe, $GeSe_2$, Sb_2Te_3, and etc.

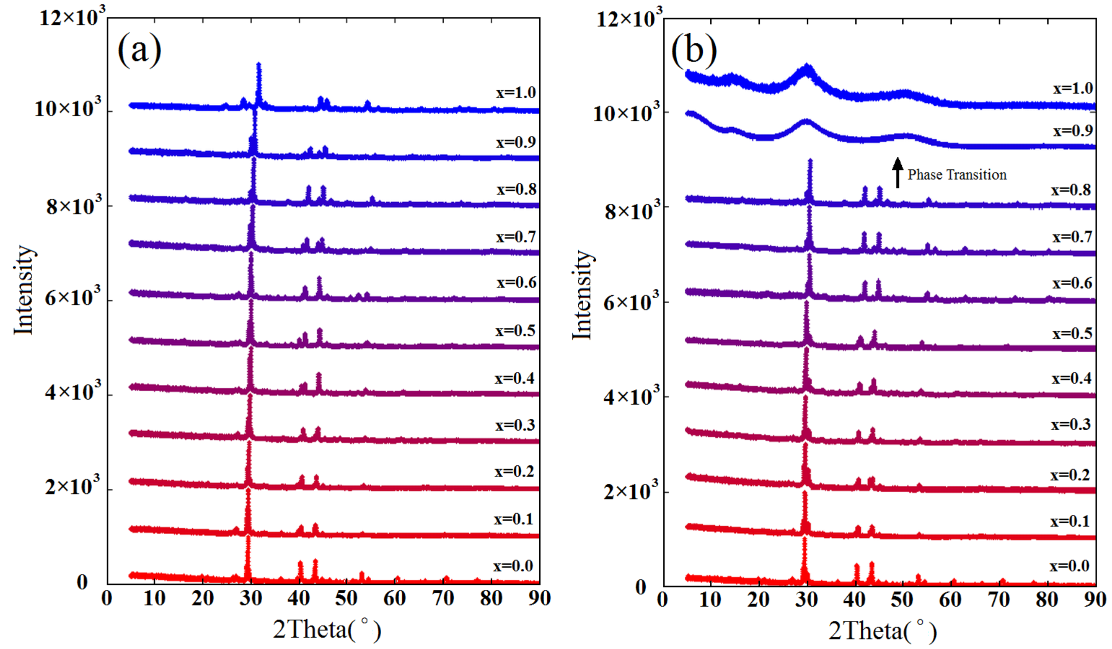

Figure 4-1: X-ray diffraction patterns of (a) SC GSST-225 samples and (b) Q GSST-225 samples across x doping spectrum ($0.0 \leq x \leq 1.0$, x step 0.1). From red color to blue color: low Se-doping end ($Ge_2Sb_2Te_5$) to high Se-doping end ($Ge_2Sb_2Se_5$). Black arrow markers where crystalline-to-amorphous phase transition happens.

The Rietveld refinements of X-ray diffraction patterns of SC GST-225 and Q GST-225 both at $x = 0.0$ and $x = 0.4$ are presented in figure 4-2. These Rietveld refinements were done with GSAS software package. Rietveld refinements show the following phase composition results. For SC GSST-225, there are two different phases presenting in the material. One majority phase of $Ge_2Sb_2Se_{5x}Te_{5-5x}$ ($P\overline{3}m1$, $\sim$86%) and a secondary $Ge_1Sb_2Se_{4x}Te_{4-4x}$ phase ($R\overline{3}m$, $\sim$14%). Compared with the SC-GSST, Q-GSST shows an additional cubic phase, the cubic GSST phase shows a rocksalt like unit cell, with its 4(a) sites fully occupied with Te/Se atoms, and 4(b) sites occupied with 40% of Ge, 40% of Sb and 20% of vacancies. The phase composition ratio of $Ge_2Sb_2Se_{5x}Te_{5-5x}$ to $Ge_1Sb_2Se_{4x}Te_{4-4x}$ is around 6:1, no matter in as-grown or quenched samples. $Ge_1Sb_2Se_{4x}Te_{4-4x}$ is much like a byproduct you will get during synthesizing $Ge_2Sb_2Se_{5x}Te_{5-5x}$ in bulk form. The cubic $Ge_2Sb_2Se_{5x}Te_{5-5x}$

phase only occurs within quenched GSST samples, its volume fraction is around 20% and doesn't show obvious relationship with doping content x.

$Ge_1Sb_2Te_4$ can be viewed as a superstructure of $Ge_2Sb_2Te_5$, its unit cell dimension is: $a = b = 4.02$Å, $c = 41.1$Å. Compared with $Ge_2Sb_2Te_5$ ($a = b = 4.02$Å, $c = 17.2$Å), their major difference comes from the length in c-axis. In $Ge_1Sb_2Te_4$, more stacking layers of GeTe and Sb_2Te_3 are included within a single unit cell so as to make the c lattice constant larger than $Ge_2Sb_2Te_5$. This is because a larger unit cell with more layers in c-axis must be included in $Ge_1Sb_2Te_4$ in order to complete the periodicity in c-axis direction.

The lattice constants a and c along with volume fractions of composition phases in both SC-GSSTs and Q-GSSTs are extracted from Rietveld refinements. These results are shown in Fig. 4-3. In Fig. 4-3, the blue and magenta curves represent the a and c lattice constants as functions of Se doping x in both subplots. With the increasing of x, both a and c lattice constants decrease in both SC-GSSTs and Q-GSSTs samples. This is expected since the introduction of Se atoms in replacement of Te atoms will cause the shrinking of unit cells. The volume fraction of GSST-124 phase (red curves in figure) show no obvious dependency with x in both plots. The value of volume fraction of GSST-124 phase is around 16%. The volume fraction ratio of GSST-225 phase to GSST-124 phase is around 6:1 in both SC-GSSTs and Q-GSSTs samples. GSST-225 cubic/rocksalt phase only appears in Q-GSSTs, its volume fraction is around 20% with some fluctuations which also shows no obvious dependency with x.

Fig. 4-4 shows the bond length plot and bond angle plot as functions of doping x. From the data, it is noticeable that the bond lengths decrease as doping x increase, which corresponds to the fact that lattice constants a and c drop in length as x increases. Another point which can make from the bond angle plot is that the bond angle doesn't show obvious change with x. With more and more Se atoms doped, the unit cell shrinks as the interatomic distance decreases, however, the relative atomic positions of each atom doesn't change obviously, so as to cause the bond angles doesn't change too much.

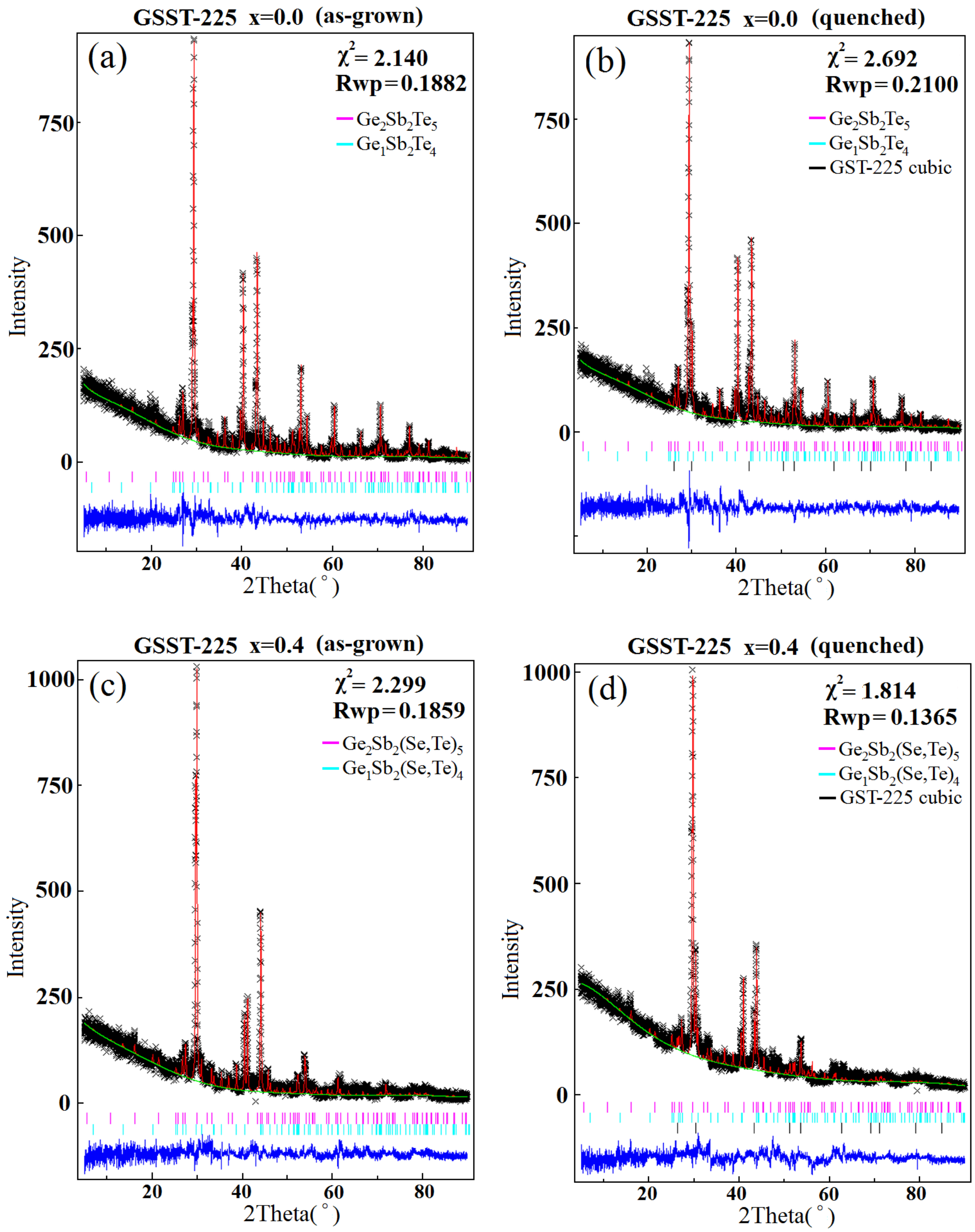

Figure 4-2: Rietveld refinement of (a) slow-cooled $Ge_2Sb_2Te_5$ ($x = 0.0$), (b) quenched $Ge_2Sb_2Te_5$ ($x = 0.0$), (c) slow-cooled $Ge_2Sb_2Se_2Te_3$ ($x = 0.4$) and (d) quenched $Ge_2Sb_2Se_2Te_3$ ($x = 0.4$). Black crosses shows XRD data, red curves show calculated XRD patterns, tick markers underneath show the peak positions generated by different phases, blue curves show differences between data and calculation. The corresponding indices of goodness of fitting: χ^2 and *Rwp* (*R*-factor of weighted profile) are listed on right-up corner in each subplot.

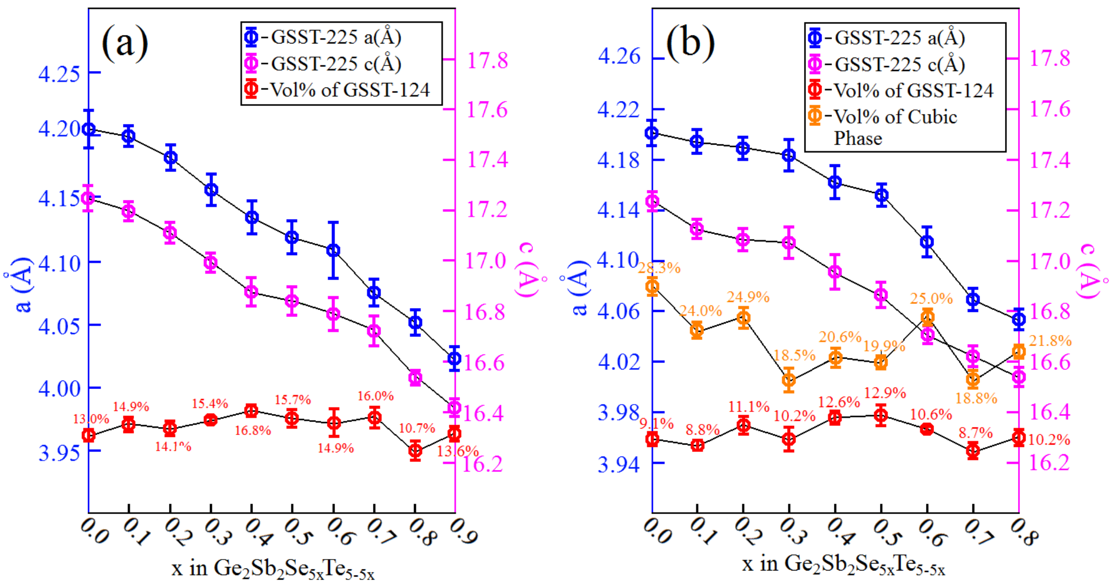

Figure 4-3: Figure (a) shows the *a* (blue) and *c* (magenta) lattice constants of GSST-225 hexgonal phase and volume fractions of GSST-124 hexagonal phase (red) as functions of doping content x in slow-cooled $Ge_2Sb_2Se_{5x}Te_{5-5x}$ samples. Figure (b) shows the *a* (blue) and *c* (magenta) lattice constants of GSST-225 hexagonal phase, volume fractions of GSST-124 hexagonal phase (red) and volume fraction of GSST-225 cubic phase (Orange) as functions of doping content x in quenched $Ge_2Sb_2Se_{5x}Te_{5-5x}$ samples.

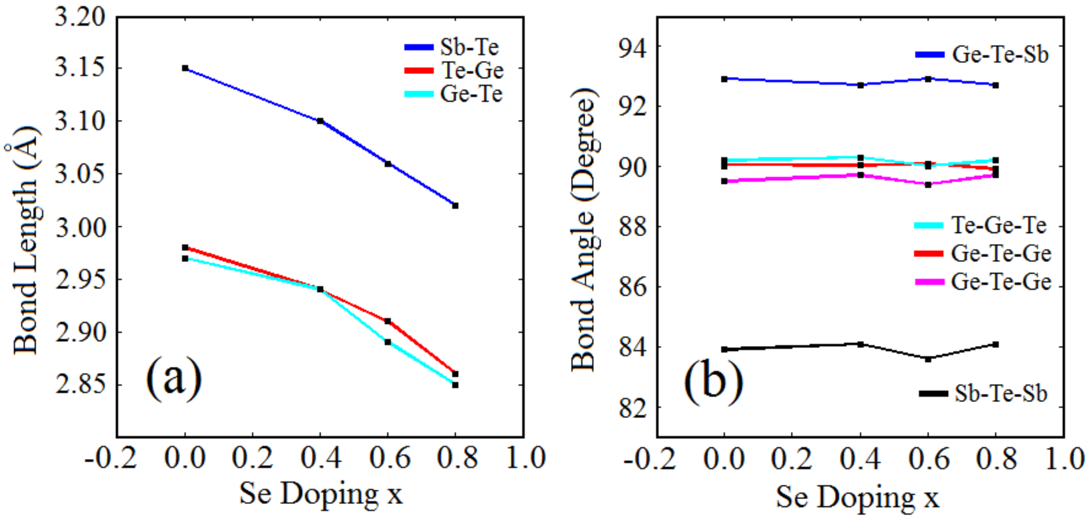

Figure 4-4: (a) Bond length plot of three selected atomic pairs within unit cell of GSST-225 phase as functions of doping x. (b) Bond angle plot of five selected atomic bond angles within unit cell of GSST-225 phase as function of doping x.

As discussed before, the metal-insulator behavior of phase change materials closely depends on the crystal structure of the researched material. According to previous works, $Ge_2Sb_2Te_5$ can exhibit three different phases, each phase's order of magnitude in resistivity is different. The hexagonal phase, which is crystalline, has the resistivity which is of order of $10^{-2} \sim 10^{-3}\ \Omega \cdot cm$; the intermediate cubic phase has the resistivity in order of $10^{-1} \sim 10^{-2}\ \Omega \cdot cm$; the amorphous phase has the resistivity in order of $10^{1} \sim 10^{2}\ \Omega \cdot cm$[8]. In phase change materials, material structures play an important role in determining electric resistivity and optic reflectivity[8]. Shown in Fig. 4-5 are the resistivity and reflectivty of GeTe (red curves) and $Ge_2Sb_2Te_5$ (blue curves). A continuous raising in temperature trigers the phase transition from amorphous phase to crystalline phase in GeTe and $Ge_2Sb_2Te_5$ materials. A step-wise resistivity curve can be seen from measurement. On the left of resistivity figure, the amorphous phase has the highest resistivity value in which the whole material is in a disordered state. Below that is the cubic/rocksalt structure which has intermediate resistivity values, in this structure, 20% of vacancies introduce a certain amount of disorderliness into the system. Further heating will render the material in its hexagonal crystalline phase, which has the lowest resistivity and also the lowest disorderliness. Although a clear and thorough research on the relationship between resistivity and disorderliness of this system is still missing, strong evidences are shown to indicate their connections. A simple explanation to illustrate this problem is with the introduction of crystal structure distortions and vacancies, scattering centers may arise from chemical disorder, the increasing number of scattering centers is the cause of increasing of the resistivity[90, 91, 92]. Some theoretical studies have suggested that vacancy disorder may be the reason why amorphous $Ge_2Sb_2Te_5$ shows insulating behavior[93, 94, 95, 96, 97].

Temperature-dependent resistivity data of both slow-cooled GSSTs and quenched GSSTs were systematically measured and the results are shown in Fig. 4-6. According to the data, the major results are summaried as follows: (i) for slow-cooled GSST ($0 \leq x \leq 0.8$), sample's resistivity decreases with temperature's decrease, resistivity's order of magnitude is of $10^{-6} \sim 10^{-5}\ \Omega \cdot m$, which is a typical metallic behavior;

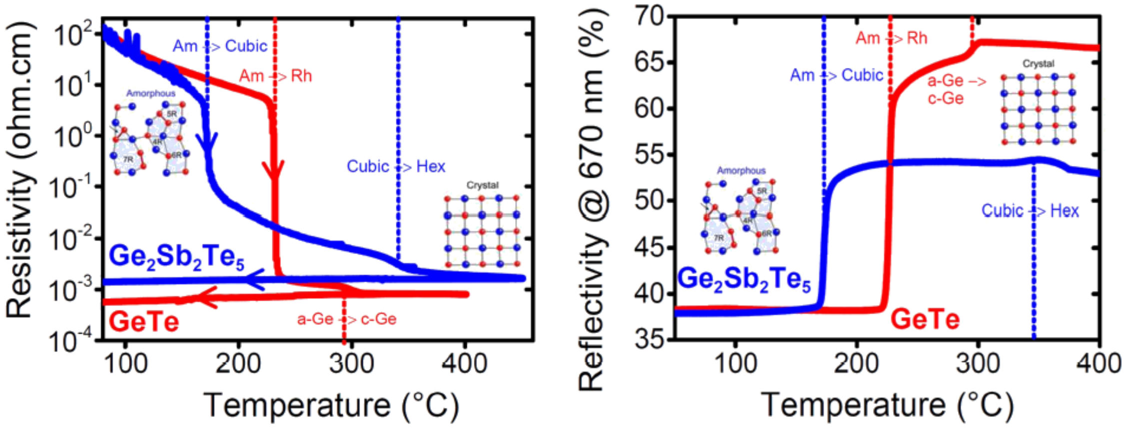

Figure 4-5: Resistivity (left) and reflectivity (right) measured as a function of increasing temperature (ramp rate of 10°C/min) for 100nm thick GeTe (exact composition is $Ge_{52.5}Te_{47.5}$) and $Ge_2Sb_2Te_5$ thin films deposited by DC magnetron sputtering. The resistivity measured during cooling down is also shown. The amorphous phase (initial state) is characterized by a high electrical resistivity and a low optical reflectivity and the crystalline phase by a much lower resistivity and higher reflectivity. Crystallization is accompanied by an abrupt change of resistivity and reflectivity. The crystallization temperature, electrical and optical contrasts are higher for GeTe than for $Ge_2Sb_2Te_5$.[8]

(ii) for furnace-cooled GSST ($0.9 \leq x \leq 1.0$), smaple's resistivity increases with temperature's decrease, resistivity's order of magnitude is of $10^1 \sim 10^3\ \Omega \cdot m$, which is a typical insulator behavior. (iii) A doping dependent metal-to-insulator transition is discovered in slow-cooled GSSTs around $x = 0.8$. (iv) for quenched GSST ($0 \leq x \leq 0.8$), sample's resistivity decreases with temperature's decrease, resistivity's order of magnitude is of $10^{-5} \sim 10^{-4}\ \Omega \cdot m$, which is a typical metallic behavior. (v) for quenched GSST ($0.9 \leq x \leq 1.0$), smaple's resistivity increases with temperature's decrease, resistivity's order of magnitude is of $10^1 \sim 10^5\ \Omega \cdot m$, which is a typical insulator behavior. (vi) A doping dependent metal-to-insulator transition is discovered in quenched GSSTs around $x = 0.8$. The resistivity's order of magnitudes is summaries in table 4.1.

Samples	0≤x≤0.8($\Omega \cdot m$)	x=0.9($\Omega \cdot m$)	x=1.0($\Omega \cdot m$)
Slow-cooled	$10^{-6} \sim 10^{-5}$	$10^{1} \sim 10^{2}$	$10^{1} \sim 10^{3}$
Quenched	$10^{-5} \sim 10^{-4}$	$10^{1} \sim 10^{3}$	$10^{2} \sim 10^{5}$

Table 4.1: Magitudes of resistivity measurements of slow-cooled and quenched GSST-225 samples.

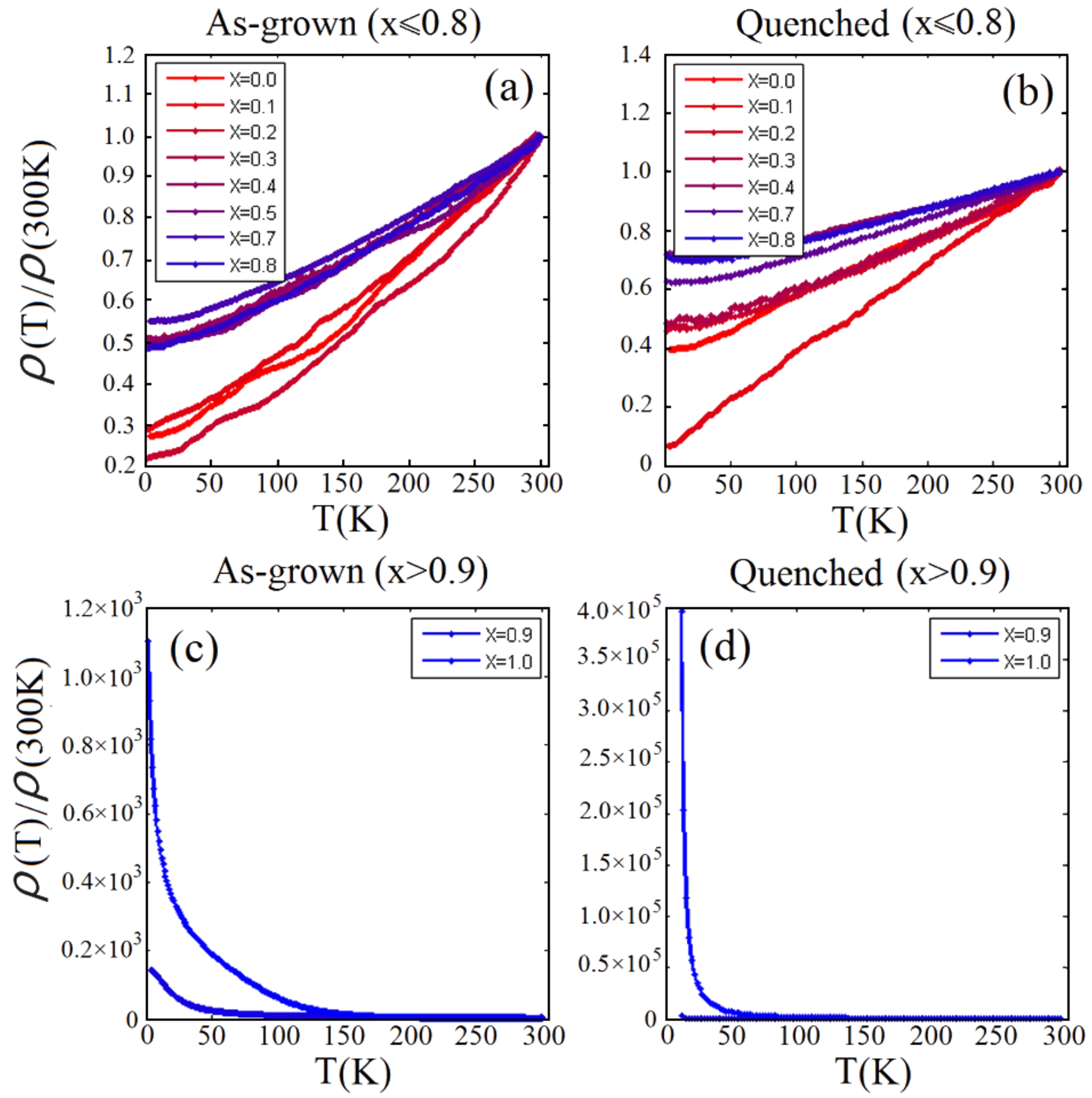

Figure 4-6: This figure shows the temperature-dependent resistivity measurements of (a) slow-cooled GSST-225 samples ($0 \leq x \leq 0.8$), (b) quenched GSST-225 samples ($0 \leq x \leq 0.8$), (c) as-grown samples ($0.9 \leq x \leq 1.0$), and (d) quenched samples ($0.9 \leq x \leq 1.0$) with x step as 0.1.

Although metal-to-insulator transitions are discovered both in slow-cooled GSST and quenched GSST samples around $x = 0.8$, the underlying mechanisms which trigger these transitions may not be the same. For quenched GSST $x = 0.9$ and $x = 1.0$ samples, they are in amorphous phases. Due to the lost of periodicity in space in amorphous phases, vacancies and disorders rise and function as scattering centers to electric current. For slow-cooled GSST $x = 0.9$ and $x = 1.0$ samples, they are in crystalline phases. Some previous published papers[93, 94, 95, 96] have pointed out Anderson localization may be the cause of this MIT, but a detailed research in GSST-225 is still absent.

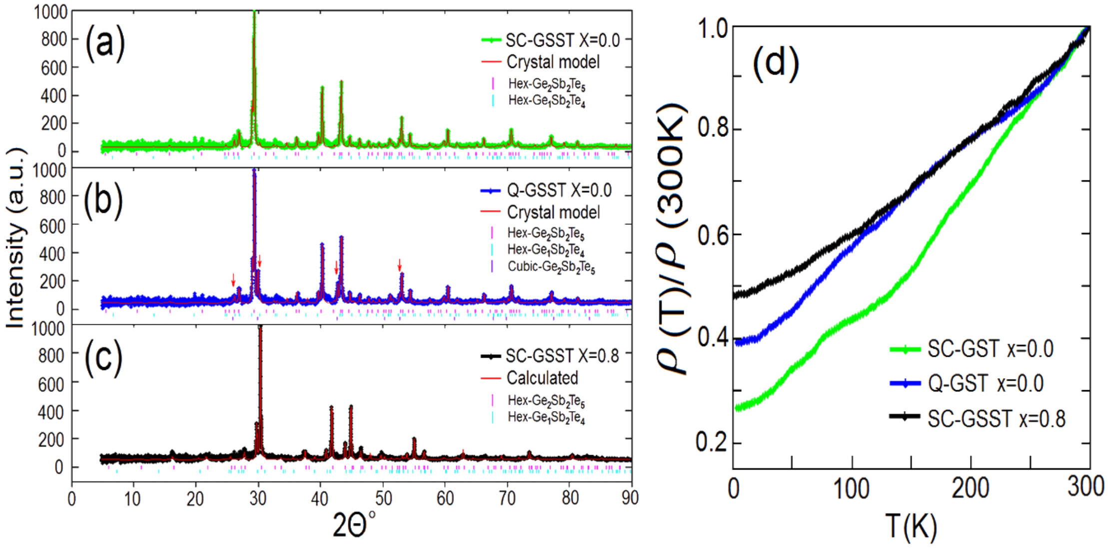

Figure 4-7: (a,b,c) The diffraction patterns of (a) SC-GST, (b) Q-GST, and (c) SC-GSST with $x = 0.8$. Data were collected at room temperature. All three samples are crystalline, as seen from the sharp Bragg peaks. For Q-GSST $x = 0$ (b), the quenching resulted in additional Bragg peaks due to the cubic phase (indicated with small red arrows). (d) The resistivity curves are normalized to their room temperature value for the three samples shown in (a-c). Modified from [98].

Shown in Fig. 4-8 are the powder X-ray diffraction patterns of (a) slow cooled GST-225 ($x = 0.0$), (b) quenched GST-225 ($x = 0.0$) and (c) slow cooled GSST-225 $x = 0.8$ samples. All data were measured and collected at room temperature. The corresponding sample synthesis information is provided in Chapter 4. Sharp Bragg peak profile in these three XRD patterns indicates that all these three samples are in crystalline phases. The phases discussed above in Section 6.3 were used to do Rietveld refinement in order to fit the data pattern. In all samples, the majority phase is GSST-225, a secondary phase GSST-124 is also present. Its chemical composition is $GeSb_2Se_{4x}Te_{4-4x}$. Detailed results of Rietveld refinements with GSAS are summarized in table 4.2. The a and c lattice constants decrease uniformly with Se-substitution as expected. The cubic phase is observed in quenched GST samples only as shown in 4-8(b). Although the majority phase is still hexagonal phase, additional Bragg peaks are present that arise from the cubic phase, such as the peak at 30.02°, this peak is

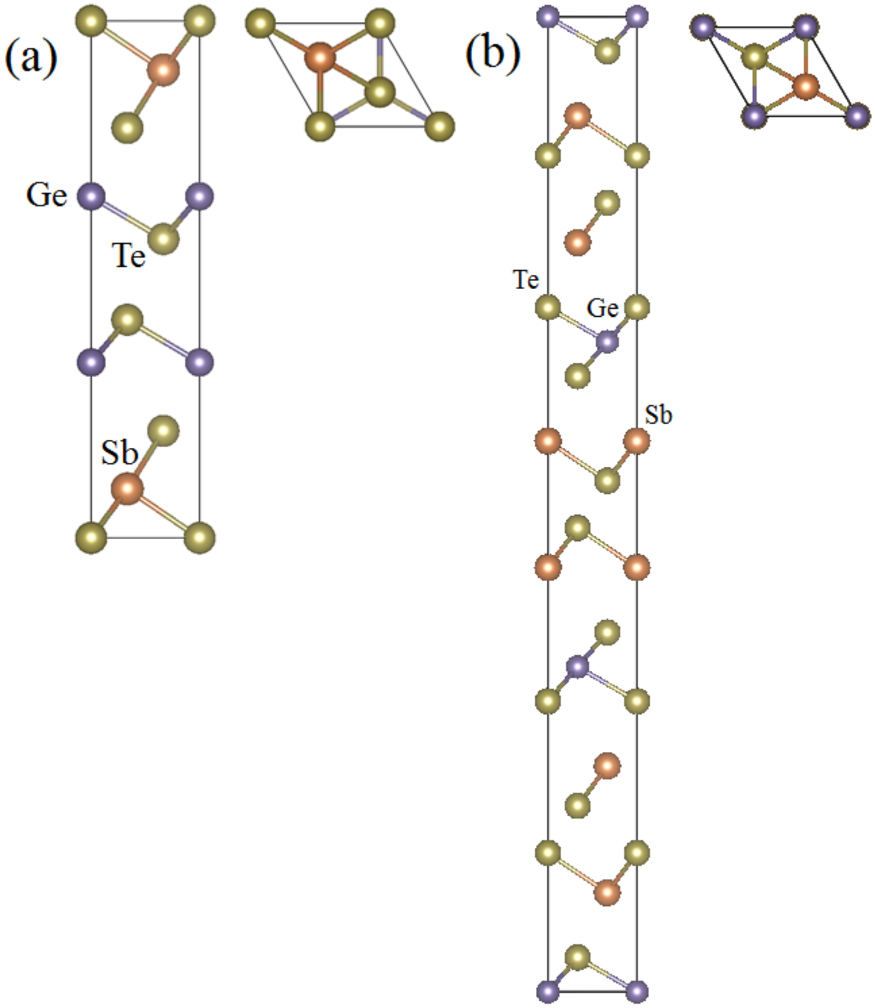

Figure 4-8: Figure (a) shows the unit cell stucture of GST-225 phase. Figure (b) shows the unit cell of GST-124 phase.

next to the hexagonal GST-225 peak which located at 29.42°. Rietveld refinement results of this cubic phase yielded a chemical ratio as follows: occupancy for Ge is 0.38(3); occupancy for Sb is 0.39(2); occupancy for Te is 1.02(2). This result is in agreement with the 0.4:0.4:1 ratio reported for the cubic phase in laser-crystallized $Ge_2Sb_{2+z}Te_5$ thin films [99].

According to this fact, for further refinement, we have fixed Ge, Sb and collective Se/Te ratios at 0.4:0.4:1.0; the refinement results for cubic phase is summarized in table 4.3. The cubic phase's volume fraction in quenched GSST samples is basically a constant (∼20%) with some fluctuations. No obvious increase or decrease trend of volume fraction of cubic phase with doping x is observed despite large changes in the kinetics of crystallization that result in amorphization for quenched GSST $x > 0.8$. This observed trend suggests that the transition from crystalline phase to the amorphous phase is not due to a growing cubic component as is assumed in thin films of GST material [98].

The resistivity of SC-GSST and Q-GSST changes with temperature as shown in Fig. 4-8(d). In order for a better comparison, the resistivity data of slow cooled GSST $x = 0.8$ is also included. All the three sets of data is normalized to their room temperature values (300K). According to the data, all samples show metallic behavior with the resistivity's value dropping as temperature decreasing. Slow cooled GST (green line) is metallic and shows no transition upon cooling. Quenched GST (blue line) is also metallic but show a residual resistivity which is higer than that in slow cooled GST (green line). This higher residual resistivity may be related to the increase in scattering centers due to the random Ge/Sb occupancy and vacancies of cubic phase presenting in quenched GSST samples while not in slow cooled GSST samples. As discussed above, theoretical studies also have indicated that the vacancy disorder may be the reason why amorphous GST shows insulating behavior [94, 95, 96, 97]. The resistivity in slow cooled GSST $x = 0.8$ (black line) still shows metallic behavior, however the residual resistivity value at low temperatures is even higher in comparison with other two samples. This may be related to randomness of the Se and Te atomic sites occupation. Further structural studies are discussed in chapter 6 to explore details of the atomic structures with doping. Above this Se concentration, the resistivity shows insulating behavior even for slow cooled GSST samples.

When high Se-doped GSST is quenched in liquid nitrogen, this leads to amorphization if the Se substitution exceeds $x = 0.8$. The crystalline phase is completely suppressed and an amorphous phase emerges even in bulk materials. Shown in Fig. 4-9(a) are the X-ray diffraction patterns for quenched GSST samples of $x = 0.8$, $x = 0.9$, and $x = 1.0$. Their corresponding temperature-dependent resistivity measurements data are shown in Fig. 4-9(b). Although the majority phase remains to be hexagonal GSST-225 up to $x = 0.8$, the structure is clearly transferred to amorphous

Phases	Space Group	a(Å)	c(Å)	Fraction
$Ge_2Sb_2Te_5$	P $\overline{3}$ m 1	4.204(3)	17.24(7)	87.03%
$Ge_1Sb_2Te_4$	R $\overline{3}$ m	4.227(1)	41.14(1)	12.97%

$Ge_2Sb_2Te_5$		x	y	z	U_{iso}(Å^2)
Ge	2d($\frac{2}{3}$,$\frac{1}{3}$,z)	2/3	1/3	0.100(7)	0.200(2)
Sb	2c(0,0,z)	0	0	0.329(4)	0.135(4)
Te1	1a(0,0,0)	0	0	0	0.123(9)
Te2	2d($\frac{1}{3}$,$\frac{2}{3}$,z)	1/3	2/3	0.200(1)	0.211(1)
Te3	2d($\frac{2}{3}$,$\frac{1}{3}$,z)	2/3	1/3	0.416(2)	0.110(8)

$Ge_1Sb_2Te_4$		x	y	z	U_{iso}(Å^2)
Ge	3a(0,0,0)	0	0	0	0.254(4)
Sb	6c(0,0,z)	0	0	0.434(3)	0.221(3)
Te1	6c(0,0,z)	0	0	0.143(1)	0.115(4)
Te2	6c(0,0,z)	0	0	0.300(8)	0.117(8)

Table 4.2: A list of the crystal structure parameters from the Rietveld refinement of the hexagonal phase of $Ge_2Sb_2Te_5$ and $Ge_1Sb_2Te_4$ in the slow-cooled sample. Modified from [98].

$Ge_2Sb_2Te_5$		x	y	z	U_{iso}(Å^2)	Fraction
Ge	4b($\frac{1}{2}$,$\frac{1}{2}$,$\frac{1}{2}$)	0.5	0.5	0.5	0.345(6)	40%
Sb	4b($\frac{1}{2}$,$\frac{1}{2}$,$\frac{1}{2}$)	0.5	0.5	0.5	0.172(2)	40%
Te	4a(0,0,0)	0	0	0	0.261(2)	100%

Table 4.3: A list of the crystal structure parameters from the Rietveld refinement of the cubic phase of GST-225 that appears only in quenched samples. Modified from [98].

for $x = 0.9$ and $x = 1.0$. As we can see the sharp Bragg peaks in these crystalline phases are replaced by broad humps, which is a typical sign of emergence of amorphous phase. An interesting point of these amorphous XRD patterns are that in GSST $x = 0.9$ and 1.0 samples, pre-peaks are observed between 10° and 20°. This is a strong indicative of the short range order existing in these amorphous materials, which is also typical in good glass formers [100, 101]. A related detailed discussion of local structure of quenched amorphous GSST samples are provided in Chapter 6.

Coupled with this crystalline-to-amorphous phase change is a metal-to-insulator transition, where a drastic change in the transport behavior is observed as seen in Fig. 4-9(b). The resistivity curves shown in Fig. 4-9(b) are colored corresponds to

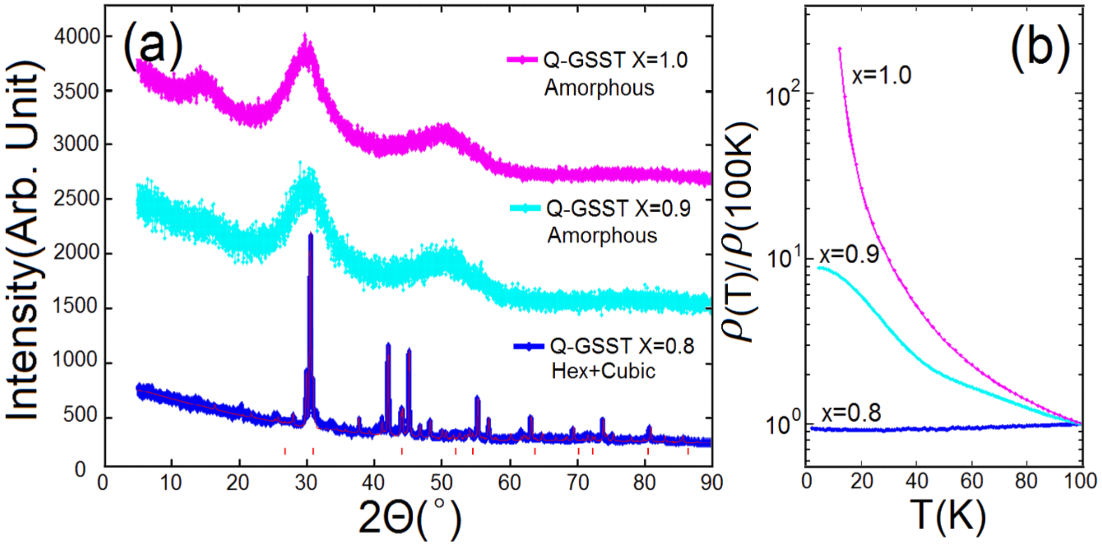

Figure 4-9: (a) The X-ray diffraction patterns of Q-GSST for $x = 0.8$, 0.9 and 1.0. The $x = 0.9$ and 1.0 are amorphous while the $x = 0.8$ is crystalline. The red tick marks under the Q-GSST $x = 0.8$ pattern are at the peak positions corresponding to the cubic GSST phase in $x = 0.8$. (b) The corresponding resistivity curves are normalized at 100 K. Modified from [98].

the XRD patterns shown in Fig. 4-9(a). All resistivity data are normalized to their values at 100K. It is clear that the metal-to-insulator transition is associated with a phase transition from the hexagonal to the amorphous and not from the cubic to the amorphous as is the case in thin films. This is because the volume fraction of the cubic phase does not change much with Se doping x, which suggests that the route to amorphization does not always proceed via the cubic phase[98]. It is likely that at the cooling rate of liquid nitrogen quench (of the order of ~100K/s), the hexagonal majority phase and cubic minority phase will always coexist. And their relative phase volume fraction ratio may very well vary with the cooling rate. Note that even though the XRD of quenched GSST $x = 0.8$ shown in Fig. 4-9(a) is crystalline, its resistivity value is higher than the one which is shown in slow-cooled GSST $x = 0.8$ in Fig. 4-8(d). The transition to the amorphous phase leads to several orders of magnitude change in the resistivity.

4.2 Phase Transition in Quenched GSST $x = 0.9$

In order to further research the crystallization kinetics of amorphous-to-crystalline phase transition in quenched high Se-doped GSST material, GSST $x = 0.9$ (liquid nitrogen quenched) materials were synthesized in our lab and used to perform temperature-dependent X-ray diffraction experiments. Part of the experimental results are shown in Fig. 4-10(a).

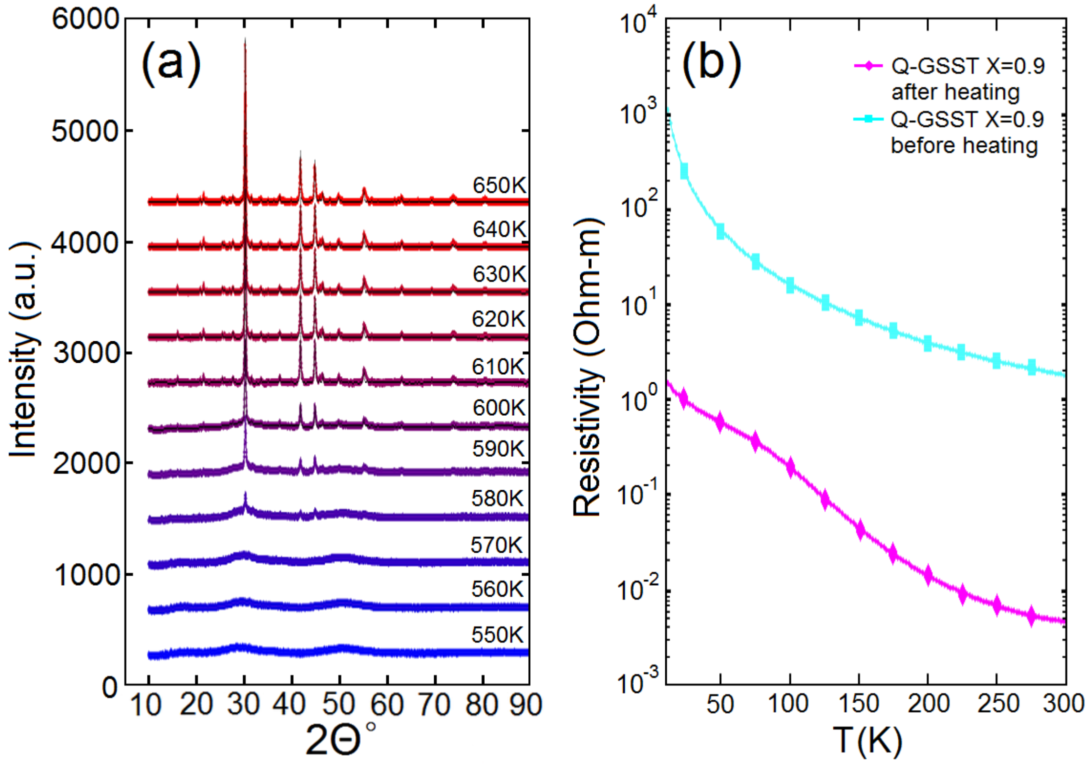

Figure 4-10: (a) Evolution of the diffraction patterns with background subtracted for $x = 0.9$ as a function of temperature on warming from 300 K. The crystallization begins on warming above ∼580 K. (b) A plot of the electrical resistivity of the $x = 0.9$ sample before and after heating on log scale. After heating, the resistivity drops by several orders of magnitude. Modified from [98].

In this experiment, a bulk piece GSST $x = 0.9$ material with flat surface is mounted on a heating plate which is connected to the thermal unit of RIGAKU XRD machine. In order to exclude the effect of oxidation of the sample when high temperature reaches, the whole stage is put in a chamber which was sealed in vacuum during the whole experiment. Some pre-measurements and adjustments of the orientation of the sample were done in order to get optimized XRD intensity. In this measurement, sample's temperature was first raised to 550K, when the temperature is fully equilibrated, a XRD scan was taken at this temperature which took around two hour. After this, a temperature rising procedure was taken in order to reach to the next target temperature: 560K, and another XRD scan would be taken at this temperature. The whole program would be kept running until the last XRD taken at 650K was finished. At this temperature, the whole material was already fully transferred into crystalline phase.

According to experimental results, which is shown in Fig. 4-10(a), recrystallization is observed on warming GSST $x = 0.9$ amorphous samples from room temperature. This is shown in Fig. 4-10(a) for quenched GSST $x = 0.9$ with the XRD diffraction patterns plotted as a function of increasing temperature. Each temperature's XRD measurement took around two hours for better data resolution. Around temperature of 580 K, small sharp Bragg peaks began to appear that belong to the hexagonal phase, although most of the sample was still amorphous, with broad peaks below the Bragg structural peaks. On further warming, the intensities of the Bragg peaks continue increasing and the volume fraction of the hexagonal phase increases as well. By temperature of 610 K, the transition to the crystalline phase was fully completed, as no further growth of the intensities of Bragg peaks was observed. One point worth mention is that no signature of the cubic phase was observed during warming, which is as expected, given that the cubic phase appears only during fast cooling process[98].

Shown in Fig. 4-10(b) is the electrical resistivity measurement data of the same GSST $x = 0.9$ sample before and after heating. Before heating, the resistivity of the amorphous GSST $x = 0.9$ sample is quite high and shows insulator behavior. After heating, the resistivity drops quite significantly but it is evident that after the phase change, GSST $x = 0.9$ is still insulating. In the absence of the cubic phase, recrystallized GSST $x = 0.9$ sample should be analogous to slow cooled GSST $x = 0.9$ sample. And indeed, this statement can be proven to be true with the data shown in Fig. 4-11.

In Fig. 4-11(a), the resistivity curves for slow cooled GSST x=0.9 (colored in green line) and GSST $x = 0.9$ recrystallized after the temperature dependent XRD measurements (colored in magenta line) are shown. As we can see, their resistivity behaviors are very similar. This confirms the point that after heating quenched GSST $x = 0.9$, its amorphous phase fully crystallizes into hexagonal GSST-225 and GSST-124 phases, which is analogous to the slow cooled GSST $x = 0.9$ sample. Quenched GSST $x = 0.9$ resistivity curve (colored in cyan line) is also plotted here for comparison. Fig. 4-11(b) shows the resistivity curve comparison for slow cooled GSST $x = 0.8$ and $x = 0.9$. This data shows that slow cooled GSST $x = 0.8$ is metallic and slow cooled GSST $x = 0.9$ is insulating. Thus a metal-to-insulator transition in slow cooled GSST samples occurs between $x = 0.8$ and $x = 0.9$[98].

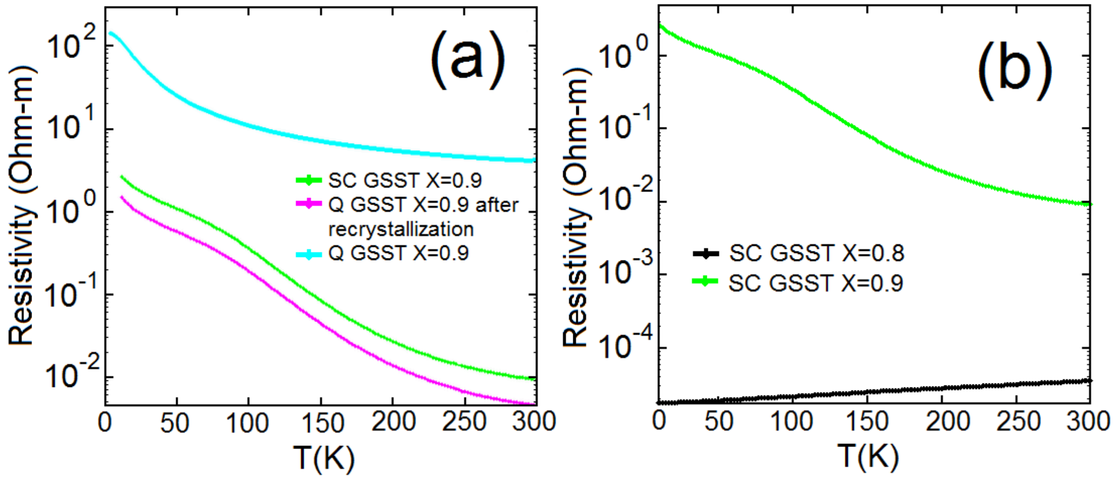

Figure 4-11: (a) The temperature dependent resistivity measurements for slow cooled GSST $x = 0.9$ (green), GSST $x = 0.9$ recrystallized after the temperature dependent X-ray measurement (see Fig. 4-10) (magenta) and quenched GSST $x = 0.9$ (cyan); In (b), temperature dependent resistivity measurements for slow cooled GSST $x = 0.8$ (black) and slow cooled GSST $x = 0.9$ (green). Modified from [98].

A more detailed temperature-dependent X-ray diffraction measurement with smaller temperature steps was carried out on quenched GSST $x = 0.9$ sample. The results are shown in Fig. 4-12. In this data, background is subtracted from the diffraction patterns so as to show the Bragg peaks from crystalline phase and broad humps from amorphous phase with better visual. As can be seen from this figure, from 510K to 579K, only diffusive bumps are observed on the patterns. This is because the sample is still in its amorphous phase. Above 580 K, small sharp peaks start to appear around $2\theta = 30°, 42°, 45°$. This marks the start of the phase transition, part of the amorphous phase started to transfer into crystalline phase. Above 610K, all amorphous phase bumps were gone and the intensities of crystalline phase peaks remain constant. This marks the end of phase transition[98].

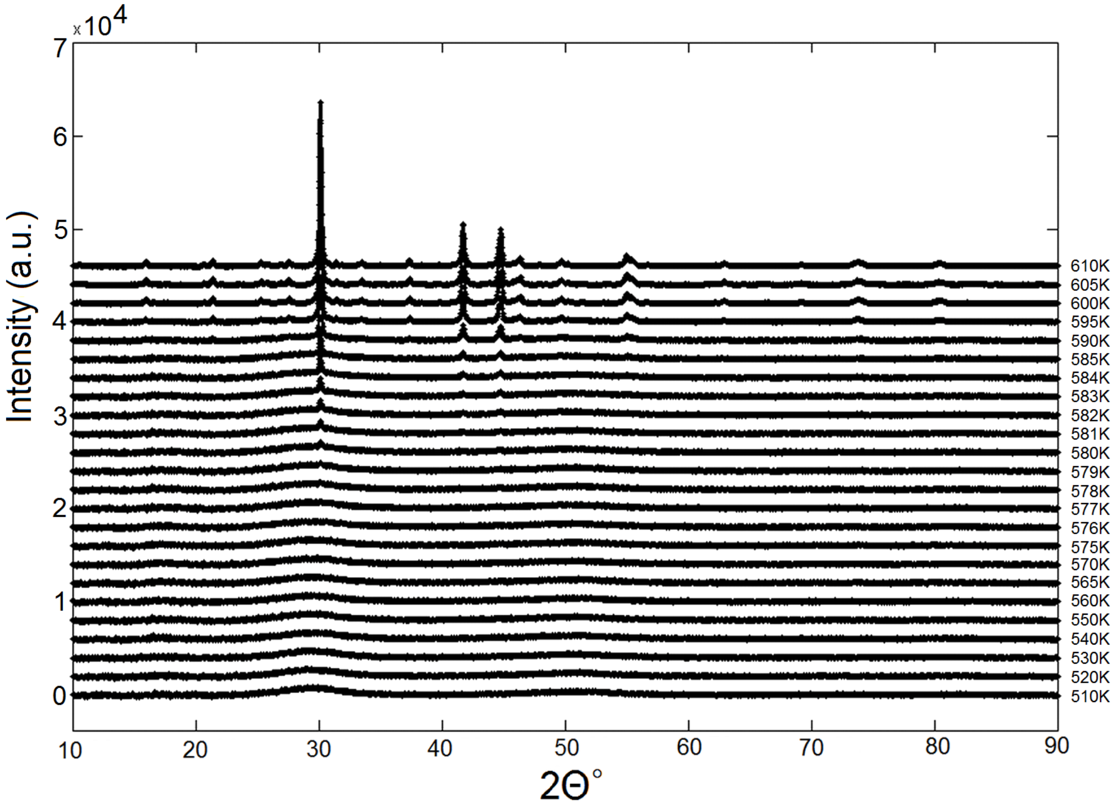

Figure 4-12: Temperature dependent X-ray diffraction measurements on Q-GSST $x = 0.9$ sample with finer temperature steps. Modified from [98].

In order to research the thermal stability of the amorphous phase up to 200°C. We have annealed Q-GSST $x = 0.9$ at 200°C for different time duration. Fig. 4-13 shows another XRD diffraction pattern data set collected on quenched GSST $x = 0.9$ sample. In this experiment, amorphous quenched GSST $x = 0.9$ sample was annealed at 200°C, below the crystallization temperature, for 15 hours, and then 100 hours. Experiments' results show that after a short annealing time (15 hours), there was no change on the XRD pattern. At longer annealing times (100 hours), small sharp peaks started to show up which indicates the formation of the crystalline phase with small volume fraction. A comparison of XRD patterns between the quenched GSST $x = 0.9$ sample annealed for 100 hrs (colored in red line) and the quenched GSST $x = 0.9$ sample which was fully crystallized (colored in blue line) shows clearly that the small peaks in the red pattern is from the crystalline phase. This indicates that although strong, this glass is not as strong as some other glasses like aluminum-rich Al-Ni-Fe-Gd alloys[100].

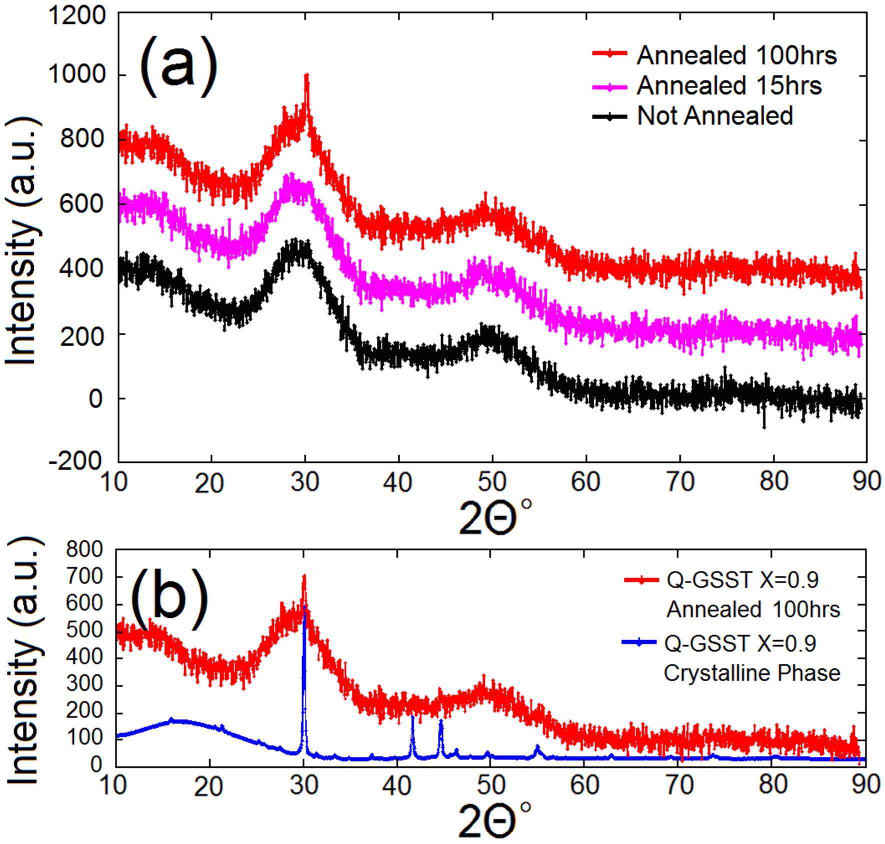

Figure 4-13: (a) A comparison of the XRD patterns measured for Q-GSST $x = 0.9$ sample (black) in the amorphous phase, the same sample annealed for 15 hrs (magenta), and annealed for 100 hrs (red). In (b), the diffraction pattern of the amorphous Q-GSST $x = 0.9$ sample annealed for 100 hrs (red) is compared to the diffraction pattern of re-crystallized $x = 0.9$ sample (blue) after the temperature dependent XRD measurement. Modified from [98].

As a conclusion part, we have summarized the results regarding GSST phase transition in a schematic phase diagram which is shown in Fig. 4-14. Without quenching, bulk GSST material is always in its hexagonal ground state across the entire composition range. The cubic GSST phase appears upon liquid nitrogen quenching for $x \leq 0.8$, but its volume fraction does not change much with Se substitution. Thus, the phase transition from crystalline phase to amorphous phase in quenched GSST samples for $x \geq 0.8$ is probably unrelated to the presence of the cubic phase. Metal-to-insulator transitions were observed both in Se-doped slow cooled GSST as well as in quenched GSST at $x \geq 0.8$, even though the former is still crystalline and the amorphous phase is only achieved by quenching. So it is clear that the Se substitution brings on changes in GST material which needs to be understood by detailed local structure studies (which will discussed in Chapter 6). On warming amorphous GSST $x = 0.9$ from room temperature to 650K, partial crystallization is observed above ~580 K, which is much higher than the reported temperature for amorphous GST (~ 440 K)[98].

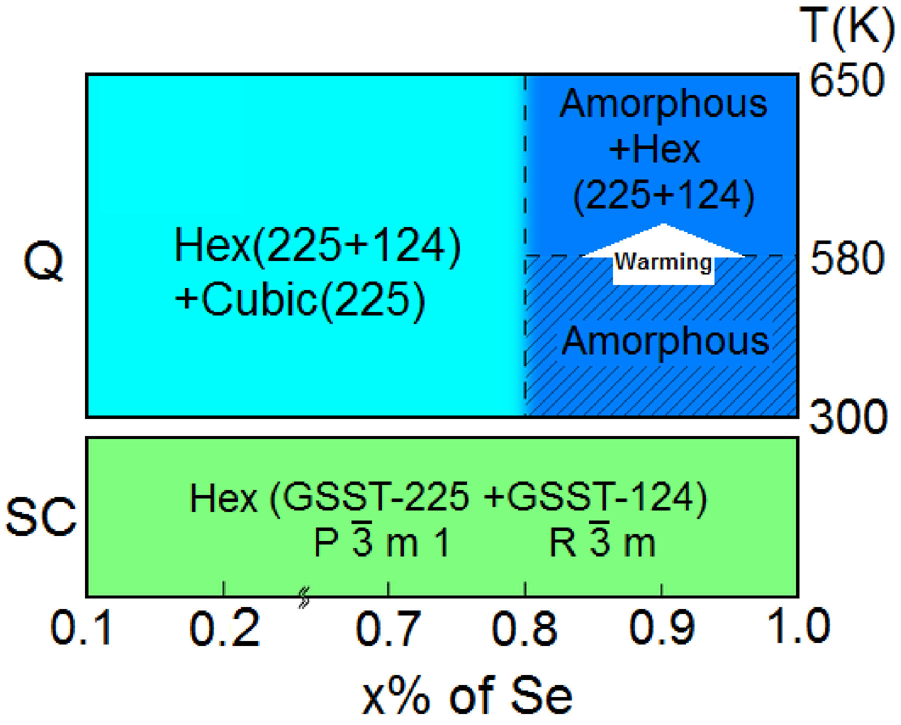

Figure 4-14: A schematic phase diagram summarizing the results on the GSST system. In the SC-GSST samples, no cubic phase and no transition to the amorphous phase is observed across the entire composition range. In the Q-GSST samples, the cubic phase appears as a second phase with about 20 % of the volume fraction. A phase change is observed at $x \geq 0.8$. On warming from the amorphous phase a $T_c \geq 580$K crystallization temperature is observed. Modified from [98].

4.3 DSC Measurements in Quenched GSST $x = 0.9$

The crystallization kinetics of amorphous GSST $x = 0.9$ were studied using Differential Scanning Calorimetry (DSC) measurements. In Fig. 4-15, the temperature-dependent DSC scan of quenched GSST $x = 0.9$ is shown. In this experiment, an increasing temperature procedure was applied on the amorphous GSST $x = 0.9$ sample, and heat flow was recorded as the y-axis data. When the amorphous sample undergoes an phase transition, heat flow will show an exothermic peak on DSC pattern which is pointing down as shown in the Fig. 4-15. From data, the crystallization began around 570K∼580K, and finished around 610K∼620K, with a peak temperature at about 595K. This result is in agreement with our temperature dependent XRD data where on warming the quenched GSST $x = 0.9$ sample, the amorphous-to-crystalline phase transition happens around 590K.

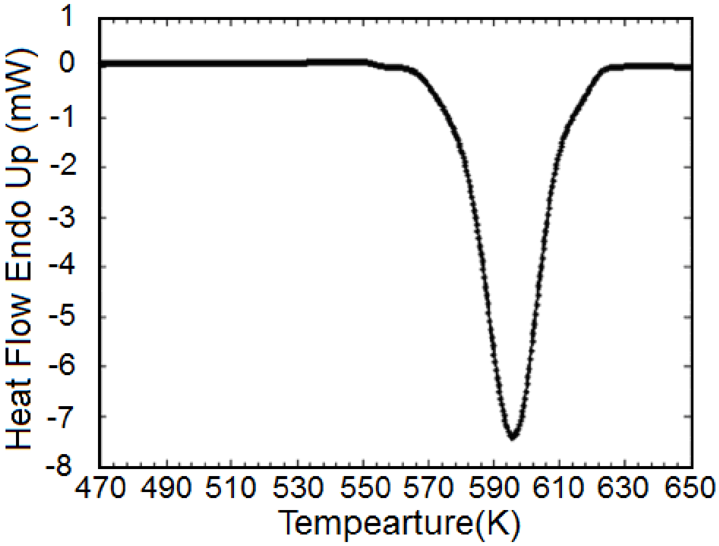

Figure 4-15: Differential Scanning Calorimetry (DSC) temperature-dependent scan on quenched GSST $x = 0.9$ from 470K to 650K.

Isothermal DSC scan results are shown in Fig. 4-16. The heat flow data as functions of heating time is plot in Fig. 4-16(a). Four sets of isothermal DSC scans are shown in different colors: 598K (magenta line), 593K (black line), 588K (green line) and 593K (blue line). These data demonstrate that as the temperature increases, the transition time decreases, which corresponds to a faster overall transition rate. From data in figure 4-16(a), the crystallization rate curves are computed and plotted in Fig. 4-16(b) with color correspondence. With the higher of the holding temperature, the crystallization process is also faster, which causes a decrease in transition time as we have discussed above. In Fig. 4-16(c), the transition time as a function of temperature is extracted from Fig. 4-16(b)'s data and fitted with exponential curve. This result also proves the conclusion that at higher holding temperature, the transition time is shorter. From these data, we also extracted the activation energy for crystallization. The results are shown in the inset of Fig. 4-16(d) which is a plot of $\ln(t_p - t)$ vs $1/T$. Here, t_p is the peak time, t is incubation time, and T is the holding temperature of the isothermal scan. According to Mehl [102] and Avrami's [103, 104] theory on crystallization, $\ln(t_p - t)$ versus $1/T$ obeys a linear relationship $(\ln(t_p - t) - E_a/RT{=}$constant. From which, E_a is the activation energy and R is the molar gas constant. Fig. 4-16(d) shows that the DSC isothermal data on quenched GSST $x = 0.9$ also obeys this relationship. The slope of the curve gives the value of activation energy of crystallization which is around 142.33 KJ/mol (or 1.47 eV)[98]. Another glass-forming system containing some of the same elements, $Ge_{30-x}Se_{70}Sb_x$, is reported to have activation energies of crystallization (from an amorphous phase) ranging from 119.2 KJ/mol - 204.81 KJ/mol for $15 \leq x \leq 25$ [105]; and our result 142.33 KJ/mol is within this range. The activation energy for crystallization estimated from isothermal DSC measurements implies that the amorphous GSST $x = 0.9$ material has good stability but it is not as high as in some good glass formers [101].

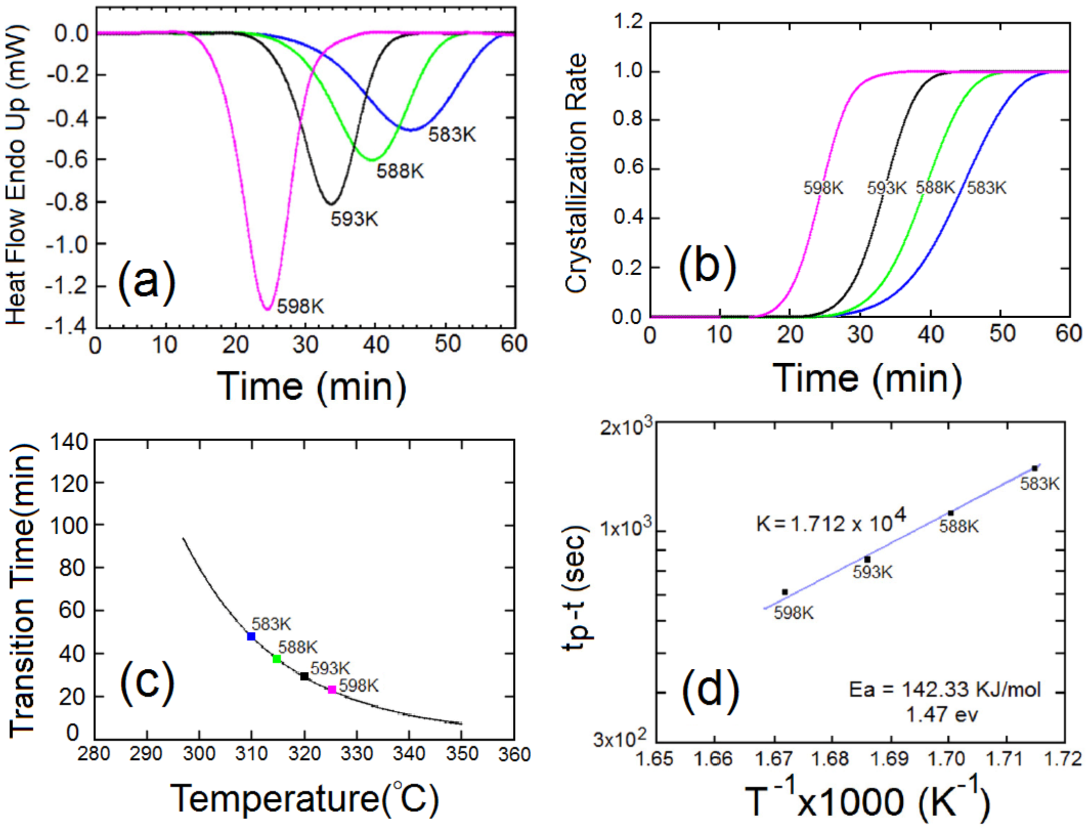

Figure 4-16: (a) Isothermal DSC scans of amorphous quenched GSST at $x = 0.9$ at different temperatures: 583K(blue), 588K(green), 593K(black), 598K(magenta). (b) Computed crystallization rate curves based on data in figure (a). (c) Computed transition time curves based on data in figure (a). (d) A $\ln(t_p - t)$ vs. $1/T$ plot, fitted with a line to extract the activation energy of the crystalline-to-amorphous phase transition for Q-GSST $x = 0.9$. An activation energy value is extracted from the fitting with $E_a = 142.33$ KJ/mol (or 1.47 eV).

Chapter 5

Local Structure of $Ge_2Sb_2Se_{5x}Te_{5-5x}$

Up to now, many works have been done on crystal structure of $Ge_2Sb_2Te_5$. In experiment, the three different phases of $Ge_2Sb_2Te_5$ have been vastly researched[10]. In computational calculation, many papers have been published centering on four different layering polymorphs[35]. However, few works have been focused on the local structure evolution across $Ge_2Sb_2Te_5$'s phase transition. In our case, when doped with Se, GSST-225 ($Ge_2Sb_2Se_{5x}Te_{5-5x}$) shows a crystalline-to-amorphous phase transition around $x = 0.8$ with liquid nitrogen quenching. This is different from the case of GST-225 since for GST-225 the fast thermal annealing is the trigger for amorphization, while for GSST-225 it's Se doping content. In order for further researching the local structure within GSST-225, we have performed neutron diffraction experiments systematically on this series compounds, the relative results and PDF analysis are presented in this chapter.

5.1 Neutron Diffraction of $Ge_2Sb_2Se_{5x}Te_{5-5x}$

Neutron diffraction experiments were carried to research Se doping-dependent phase transition in GSST-225 materials. Shown in Fig. 5-1 are the refinement results for neutron diffraction data of powder SC-GSST $x = 0.0$ and Q-GSST $x = 0.0$. Prior to neutron diffraction experiments, both EDS and XRD experiments were performed in order to confirm samples' chemical stoichiometries and rough phase compositions. After experiments, both neutron diffraction and XRD data confirmed the appearance of the following phases: in SC-GSST, a hexagonal $Ge_2Sb_2Se_{5x}Te_{5-5x}$ primary phase with $P\bar{3}m1$ symmetry (∼84% in volume fraction), a secondary trigonal $Ge_1Sb_2Se_{4x}Te_{4-4x}$ phase with $R\bar{3}m$ symmetry (∼16% in volume fraction). Compared with SC-GSST, Q-GSST has one more cubic $Ge_2Sb_2Se_{5x}Te_{5-5x}$ phase with $Fm\bar{3}m$ symmetry (∼15% in volume fraction) due to the effect of fast quenching. All samples show a small fraction (∼5% in volume fraction) of GeO_2 phase due to oxidation. All other samples with different doping contents show similar phase composition results but with slightly different volume fractions of each phase. These results are summarized in table 5.1.

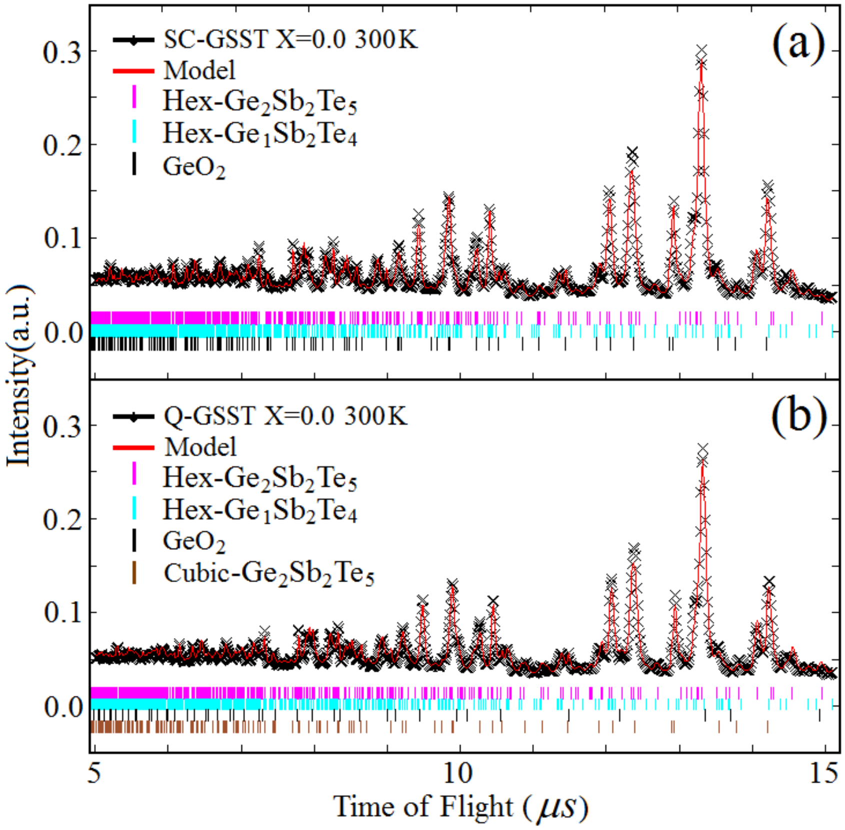

Figure 5-1: Neutron diffraction Rietveld refinements of (a) slow-cooled GSST $x = 0.0$ sample; (b) quenched GSST $x = 0.0$ sample. In figure, Black cross markers represent the raw data points. Red curves represent calculated patterns. The tick markers underneath data patterns represent the peak positions generated from different phases. Due to oxidation of the sample, a small amount of GeO_2 phase is detected.

SC-GSSTs			
Sample	GSST-225	GSST-124	GeO_2
$x = 0.0$	75.9(3)%	12.4(1)%	11.7(2)%
$x = 0.4$	82.3(2)%	13.4(4)%	4.3(5)%
$x = 0.6$	80.7(4)%	15.3(8)%	3.9(3)%

Q-GSSTs				
Sample	GSST-225	GSST-124	GSST-Cubic	GeO_2
$x = 0.0$	59.8(1)%	8.9(3)%	21.1(2)%	10.1(3)%
$x = 0.4$	66.6(7)%	10.3(1)%	18.9(2)%	4.1(4)%
$x = 0.6$	65.7(1)%	11.5(3)%	17.8(2)%	5.0(3)%
$x = 0.8$	66.2(4)%	10.8(1)%	23.0(1)%	0.0(0)%

Table 5.1: Volume fractions of different phases within SC-GSSTs and Q-GSSTs with different Se doping x extracted from PDF analysis.

5.2 PDF Analysis of $Ge_2Sb_2Se_{5x}Te_{5-5x}$

Fig. 5-2 shows the pair distribution function (PDF) data analysis for SC-GSST $x = 0.0$ sample. The raw PDF pattern is fitted with three majority phases: hexagonal $Ge_2Sb_2Te_5$ phase, trigonal $Ge_1Sb_2Te_4$ phase, an oxidation GeO2 phase. Here in the figure, the peak contribution from GeO_2 phase is subtracted in order to get a better visual. Most of sharp-peak features on PDF pattern are reproduced by these three phases discussed above. The simulated PDF pattern is shown in red curve. Under the main pattern, PDF partials coming from different atomic pairs are plotted in different colors.

A comparison of PDF patterns of SC-GSST $x = 0.0$ and Q-GSST $x = 0.0$ is shown in Fig. 5-3(a). They show similar patterns with small differences in some details. In general, the PDF pattern generated from SC-GSST sample is similar to that generated from Q-GSST sample with same Se doping content. This is because the cubic phase in Q-GSST is in nature a variation of the hexagonal phase with distortions[106]. A simple rotation can map the [111] crystalline direction of the cubic phase onto the c-axis of the hexagonal phase and similar stacking layering is shown between these two lattices. Taking consideration of their local structures, shown in Fig. 5-4(b) is a comparison of the PDFs generated by hexagonal phase (red curve) and cubic phase (blue curve), although different intensities are observed

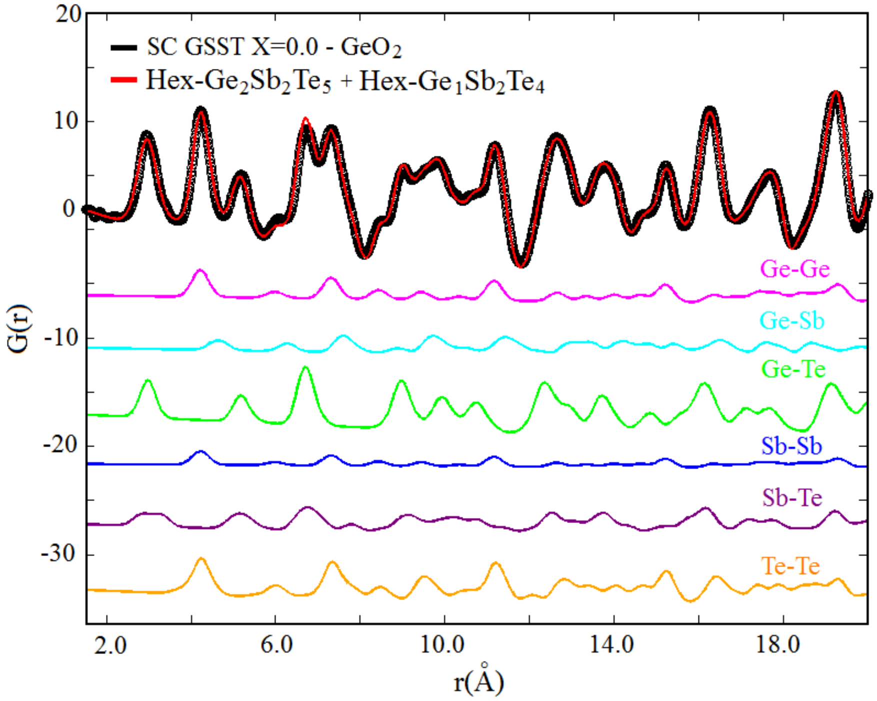

Figure 5-2: PDF pattern and its partial plots of slow cooled GSST $x = 0.0$. Black dots represents the raw PDF data. Contribution of GeO$_2$ phase is subtracted from raw data. The red line represents the calculated pattern. Underneath are the partial plots for Ge-Ge (colored in magenta), Ge-Sb (colored in cyan), Ge-Te (colored in green), Sb-Sb (colored in blue), Sb-Te (colored in purple), Te-Te (colored in orange) pair correlations.

due to different volume fractions of these two phases, similarities in peak positions and relative peak intensities can be seen from this figure. Fig. 5-3(b) and (c) show crystalline structures of hexagonal GST-225 phase and cubic GST-225 phase, some of the bond lengths and bond angles are labeled accordingly.

Fig. 5-4(a) shows a comparison of PDF patterns of SC-GSST $x = 0.6$ and Q-GSST $x = 0.6$. Both of the samples contain a small volume fraction ($\sim 5\%$) of GeO$_2$ phase due to oxidation. In order for a better comparison, the contribution of GeO$_2$ phase on PDF pattern is subtracted from raw data, the two patterns show similarities as expected. Fig. 5-4(c) shows PDF data across phase transition in Q-GSSTs. PDF data for Q-GSST $x = 0.0/0.4/0.6/0.8/0.85/0.9/1.0$ are shown in different colors. Within them, Q-GSST $x = 0.0/0.4/0.6/0.8$ samples are in crystalline phases, they show shape peak features due to long range ordering in structures. Q-GSST $x = 0.85/0.9/1.0$

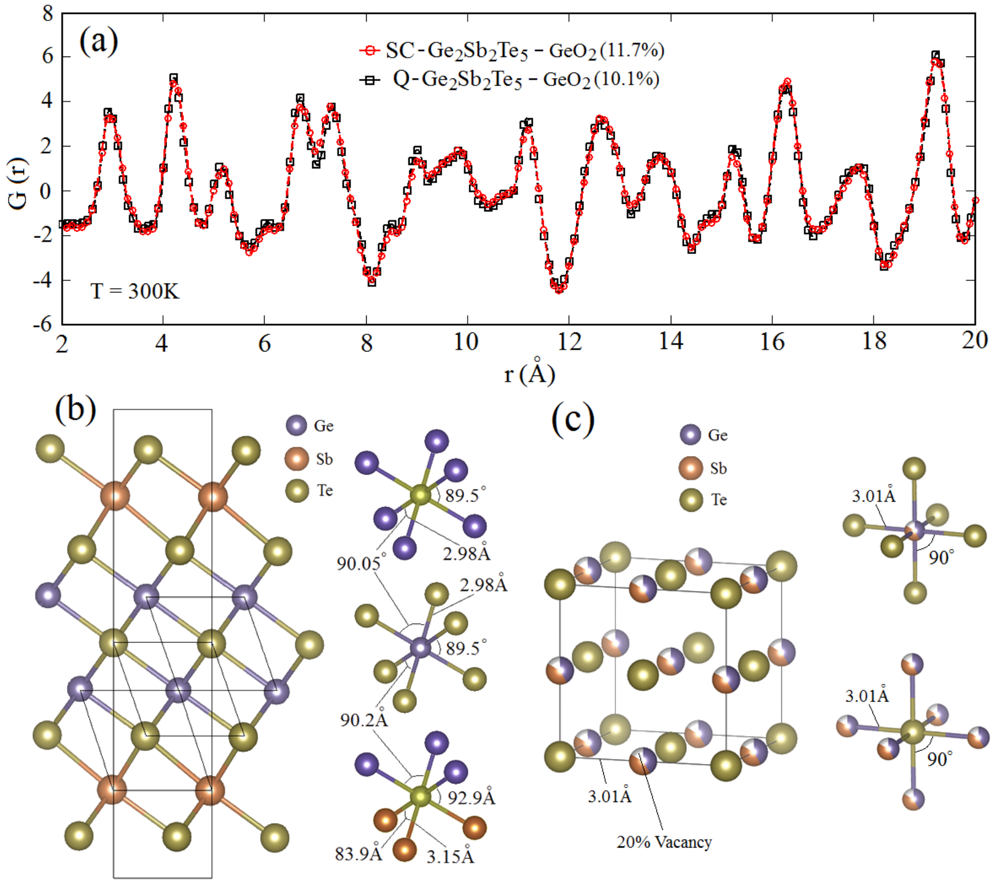

Figure 5-3: Panel (a) shows a comparison of PDF patterns of slow cooled $Ge_2Sb_2Te_5$ (colored in red and dotted with circle markers) and quenched $Ge_2Sb_2Te_5$ (colored in black and dotted with square markers) samples. Both data are collected at temperature of 300K. Contribution of the oxidized phase GeO_2 is subtracted from raw data. Panel (b) and (c) shows unit cell structures of hexagonal GST-225 and cubic GST-225 phases. Some bond lengths and angles are labeled accordingly.

samples are in amorphous phases, above r=5Å, shape peak features are replaced by small ripples in PDF, no useful structural information can be extracted from this segment of data. This corresponds to the fact that no long range order persists after amorphization in Q-GSST samples. Interestingly, Q-GSST $x = 0.85/0.9/1.0$ samples still show pair correlation peaks at low r range (see brown, orange, black curves in 5-4(c) below 3Å) which indicates the existence of local structures in these samples. The short r range correlation is featured by two peaks which located at around 2.37Å and 2.61Å on PDF patterns. At location around r=3.9Å, a triangle-shaped peak is observed with large intensity. It can be inferred from this peak shape that multiple shoulder peaks appear on both left and right sides to the main peak so as to merge into a non-Gaussian peak profile. From Fig. 5-4(c), it can be seen that this composite peak is a variation of the peaks located around 4Å on crystalline samples' PDF patterns. The reason for correlation length get shortened is because with the increasing of Se doping content, peaks shift to the left due to shrinking of unit cell dimensions. This peak-shift effect also appears on Fig. 5-5(a), although the peak shift is small due to the change of Se doping content is small between Q-GSST $x = 0.85$ and $x = 0.9$ samples.

Another unique feature of these first two peaks is that no peak shift due to Se doping is observed. The first two peaks located at 2.37Å and 2.61Å are fitted with Gaussian peak profiles and their peak locations and peak areas are extracted from fitting. The results are listed in table 5.2. We can see from the table that first two peaks are of highly constant peak positions (2.375Å and 2.611Å), Se doping has no effect on these atomic pair correlation lengths.

Q-GSST Sample	Peak #1 Position	Peak #2 Position	Peak #1 Area	Peak #2 Area
$x = 0.85$ 100K	2.372Å	2.612Å	1.314	1.015
$x = 0.85$ 300K	2.378Å	2.610Å	1.295	0.988
$x = 0.90$ 100K	2.373Å	2.610Å	1.622	0.865
$x = 0.90$ 300K	2.375Å	2.612Å	1.635	0.821

Table 5.2: The peak position and peak area results of the Peak #1 (located around 2.37Å) and Peak #2 (located around 2.61Å) on PDF patterns of Q-GSST $x = 0.85$ and $x = 0.9$. Four sets of data were collected at temperature of 100K and 300K. Gaussian peak profiles were used to fit the peaks in order to extract information.

The PDF pattern of GSST $x = 0.8$ is highly interesting since it's near the boundary of phase transition. Fig. 5-4(d) shows a Gaussian fitting of the PDF pattern of GSST $x = 0.8$ sample at low r range (up to 3.5Å). Five peaks are detected and their peak locations are labeled accordingly. The first peak (located at 2.38Å) comes from the amorphous phase as you can see this markers the prelude of the first peak (2.37Å) in amorphous phase. The second peak located around 2.62Å is a shoulder peak to the tallest third peak which located at 2.84Å. It can be inferred that the second peak comes from the amorphous phase since they have similar bond lengths

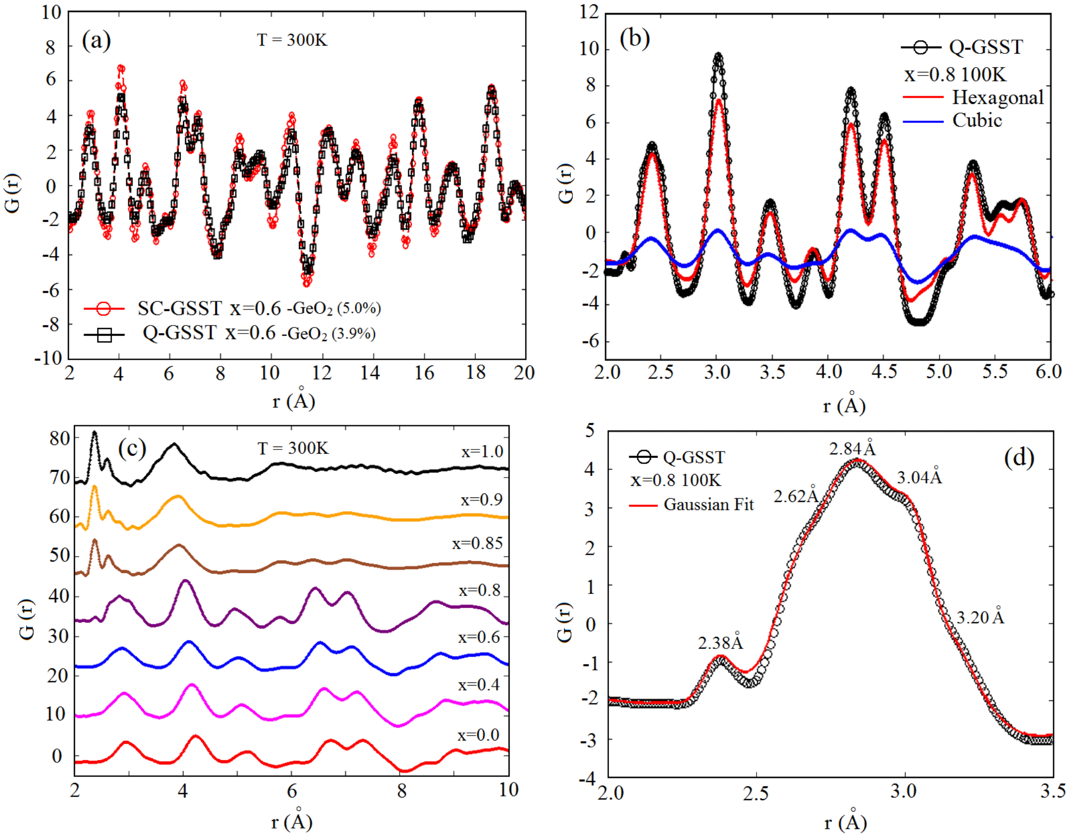

Figure 5-4: Panel (a) shows a comparison of PDF patterns of slow cooled GSST $x = 0.6$ (colored in red and dotted with circle markers) and quenched GSST $x = 0.6$ (colored in black and dotted with square markers) samples. Both data were collected at temperature of 300K. Contribution of the oxidized phase GeO_2 is subtracted from raw data. Panel (b) shows the PDF pattern for quenched GSST $x = 0.8$ (data collected at 100K). The contribution of hexagonal phase (red line) and cubic phase (blue line) are plotted for comparison. Panel (c) shows PDF patterns of quenched GSST $X = 0.0/0.4/0.6/0.8/0.85/0.9/1.0$ samples up to 10Å, all data were collected at 300K. Panel (d) shows a Gaussian fitting of the quenched GSST $x = 0.8$ data, five Gaussian peaks are labeled with their peak positions.

(2.61∼2.62Å). The tallest peak located on 2.84Å is from crystalline phases. There is a good continuity of peak shift from Q-GSST $x = 0.0$ to $x = 0.8$. There is a third small peak (located at 2.83Å) in amorphous GSST PDF pattern which corresponds to the Sb-Te atomic pair correlation length. The fourth and fifth peak are located at 3.04Å and 3.20Å respectively, they are not obvious on amorphous PDF pattern since their low peak intensities are easily submerged or destroyed by the termination ripples from Fourier transformation in PDF. They come from the Ge/Sb-Se/Te correlations in cubic structures. From PDF analysis, it can be concluded that the majority part of GSST $x = 0.8$ sample is in crystalline phases, only a small part is transferred into amorphous phase due to fast quenching. However, in Rietveld refinement, amorphous phase wouldn't possess any shape peak feature and will be treated as background, this explains why we didn't discover the trace of amorphous phase in GSST $x = 0.8$ Rietveld refinements.

Fig. 5-5(b) shows a PDF fit of the Q-GSST $x = 0.9$ sample at low r range (up to 3.5Å) with the four tetragonal models showed on Fig. 5-5(c). It is worth mentioning that in a real material, the four corners of a tetragon are not necessarily occupied by Se or Te atoms only, a hybridization of Se/Te atoms taking four corners could happen which means many more types of tetragonal models exiting in a real amorphous GSST material.

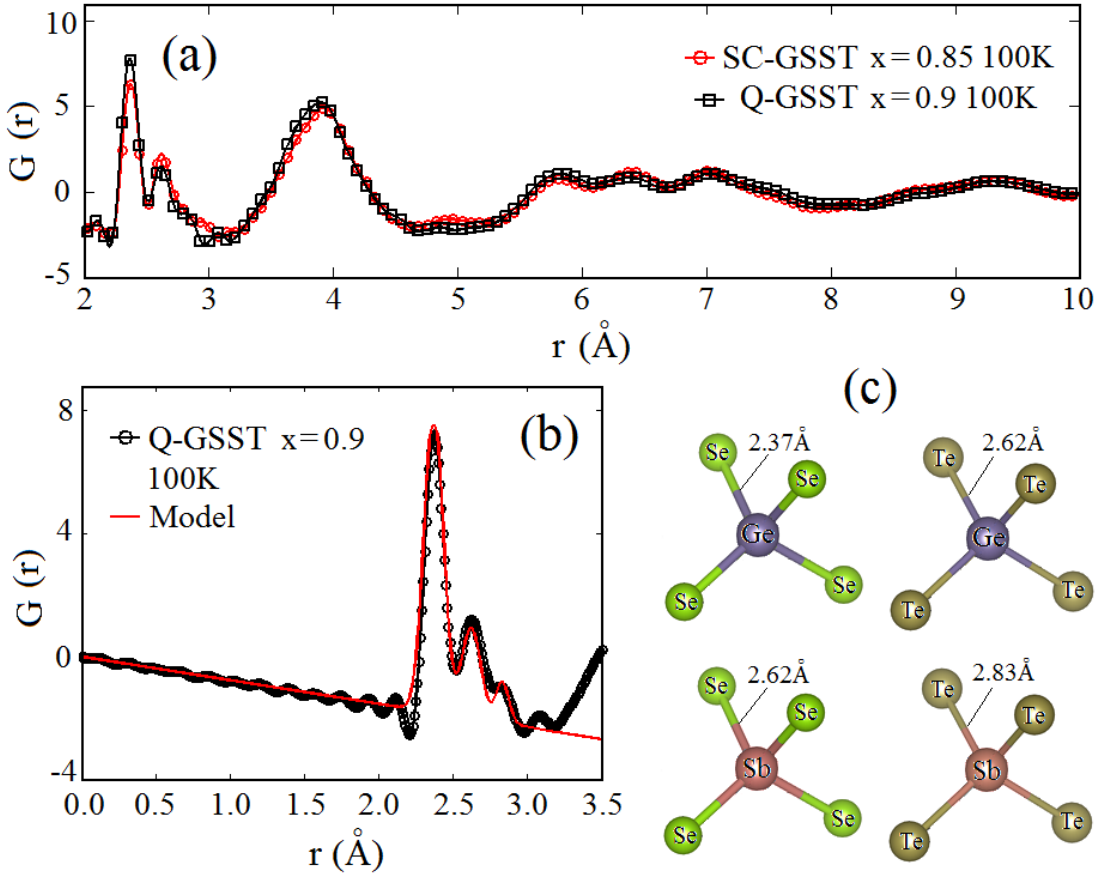

Figure 5-5: Panel (a) shows a comparison of PDF patterns of slow cooled GSST $x = 0.85$ (colored in red and dotted with circle markers) and quenched GSST $x = 0.85$ (colored in black and dotted with square markers) samples. Panel (b) shows a PDF fit of GSST $x = 0.9$ data collected at 100K with the models shown in Panel (c).

Chapter 6

Conclusions

Phase change materials are prominent medium for fabricating next-generation data storage devices. Their rapid phase transition between crystalline and amorphous phases enables the fast speed of reading and writing data into or out of the device. As a successful phase change material, $Ge_2Sb_2Te_5$ has been researched for many decades and a lot of electronic and optical memories have been commercialized based on this material[8]. In order to optimize the data storage device based on GST-225, Se-doped GSST-225 materials have been systematically synthesized and relative research have been done on this material.

Without quenching, bulk SC GSST-225 always show their crystalline phases. Rietvelt refinements on XRD patterns show two phases coexisting in these materials: a majority hexagonal GSST-225 phase and a secondary hexagonal GSST-124 phase. GSST-124 can be viewed as a superlattice structure of corresponding GSST-225. Their ratio in phase volume fraction is maintained around 6:1. Compared with SC-GSST, Q-GSST bulk material shows another cubic phase. This cubic phase is featured with a crystal structure which is similar to rock salt. Se/Te atoms are co-occupying the 4(a) sites while the 4(b) sites are occupied by 40% of Ge, 40% of Sb and 20% of vacancies. According to refinement results, the volume fraction of cubic phase does not change much with Se substitution (∼20% in volume fraction). Thus, the phase transition to the amorphous phase in Q-GSST samples with $x > 0.8$ is most likely non-relative to the presence of cubic phase. Amorphous phase in GSST material is only achieved through liquid nitrogen quench. A crystalline-to-amorphous phase transition is observed in Q-GSSTs around $x = 0.8$.

Resistivity measurements are systematically performed on GSST-225 samples. A metal-to-insulator transition is observed both in SC-GSSTs as well as in Q-GSSTs around $x = 0.8$, even though SC-GSSTs are still in crystalline phases. Several orders' change in magnitude of resistivty is observed between crystalline and amorphous phases of GSST material which shows its potential to become the next promising material to be used in PCM random access memories.

In order to study the crystallization kinetics of GSST material, amorphous GSST $x = 0.9$ sample is heated in a vacuum chamber within XRD machine from room temperature to 650K. Partial crystallization featuring Bragg peaks located around $2\theta = 30°$ is observed above temperature of 580K. This is much higher than that previously reported in amorphous GST material ($\sim$ 440 K). DSC measurements including temperature scans and isothermal scans were performed on amorphous GSST $x = 0.9$. Similar crystallization temperature is obtained which provides more evidence supporting our findings in temperature-dependent XRD experiments. The activation energy for crystallization is estimated from isothermal DSC measurements. Its value is around 1.47 eV which indicates that the amorphous GSST material has good stability but is not as high as that in some good glass formers.

In neutron diffraction studies, PDF analyses were performed in order to research the local structure evolution across phase transition in Q-GSSTs. The absence of sharp peak feature above 5Å on PDF patterns of amorphous Q-GSST samples shows the lost of long range ordering within these samples. However, two unusual atomic correlation peaks which of short bond lengths (2.37Å and 2.61Å) were observed in amorphous Q-GSST samples ($x = 0.85/0.9/1.0$). This indicates the existence of local structures which have short range ordering in amorphous phases. Through PDF analysis, tetragonal shaped local structure models with Ge/Sb atoms siting at centers and Te/Se atoms siting at corners were proposed.

Bibliography

[1] M. Wuttig and N. Yamada. Phase-change materials for rewriteable data storage. *Nature Materials*, 6(11):824–832, 2007.

[2] N. Yamada. Origin, secret, and application of the ideal phase-change material GeSbTe. *physica status solidi (b)*, 249(10):1837–1842, 2012.

[3] P. Guo, A. M. Sarangan, and I. Agha. A review of germanium-antimony-telluride phase change materials for non-volatile memories and optical modulators. *Applied Sciences*, 9(3):2076, 2019.

[4] Q. Hubert, C. Jahan, A. Toffoli, G. Navarro, S. Chandrashekar, P. Noe, D. Blachier, V. Sousa, L. Perniola, J.-F. Nodin, A. Persico, R. Kies, S. Maitrejean, A. Roule, E. Henaff, M. Tessaire, P. Zuliani, R. Annunziata, G. Pananakakis, G. Reimbold, and B. De Salvo. Lowering the reset current and power consumption of phase-change memories with carbon-doped $Ge_2Sb_2Te_5$. In *2012 4th IEEE International Memory Workshop*, pages 1–4, May 2012.

[5] H.-Y. Cheng, S. Raoux, and Y.-C. Chen. The impact of film thickness and melt-quenched phase on the phase transition characteristics of $Ge_2Sb_2Te_5$. *Journal of Applied Physics*, 107(10):074308, 2010.

[6] Y. Choi, M. Jung, and Y. K. Lee. Effect of heating rate on the activation energy for crystallization of amorphous $Ge_2Sb_2Te_5$ thin film. *Solid-State Lett.*, 12(1):17–19, 2009.

[7] Z. Gong, F. Yang, L. Wang, R. Chen, J. Wu, C. P. Grigoropoulos, and J. Yao. Phase change materials in photonic devices. *J. Appl. Phys.*, 129(3):030902, 2021.

[8] P. Noé, C. Vallée, F. Hippert, F. Fillot, and J. Raty. Phase-change materials for non-volatile memory devices: from technological challenges to materials science issues. *Semiconductor Science and Technology*, 33(1):013002, 2017.

[9] L. Lazzarini, E. Rotunno, V. Grillo, and M. Longo. Determination of the atomic stacking sequence of Ge-Sb-Te nanowires by HAADF STEM. *MRS Online Proceedings Library (OPL)*, 1512(4), 2013.

[10] T. Matsunaga and N. Yamada. Structural investigation of $GeSb_2Te_4$: A high-speed phase-change material. *Physical Review B*, 69(10):104111, 2004.

[11] T. Matsunaga, R. Kojima, N. Yamada, K. Kifune, Y. Kubota, S. Kohara, and M. Takata. Structural analysis of GeSbTeSe phase-change materials. *Libr E PCOS*, pages 99–104, 2009.

[12] S. Shin, H. K. Kim, J. Song, D. J. Choi, and H. H. Cho. Phase-dependent thermal conductivity of $Ge_1Sb_4Te_7$ and N:$Ge_1Sb_4Te_7$ for phase change memory applications. *Journal of Applied Physics*, 107:033518, 2010.

[13] T. Matsunaga, R. Kojima, N. Yamada, K. Kifune, Y. Kubota, and M. Takata. Structural investigation of $Ge_3Sb_2Te_6$, an intermetallic compound in the GeTe-Sb_2Te_3 homologous series. *Appl. Phys. Lett.*, 90:161919, 2007.

[14] J. Kumar., P. Kumar, M. Ahmad, R. Chander, R. Thangaraj, and T. S. Sathiaraj. Phase transformation in Pb:GeSbTe chalcogenide films. *Eur. Phys. J. Appl. Phys.*, 44(10):117–123, 2008.

[15] K. Jeong, S. Park, M. Park, D. Ahn, J. Han, W. Yang, H.-S. Jeong, and M.-H. Cho. Evolution of crystal structures in GeTe during phase transition. *Sci. Rep.*, 7(10):955, 2017.

[16] T. Chattopadhyay, J. X. Boucherle, and H. G. VonSchnering. Neutron diffraction study on the structural phase transition in GeTe. *J. Phys. C: Solid State Phys.*, 20(10):1431, 1987.

[17] R. Shekhawat, H. Pamuluri, V. E. Madhavan, and K. Ramesh. Structural transformation and phase change properties of Se substituted GeTe. *Sci. Rep.*, 11(1):7604, 2021.

[18] R. Tsu, W. Howard, and L. Esaki. Optical and electrical properties and band structure of GeTe and SnTe. *Physical Review*, 172(1):779–788, 1968.

[19] F. Herman, R. Kortum, I. B. L. Ortenburger, and J. P. Van Dyke. Relativistic band structure of GeTe, SnTe, PbTe, PbSe, and PbS. *J. Phys. Colloques*, 27(29):62–64, 1968.

[20] Y. Tung and M. Cohen. Relativistic band structure and electronic properties of SnTe, GeTe, and PbTe. *Physical Review*, 180(10):823–826, 1969.

[21] S. F. Alexander, S.-B. Jaime, C. Carolien, J. Hadermann, A. V. Fedorov, D. Y. Usachov, A. N. Chaika, B. C. Walls, K. Zhussupbekov, I. V. Shvets, M. Muntwiler, M. Amati, L. Gregoratti, A. Y. Varykhalov, O. Rader, and L. V. Yashina. Atomic and electronic structure of a multidomain GeTe crystal. *ACS Nano.*, 14(12):16576–16589, 2020.

[22] L. Zhao, H. Deng, I. Korzhovska, M. Begliarbekov, Z. Chen, E. Andrade, E. Rosenthal, A. Pasupathy, V. Oganesyan, and K.-E. Lia. Emergent surface superconductivity in the topological insulator Sb_2Te_3. *Nat. Commun.*, 6(1):8279, 2015.

[23] A. Lawalab, A. Shaaria, R. Ahmeda, and N. Jarkonia. Sb_2Te_3 crystal a potential absorber material for broadband photodetector: A first-principles study. *Results in Physics*, 7(1):2302–2310, 2017.

[24] M. Lewin, L. Mester, T. Saltzmann, S.-J. Chong, M. Kaminski, B. Hauer, M. Pohlmann, A. M. Mio, M. Wirtssohn, P. Jost, M. Wuttig, U. Simon, and T. Taubner. Sb_2Te_3 growth study reveals that formation of nanoscale charge carrier domains is an intrinsic feature relevant for electronic applications. *ACS Appl. Nano Mater.*, 1(1):6834–6842, 2018.

[25] C. Zheng, J. Tu, S. Jiao, M. Wang, and Z. Wang. Sb_2Te_3 hexagonal nanosheets as high-capacity positive materials for rechargeable aluminum batteries. *ACS Appl. Energy Mater.*, 3(11):12635–12643, 2020.

[26] Y. R. Guo, F. Dong, C. Qiao, J. J. Wang, M. Wang, S. Y. andXu, Y. X. Zheng, R. J. Zhang, L. Y. Chen, C. Z. Wang, and K. M. Ho. Structural signature and transition dynamics of Sb_2Te_3 melt upon fast cooling. *Phys. Chem.*, 1(20):11768, 2018.

[27] G.-S. Park, J.-H. Kwon, M. Kim, H. R. Yoon, W. Jo, T. K. Kim, J.-M. Zuo, and Y. Khang. Crystalline and amorphous structures of Ge–Sb–Te nanoparticles. *Journal of Applied Physics*, 102(1):013524, 2007.

[28] P. I. Lazarenko, A. A. Sherchenkov, S. A. Kozyukhin, A. V. Babich, S. P. Timoshenkov, D. G. Gromov, A. S. Shuliatyev, and E. N. Redichev. Electrical properties of the $Ge_2Sb_2Te_5$ thin films for phase change memory application. *AIP Conference Proceedings*, 1727(1):020013, 2016.

[29] I. Friedrich, V. Weidenhof, W. Njoroge, P. Franz, and M. Wuttig. Structural transformations of $Ge_2Sb_2Te_5$ films studied by electrical resistance measurements. *Journal of Applied Physics*, 87(9):4130–4134, 2000.

[30] M. Osiac. The electrical and structural properties of nitrogen $Ge_1Sb_2Te_4$ thin film. *Coatings*, 8(4):117, 2018.

[31] A. Lotnyk, I. Hilmi, U. Ross, and B. Rauschenbach. Van der waals interfacial bonding and intermixing in GeTe-Sb_2Te_3-based superlattices. *Nano Research*, 11(3):1676–1686, 2018.

[32] V. L. Deringer and R. Dronskowski. DFT studies of pristine hexagonal $Ge_1Sb_2Te_4$(0001), $Ge_2Sb_2Te_5$(0001), and $Ge_1Sb_4Te_7$(0001) surfaces. *The Journal of Physical Chemistry C*, 117(29):15075–15089, 2013.

[33] T. Tsafack, E. Piccinini, B.-S. Lee, E. Pop, and M. Rudan. Electronic, optical and thermal properties of the hexagonal and rocksalt-like $Ge_2Sb_2Te_5$ chalcogenide from first-principle calculations. *Journal of Applied Physics*, 110(6):063716, 2011.

[34] P. Urban, M. N. Schneider, L. Erra, S. Welzmiller, F. Fahrnbauera, and O. Oeckler. Temperature dependent resonant x-ray diffraction of single-crystalline $Ge_2Sb_2Te_5$. *Cryst. Eng. Comm.*, 15(24):4787–4982, 2013.

[35] S. V. Eremeev, I. P. Rusinov, P. M. Echenique, and E. V. Chulkov. Temperature-driven topological quantum phase transitions in a phase-change material $Ge_2Sb_2Te_5$. *Scientific Reports*, 6(1):38799, 2016.

[36] J. Tominaga, A. V. Kolobov, P. Fons, T. Nakano, and S. Murakami. Ferroelectric order control of the Dirac-Semimetal phase in GeTe-Sb_2Te_3 superlattices. *Advanced Materials Interfaces*, 1(1):1300027, 2014.

[37] J. Kalikka, X. Zhou, J. Behera, G. Nannicini, and R. E. Simpson. Evolutionary design of interfacial phase change van der Waals heterostructures. *Nanoscale*, 8(42):18212–18220, 2016.

[38] D. Campi, L. Paulatto, G. Fugallo, F. Mauri, and M. Bernasconi. First-principles calculation of lattice thermal conductivity in crystalline phase change materials: GeTe, Sb_2Te_3, and $Ge_2Sb_2Te_5$. *Physical Review B*, 95(2):024311, 2017.

[39] N.-K. Chen, X.-B. Li, X.-P. Wang, S.-Y. Xie, W. Q. Tian, S. Zhang, and H.-B. Sun. Metal–insulator transition of Ge–Sb–Te superlattice: An electron counting model study. *IEEE Transactions on Nanotechnology*, 17(1):140–146, 2018.

[40] X. Yu and J. Robertson. Modeling of switching mechanism in GeSbTe chalcogenide superlattices. *Scientific Reports*, 5(1):12612, 2015.

[41] J. Kim, J. Kim, Y. Song, R. Wu, S. Jhi, and N. Kioussis. Weyl node assisted conductivity switch in interfacial phase-change memory with van der waals interfaces. *Physical Review B*, 96(23):235304, 2017.

[42] J. Kellner, G. Bihlmayer, M. Liebmann, S. Otto, C. Pauly, J. E. Boschker, V. Bragaglia, S. Cecchi, R. N. Wang, V. L. Deringer, P. Küppers, P. Bhaskar, E. Golias, J. Sánchez-Barriga, R. Dronskowski, T. Fauster, O. Rader, R. Calarco, and M. Morgenstern. Mapping the band structure of GeSbTe phase change alloys around the fermi level. *Commun. Phys.*, 1(5):018, 2018.

[43] J. Kim, J. Kim, and S.-H. Jhi. Prediction of topological insulating behavior in crystalline ge-sb-te. *Phys. Rev. B*, 82(4):201312, 2010.

[44] I. V. Karpov and S. A. Kostylev. Set to reset programming in phase change memories. *IEEE Electron Device Letters*, 27(10):808–810, 2006.

[45] A. V. Kolobov, P. Fons, A. I. Frenkel, A. L. Ankudinov, J. Tominaga, and T. Uruga. Understanding the phase-change mechanism of rewritable optical media. *Nature Materials*, 3(10):703–708, 2004.

[46] A. V. Kolobov and J. Tominaga. Local structure of crystallized GeTe films. *Applied Physics Letters*, 82(382), 2003.

[47] A. Zeeshan. Growth, transport, and magnetic properties of oblique-angle-dsposited permalloy thin films. *Electronic Thesis or Dissertation*, pages 42–43, 2018.

[48] Quantum Design. PPMS MultiVu Application User's Manual, 2000.

[49] The MathWorks Inc. *Matlab version 7.10.0 (R2010a)*. Natick, Massachusetts, 2010.

[50] E. S. Watson and M. J. O'Neill. Apparatus for the determination of rates of heat absorption or evolution for materials, U.S. Patent: US2986028A, May. 1961.

[51] Netzsch. Differential scanning calorimetry (DSC) methods, 2015. ETZSCH-Gerätebau GmbH.

[52] N. Tanwar and V. K. Saraswat. A study of kinetics of phase transformation of $Ge_{10}Se_{75}Sb_{15}$ chalcogenide glass. *Journal of Non-Crystalline Solids*, 1(5):394–395, 2014.

[53] PerkinElmer. Pyris user manual, 2000. DSC User Manual.

[54] W. Friedrich, P. Knipping, and M. Laue. X-ray interference phenomena. *Verl. Der Kgl. Bayer. Akad. Der Wiss.*, 5:303–322, 1912.

[55] M. Attfield, P. Barnes, J. Cockcroft, and H. Driessen. Advanced certificate in powder diffraction on the web, 2006.

[56] H. A. Dabkowska and A. B. Dabkowski. *Crystal Growth of Oxides by Optical Floating Zone Technique*. Springer Handbook of Crystal Growth, 2010.

[57] W. L. Bragg. The structure of some crystals as indicated by their diffraction of x-rays. *Proc. Cambr. Phil. Soc.*, 17:43–47, 1913.

[58] B. E. Warren. *X-Ray Diffraction*. Dover Publications, 1990.

[59] A. C. Larson and R. B. V. Dreele. General structure analysis system manual, 2004.

[60] N. Ashcroft and N. Mermin. Solid state physics. *Appendix N*, 2010.

[61] J. Ziman. *Principles of the Theory of Solids*. Cambridge university press, 1979.

[62] G. Squires. *Introduction to the theory of thermal neutron scattering*. Cambridge university press, 2012.

[63] B. H. Toby. Expgui, a graphical user interface for GSAS. *J. Appl. Cryst.*, 34(210):1600–5767, 2001.

[64] B. H. Toby. R factors in rietveld analysis: how good is good enough? *Powder Diffraction*, 21(1):67–70, 2006.

[65] T. Egami and S. Billinge. *Underneath the Bragg peaks: structural analysis of complex materials.* Elsevier, 2003.

[66] S. J. L. Billinge. The rise of the x-ray atomic pair distribution function method: a series of fortunate events. *Phil. Trans. R. Soc.*, 377:2147, 2019.

[67] A. Wegner, D. Louca, and J. Yang. Local trigonal modes and the suppression of the charge density wave in $TiSe_{2\text{-}x}Te_2$. *Physical Review B*, 99(20):205110, 2019.

[68] A. Wegner, J. Zhao, J. Li, J. Yang, A. A. Anikin, G. Karapetrov, K. Esfarjani, D. Louca, and U. Chatterjee. Evidence for pseudo–jahn-teller distortions in the charge density wave phase of 1T-$TiSe_2$. *Physical Review B*, 101(19):195145, 2020.

[69] H. J. Kim, C. D. Malliakas, A. T. Tomic, S. H. Tessmer, M. G. Kanatzidis, and S. J. L. Billinge1. Local atomic structure and discommensurations in the charge density wave of $CeTe_3$. *Physical Review Letters*, 9(96):226401, 2006.

[70] V. Petkov, K. Chapagain, S. Shastri, and Y. Ren. Genesis of the periodic lattice distortions in the charge density wave state of 2H-$TaSe_2$. *Phys. Rev. B*, 101(12):121114, 2020.

[71] R. E. Dinnebier and Billinge S. J. L. *International tables of crystallography, vol. H.* International Union of Crystallography, 2014.

[72] K. Page. Atomic pair distribution function (pdf) analysis, 2018.

[73] X. Wang, S. Tan, X. Q. Yang, and E. Hu. Pair distribution function analysis: Fundamentals and application to battery materials. *Chin. Phys. B*, 29:028802, 2020.

[74] A.N. Fitch. *Synchrotron Methods.* Elsevier, 2019.

[75] P. F. Peterson, M. Gutmann, Th. Proffen, and S. J. L. Billinge. Pdfgetn: A user-friendly program to extract the total scattering structure function and the pair distribution function from neutron powder diffraction data. *J. Appl. Crystallogr.*, 33:1192, 2000.

[76] G. Placzek. The scattering of neutrons by systems of heavy nuclei. *Phys. Rev.*, 86:377, 1952.

[77] A. Anushika and D. Louca. The role of nanoscale atomic fluctuations in the superconducting mechanism of the BiS_2 superconductors. *University of Virginia, Physics*, 2017.

[78] J. Zheng, S. Ostrach, and Y. Kamotani. *Transport Phenomena in Heat and Mass Transfer*. Science Direct, 1992.

[79] G. Müller and J. Friedrich. *Crystal Growth, Bulk: Methods*. Encyclopedia of Condensed Matter Physics, 2005.

[80] P. Schmidt, M. Binnewies, R. Glaum, and M. Schmidt. *Chemical vapor transport reactions–methods, materials, modeling.* Advanced Topics on Crystal Growth, 2013.

[81] D. Hu, G. Xu, L. Xing, X. Yan, J. Wang, J. Zheng, Z. Lu, P. Wang, X. Pan, and L. Jiao. Two-dimensional semiconductors grown by chemical vapor transport. *Angewandte Chemie*, 56:3611–3615, 2017.

[82] R. Heinemann and P. Schmidt. Crystal growth by chemical vapor transport: Process screening by complementary modeling and experiment. *Cryst. Growth Des.*, 20:5986–6000, 2020.

[83] K. Klosse and P. Ullersma. Convection in a chemical vapor transport process. *Journal of Crystal Growth*, 18:167–174, 1973.

[84] M. Binnewies, R. Glaum, M. Schmidt, and P. Schmidt. Chemical vapor transport reactions–a historical review. *Z. Anorg. Allg. Chem.*, 20:219–229, 2013.

[85] P. Prabukanthan and R. Dhanasekaran. Growth of $CuGaS_2$ single crystals by chemical vapor transport and characterization. *Crystal Growth & Design*, 7:618–623, 2007.

[86] R. Grimes and N. Kuganathan. Database of ionic radii, 2015. Accessed: 2015-01-11.

[87] R.D. Shannon. Revised effective ionic radii and systematic studies of interatomic distances in halides and chalcogenides. *Acta Cryst.*, 1(32):751–767, 1976.

[88] J. Barták, P. Koštál, V. Podzemná, J. Shánělová, and J. Málek. Crystal growth kinetics and viscous behavior in $Ge_2Sb_2Se_5$ undercooled melt. *J. Phys. Chem. B*, 120(32):7998–8006, 2016.

[89] Y. Zhang, J. B. Chou, J. Li, H. Li, Q. Du, A. Yadav, S. Zhou, M. Y. Shalaginov, Z. Fang, H. Zhong, C. Roberts, P. Robinson, B. Bohlin, C. Ríos, H. Lin, M. Kang, T. Gu, J. Warner, V. Liberman, K. Richardson, and J. Hu. Broadband transparent optical phase change materials for high-performance nonvolatile photonics. *Nature Communications*, 10(4279):12196, 2019.

[90] J. Kim and S. Jhi. Disorder-induced structural transitions in topological insulating Ge-Sb-Te compounds. *Journal of Applied Physics*, 117(19):195701, 2015.

[91] V. Bragaglia, F. Arciprete, W. Zhang, A. M. Mio, E. Zallo, K. Perumal, A. Giussani, S. Cecchi, J. E. Boschker, H. Riechert, S. Privitera, E. Rimini, R. Mazzarello, and R. Calarco. Metal-insulator transition driven by vacancy ordering in gesbte phase change materials. *Science Report*, 6:23843, 2016.

[92] P. Jost, H. Volker, A. Poitz, C. Poltorak, P. Zalden, T. Schäfer, F. R. L. Lange, R. M. Schmidt, B. Holländer, M. R. Wirtssohn, and M. Wuttig. Disorder-induced localization in crystalline pseudo-binary GeTe-Sb_2Te_3 alloys between $Ge_3Sb_2Te_6$ and GeTe. *Advanced Functional Materials*, 25(40):6399–6406, 2015.

[93] H. Qian, H. Tong, M. He, H. Ji, L. Zhou, M. Xu, and X. Miao. Observation of carrier localization in cubic crystalline $Ge_2Sb_2Te_5$ by field effect measurement. *Scientific Reports*, 8(1):1–7, 2018.

[94] J.-J. Wang, Y.-Z. Xu, R. Mazzarello, M. Wuttig, and W. Zhang. A review on disorder-driven metal–insulator transition in crystalline vacancy-rich GeSbTe phase-change materials. *Materials (Basel, Switzerland)*, 10(8):862, 2017.

[95] D. Di Sante, S. Fratini, V. Dobrosavljević, and S. Ciuchi. Disorder-Driven Metal-Insulator transitions in deformable lattices. *Physical Review Letters*, 118(3):036602, 2017.

[96] T. Siegrist, P. Jost, H. Volker, M. Woda, P. Merkelbach, C. Schlockermann, and M. Wuttig. Disorder-induced localization in crystalline phase-change materials. *Nature Materials*, 10(3):202–208, 2011.

[97] W. Zhang, A. Thiess, P. Zalden, R. Zeller, P. H. Dederichs, J.-Y. Raty, M. Wuttig, S. Blügel, and R. Mazzarello. Role of vacancies in metal-insulator transitions of crystalline phase-change materials. *Nature Materials*, 11(11):952–956, 2012.

[98] Z. Xu, K. Park, J. A. Schneeloch, and D. Louca. Metal-insulator transition and doping-induced phase change in $Ge_2Sb_2Se_{5x}Te_{5-5x}$. *Applied Physics Letters*, 117(19):193503, 2020.

[99] N. Yamada and T. Matsunaga. Structure of laser-crystallized $Ge_2Sb_{2+x}Te_5$ sputtered thin films for use in optical memory. *Journal of Applied Physics*, 88(12):0021–8979, 2000.

[100] K. Ahn, D. Louca, S. J. Poon, and G. J. Shiflet. Topological and chemical ordering induced by Ni-Nd-Al-Ni-Nd metallic glass. *Physical Review B*, 70(22):224103, 2004.

[101] Y. He, G. M. Dougherty, G. J. Shiflet, and S. J. Poon. Unique metallic glass formability and ultra-high tensile strength in Al-Ni-Fe-Gd alloys. *Acta Metallurgica et Materialia*, 41(2):337–343, 1993.

[102] M. Castro, F. Domínguez-Adame, A. Sánchez, and T. Rodriguez. Model for crystallization kinetics: Deviations from Kolmogorov–Johnson–Mehl–Avrami kinetics. *Applied Physics Letters*, 75(15):2205–2207, 1999.

[103] M. Avrami. Kinetics of phase change. I general theory. *The Journal of Chemical Physics*, 7(12):1103–1112, 1939.

[104] M. Avrami. Kinetics of phase change. II Transformation-Time relations for random distribution of nuclei. *The Journal of Chemical Physics*, 8(2):212–224, 1940.

[105] A. Kaswan, V. Kumari, D. Patidar, N. S. Saxena, and K. Sharma. Kinetics of crystallization of $Ge_{30-x}Se_{70}Sb_x$ (x=15,20,25) chalcogenide glasses. *Processing and Application of Ceramics*, 8(1):25–30, 2014.

[106] X. Q. Liu, X. B. Li, L. Zhang, Y. Q. Cheng, Z. G. Yan, M. Xu, X. D. Han, S. B. Zhang, Z. Zhang, and E. Ma. New structural picture of the $Ge_2Sb_2Te_5$ phase-change alloy. *Physical Review Letters*, 106(2):025501, 2011.